Multiferroic properties of some perovskite oxides

A thesis submitted in partial fulfilment
for the degree of

Master of Science

as a part of the

Integrated Ph. D. programme
(Materials Science)

by

Chandan De

Chemistry and Physics of Materials Unit
Jawaharlal Nehru Centre for Advanced Scientific Research
(*A Deemed University*)
Bangalore, India.

March 2013

Dedicated to my grandparent

II

DECLARATION

I hereby declare that the matter embodied in this M.S. thesis entitled "**Multiferroic properties of some perovskite oxides**" is the result of investigations carried out by me under the supervision of Prof. A. Sundaresan at the Chemistry and Physics of Materials Unit, Jawaharlal Nehru Centre for Advanced Scientific Research, Bangalore, India and that it has not been submitted elsewhere for the award of any degree or diploma.

In keeping with the general practice in reporting scientific observations, due acknowledgement has been made whenever the work described is based on the findings of other investigators.

31/03/2013

_____
Chandan De

CERTIFICATE

I hereby certify that the matter embodied in this M.S. thesis entitled "**Multiferroic properties of some perovskite oxides**" has been carried out by Mr. Chandan De at the Chemistry and Physics of Materials Unit, Jawaharlal Nehru Centre for Advanced Scientific Research, Bangalore, India under my supervision and it has not been submitted elsewhere for the award of any degree or diploma.

_____

31/03/2013

Prof. A. Sundaresan

(Research Supervisor)

V

Acknowledgements

I am extremely thankful to *Prof. A. Sundaresan* and I take this opportunity to express my immense gratitude to him. He not only introduced me to the field of Material Science research but also has helped me with his invaluable guidance and fascinating constant encouragement. I sincerely thank him for providing interesting research problems and freedom to perform all my experiments. It has been a great pleasure for me to work under his guidance. I thank him for treating me as a family member and supporting me during my thesis work.

Prof. C. N. R. Rao, FRS has been a great source of inspiration during my MS work. I would like to sincerely thank him for providing us all the experimental facilities.

I thank *Dr. Rajeev Ranjan* and *Ms. Latitha* for providing us their experimental facility of piezoelectric measurement and giving me fruitful suggestions for my research work.

I thank *Prof. Kee Hoon Kim* and *Mr. Tai Hoon Kim* for fruitful collaboration and giving me suggestions for my research problem and providing us their experimental facilities.

My special thank to *Prof. Mamoru Fukunaga* for spending his valuable time and giving me his kind suggestions for my research problem.

Preface

This thesis is focused on the study of multiferroic properties of some perovskite oxides. Magnetoelectric multiferroics have been the subject of recent research because of their potential applications and interesting chemistry and physics. In this thesis we have investigated several oxides belong to perovskite family. The results of overall work have been presented in three chapters and two other chapters presenting an introduction to multiferroics and experimental techniques.

Chapter 1 introduces multiferroics, its brief history, and the magnetoelectric effect. It contains some basic physics about the both primary order parameters i,e electric and magnetic. It also gives various mechanisms that induce ferroelectricity in single phase material where magnetism is already present. Among various mechanisms of inducing ferroelectricity, the magnetism induced ferroelectricity provides a strong coupling between the electric and magnetic ordering which has been discussed in more detail.

Chapter 2 explains the basic principles of synthesizing and characterizing the materials, investigation in this work. This chapter has a major focus on a number of experimental techniques which were setup and used in the course of our work. A detailed procedure and difficulty of some important measurement have been discussed.

Chapter 3 is study of some perovskite materials ($NaRMnWO_6$: R= La, Nd and Tb) with unusual cation ordering for possible ferroelectric polarization. Though these materials are reported to be non centrosymmetric polar, our electrical measurements show no evidence for ferroelectric polarization.

Chapter 4   deals with disordered rare-earth perovskite manganites, which are very important for magnetically induced polarization. It presents a complete study of magnetism and ferroelectricity of $SmM_{0.5}M'_{0.5}O_3$: M, M'= Cr, Fe and Mn.

Chapter5   presents multiferroic properties of $R_{1-x}Sc_xMnO_3$: R= Nd, Sm and x = 0.1, 0.15, 0.2, 0.25, 0.3 materials, which shows ferroelectricity at the magnetic ordering temperature for all the substituted compounds while the parent compounds remains non ferroelectric.

Contents

Chapter 1

Introduction to multiferroics

Ever increasing requirement for better modern instruments and devices has led scientist to invent efficient and versatile functional data storing devices beyond the conventional magnetically information storing technology. Currently older technologies of storing the data magnetically, are approaching the perceived superparamagnetic limit and does not allow a further reduction of bit size, which subsequently limit the increase of areal density of the storage devices like hard drives. These magnetic materials, being the key of storage devices over the past few decades are already optimized. The tremendous success of hard discs now are based on improvements of the read-write head [2]. The mechanical moving parts (read-write head) of such devices are prone to failure and limit the access time which had led to the development of magnetic random access memory (MRAMs)[1, 35]. These can be viewed as an array of magnetic cells, each provided with a read-and-write unit or a bit (similar to the semiconducting storage device). The major technical difficulties of MRAMs are the need for high power to create the field for writing. However, the major advantage is that the magnetically reading of a bit is a nondestructive and fast process. On the otherhand Ferroelectric RAMs (FeRAMs) [36, 37] are very power efficient but have complementary issues as well, such as data retention and a destructive reading process. Trying to unite these two processes, we would need such materials which can be written electrically and read magnetically. These requirements can be met by *Magnetoelectric* materials where magnetic properties of the materials are influenced by

electric fields, or vice versa [7]. Further, the extra degree of freedom due to simultaneous ordering can make a huge data storage density.

The magnetoelectric effect has primarily been observed in those materials which possess both ferroelectric and magnetic ordering, and hence are called *Multiferroic* materials [7, 10]. Given the fact that these two properties had been thought to be mutually exclusive so far, in a material, synthesizing such materials have been of major scientific interest. Unfortunately, at present there is no such material know to exhibit both (anti)ferromagnetic and ferroelectric ordering as well as efficient coupling between them at room temperature. The breakthrough material for these requirements were found in classical multiferroic $TbMnO_3$ where spiral spin magentic ordering induces polarization and hence a storng coupling between them [10]. But, the lower magnetic ordering temperature does not allow to make an useful device on it. By definition, multiferroic includes spontaneous deformation or strain also but we have focussed only on the electrical and magnetic ordering. This chapter presents an introduction with a brief survey on multiferroics. In the later chapters we have discussed synthesis and characterization of some multiferrioc materials which are based on the spiral spin ordering as well as from some other aspects, such as symmetry consideration which are expected to enrich the emerging field of muliferroics.

1.1   Electric and magnetic ordering in solids

The electric charges of electrons and ions are responsible for the charge effects which gives electrical properties, whereas electron spins govern magnetic properties. Multiferroics are materials in which the properties of both the ordering, electrical (ferroelectricity) and magnetic (ferromagnetism/antiferromagnetism), coexist. Ideally, the magnetization of a ferromagnet in a magnetic field displays the usual hysteresis

and ferroelectrics exhibit a similar response to an electric field. Magnetoelectric multiferroics are simultaneously ferromagnetic and ferroelectric and cross-coupling responses are observed as there is a magnetic response to an electric field or vice versa. Ferroics is the generic name given to the study of ferromagnets, ferroelectrics, and ferroelastics. Multiferroics have been formally defined as materials that exhibit more than one primary ferroic order parameter simultaneously in a single phase. The microscopic origin of magnetism is basically the same in all magnetic systems. It is the presence of localized electrons, mostly in the partially filled d or f shells of transition-metal or rare-earth ions which have a corresponding localized spin or magnetic moment. Exchange interactions between the localized moments lead to magnetic ordering. The situation with ferroelectrics is quite different (discussed in the following section). There are several different microscopic sources of origin of ferroelectricity.

1.2   Historical perspective

In the year 1865 James Clerk Maxwell first combined the electricity and magnetism as single phenomenon called electromagnetism which would be governed by his given four equation (called Maxwell′s equation) which were later on reduced to two equations considering relativistic correction although earlier, these were thought to be independent phenomena. Later in 1894 Pierre Curie conjectured "*Materials should exist, which can be polarized by a magnetic field and magnetized by an electric field*" [15]. In 1959 magnetoelectric effect was predict by Landau and Lifshitz based on symmetry consideration in crystal "*The linear piezomagnetic effect and the linear magnetoelectric effect could exist in principle for certain magneto-crystalline classes.*" But he also commented in his a volume of the Course of Theoretical Physics that "*We*

will not however discuss these phenomena in more detail because it seems that till

present, presumably, they have not been observed in any substance" [16].

The situation changed soon after when Dzyaloshinsky predicted the linear ME effect in Cr_2O_3 which was experimentally observed in 1960 by Astrov and in 1966 by Asher [17, 18, 20]. After that a lot of materials were found to have linear magnetoelectric effect. The story was assumed new direction when it was realized that strong magnetic and electric cross-coupling coexist in solids (i.e., the appearance of magnetization **M** in an electric field **E**, or vice versa). Not only this, it was also realized that types of ordering (anti)ferromagnetism (the spontaneous ordering of orbital and spin magnetic moments) and ferroelectricity (the spontaneous ordering of electric dipole moments) can coexist in one material in the absence of external electric and magnetic fields. Later the term Multiferroic was first used by H. Schmid in 1994 which included spontaneous deformation i.e ferroelasticity [19]. Thus, the real multiferroic family has begun emerging [38, 39]. Now a days, the multiferroics predominantly applies to the coexistence of magnetism and ferroelectricity. People have interest in this field not only for a scientific knowledge but also for a technological advancing as these materials are potential for giving a very high speed, versatile functions and large storage capacity.

1.3   Physics ferroelectric and magnetic ordering

1.3.1   Ferroelectricity

The ferroelectric effect was first observed by Valasek in 1921, in the Rochelle salt [14]. This has molecular formula $KNaC_4H_4O_6 \cdot 4H_2O$. The formal definition of a ferroelectric requires that the material must possess a spontaneous dipole moment that can be

switched in an applied electric field, i.e. spontaneous switchable polarisation. This is found when two particles of charge q are separated by some distance r.

Figure 1.1   Electric Dipole for a charge q and distance r

The dipole moment, μ is

$$\mu = q.r$$

In ferroelectric materials, there is a net permanent dipole moment, which comes from the vector sum of dipole moments in each unit cell. This requires that it cannot exist in a structure that has a centre of symmetry, as any dipole moment generated in one direction would be forced by symmetry to be zero. Therefore, ferroelectrics must be non-centrosymmetric. However, this is not the only requirement. There must also be a spontaneous local dipole moment (which typically leads to a macroscopic polarization, but not necessarily, if there are domains that cancel completely). This means that the central atom must be in a non-equilibrium position. This primary axiom can be illustrated by considering an atom in an octahedral interstice. In Fig. 1.2.a the structure is said to be non-polar. There is no displacement of the central atom, and no net dipole moment. In Fig. 1.2.b, c however, the central atom is displaced to up, down and the structure is polar. There is now an inherent dipole moment in the structure. By applying electric field along P direction the polarization direction can be altered. This results in a dipole formation and net polarization (P). Polarisation may be defined as the total dipole moment (μ) per unit volume, i.e.

$$P = \frac{\Sigma \mu}{V}$$
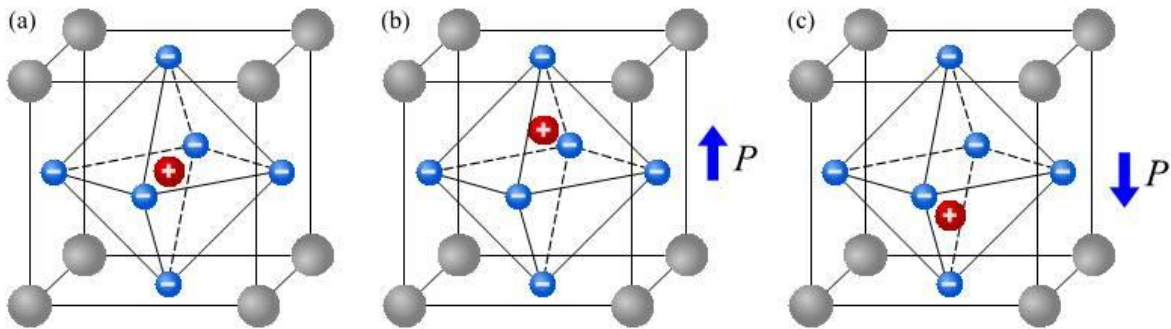
Figure 1.2   Illustration of a ferroelectric phase transition in an example of a perovskite structure. (a) Above the phase transition temperature T_C, the cation (marked red) is centered. There is no net polarization because the centers of the positive and the negative charge distributions coincide. Below T_C (b), (c), the ion off-centers, giving rise to a finite polarization P, which is the order parameter.

Materials are polarised along a unique crystallographic direction, in that certain atoms are displaced along this axis, leading to a dipole moment along it. Depending on the crystal system, there may be few or many possible axes. Upon examining a typical case study of $BaTiO_3$, (a classical ferroelectric), the tetragonal phase that forms when cooled from the high temperature cubic phase, through the Curie temperature, ($T_c = 120$ °C), the dipole moment can lie in six possible directions corresponding to the original cubic axes.
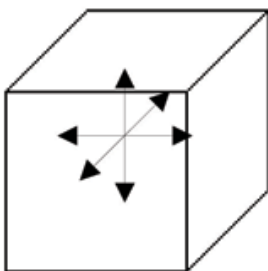
Figure 1.3   Six posible direction of polarization in $BaTiO_3$.

1.3.2 Ferroelectric Domain creation

A domain is a homogenous region of a ferroelectric, in which all of the dipole moments in adjacent unit cells have the same orientation. In a newly-grown single crystal, there will be many domains, having individual polarisations, organized in such a way that there will be no overall polarisation. This leads to a reduction electrostatic energy. Domain boundaries are arranged so that the dipole moments of individual domains meet at either 90° or 180°.

Individual domains
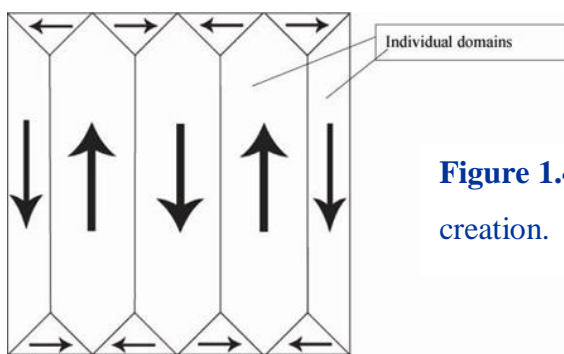
Figure 1.4   Ferroelectric   Domain creation.

In a polycrystal (one with more than one crystallographic grain), the arrangement of domains depends on grain size. If the grains are fine (<< 1 micron), then there is usually found to be one domain per grain. In larger grains there can be more than one domain in each grain. In an electric field (E), a polarised material lowers its energy by –$P.E$, (where P is the polarisation). Any dipole moments which lie parallel to the electric field are lowered in energy, while moments that lie perpendicular to the field are higher in energy and moments that lie anti-parallel are even higher in energy, (+$P.E$). This introduces a driving force to minimise the free energy, such that all dipole moments align with the electric field.

P

The dipole moment is stable either aligned to the left or the right. This is because the horizontal direction is crystallographically unique.

P
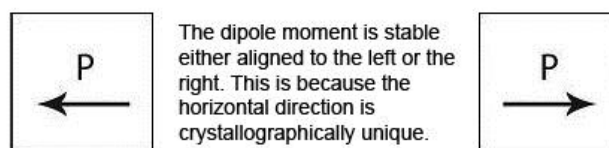
These two moments are stable, because they sit in potential energy wells. The potential barrier between them can be represented on a free energy diagram.

(a) If the material is considered to be homogenous,
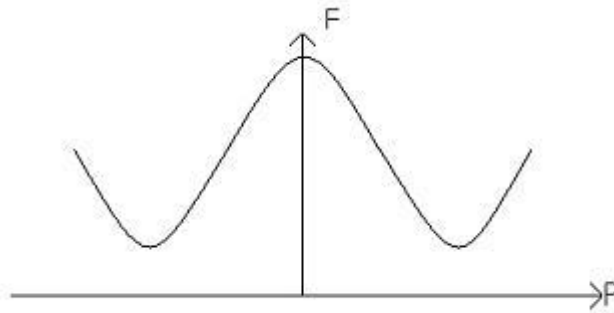
(b) If the polarisation points left,
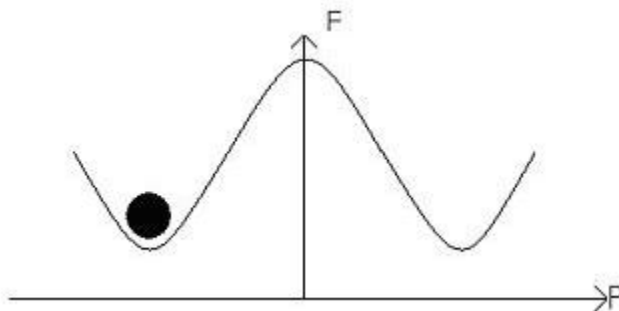
(c) If the electric field alters the energy profile, resulting in a 'tilting' of the potential well,
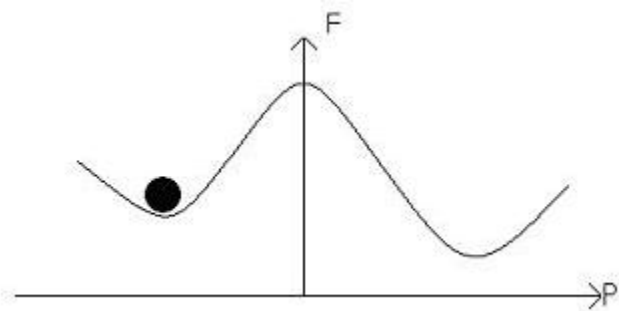
(d) An increase in the electric field will result in a greater tilt, and lead to the dipole moments switching:
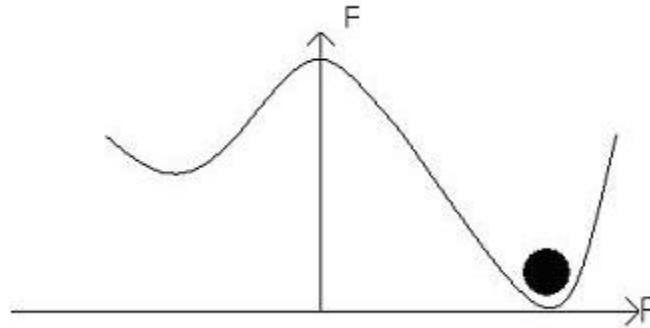
Next we must look at the more realistic scenario in which domains form. Consider a material which is fully polarised, so that all of the dipole moments are aligned in the same direction. Then apply a reversed electric field over it. New domains with a reversed polarisation nucleate inhomogenously. This requires a certain amount of time, in the same manner as any nucleation process. When the fluctuating nuclei reach a certain critical radius, they grow outwards, forming needle-like structures. When they reach the other side of the ferroelectric, they begin to grow outwards.

This shows the origin of the hysteresis loop. The removal of the field will leave some polarisation behind, and only when the field is reversed does the polarisation start to lessen as new, oppositely poled domains form. They grow quickly and giving a large change of polarisation for very little electric field. But to form an entirely reversed material, a large switching field is required. This is because of both defects in the crystal structure, in a manner similar to zener drag, and also to do with stray field energy. The polarisation of the material goes from a coupled pattern, with 180° boundaries, to a state in which many heads and tails are separated. This leads to the increase in stray field energy. Therefore, to attain this state, a lot of energy has to be put in by a larger field.

Here we show, how a minor hysteresis loop fits into the major loop.
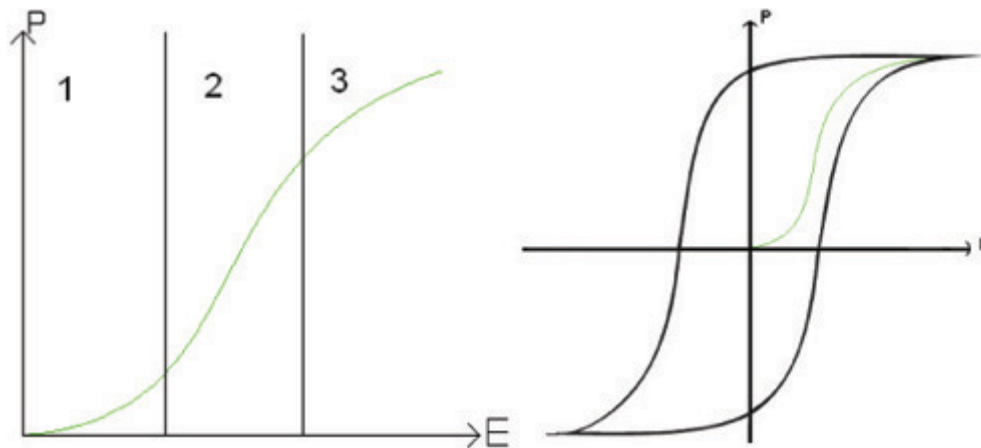
Figure 1.6   Ferroelectric hysteresis loop.

The part of curve shown fits into the major hysteresis curve. Ferroelectrics are very useful for devices and are used in many different ways today. If a ferroelectric is used in its linear region, above T_C (where the ferroelectric domains disappear) it makes a very good capacitor, as its dielectric constant can be very high indeed.

1.3.3   Ferromagnetism

Iron, nickel, cobalt and some of the rare earths (gadolinium, dysprosium, etc.) exhibit a unique magnetic behavior which is called ferromagnetism because iron is the most common and most dramatic example. Ferromagnetic materials exhibit a long-range ordering phenomenon at the atomic level which causes the unpaired electron spins to line up parallel with each other in a region called a domain. Within the domain, the magnetic field is intense, but in a bulk sample the material will usually be un-magnetized because the domains will themselves be randomly oriented with respect to one another to minimize the magnetostatic energy. Ferromagnetism manifests itself in the fact that a small externally imposed magnetic field can lead to the magnetic domains to line up with each other and the material is said to be magnetized. The

driving magnetic field will then be increased by a large factor which is usually expressed as a relative permeability for the material. It can be mentioned that ferromagnetic domains are similar to the ferroelectric domains. Ferromagnets will tend to stay magnetized to some extent after being subjected to an external magnetic field. This tendency to "remember their magnetic history" is called hysteresis. The fraction of the saturation magnetization which is retained when the driving field is removed is called the remanence of the material, and is an important factor in permanent magnets. All ferromagnets have a maximum temperature where the ferromagnetic property disappears as a result of thermal agitation. This temperature is called the Curie temperature (T_C).

Ferromagnetic materials will respond mechanically to an impressed magnetic field, changing length slightly in the direction of the applied field. This property is called magnetostriction. The long range order which creates magnetic domains in ferromagnetic materials arises from a quantum mechanical interaction at the atomic level [41]. This interaction is remarkable as it locks the magnetic moments of neighbouring atoms into a rigid parallel order over a large number of atoms in spite of the thermal agitation which tends to randomize any atomic-level order. Sizes of domains range from a 0.1 mm to a few mm. When an external magnetic field is applied, the domains already aligned in the direction of this field grow at the expense of their neighbors. If all the spins were aligned in a piece of iron, the field would be about 2.1 Tesla. A magnetic field of about 1 T can be produced in annealed iron with an external field of about 0.0002 T, a multiplication of the external field by a factor of 5000! For a given ferromagnetic material the long range order abruptly disappears at a certain temperature which is called the Curie temperature for the material. The Curie temperature of iron is about 1043 K.

1.4   Incompatibility between ferroelectricity and magnetism

To achieve a multiferroic material the incompatibility between ferroelectricity and magnetism is the first issue we need to address. From the symmetry consideration, ferroelectricity needs broken spatial inverse of symmetry while the time reverse symmetry can be invariant whereas, for (anti)ferromagnetism, the broken time inversion symmetry is prerequisite. Figure 1.7 shows this symmetry requirement of different ordering. Among all of the 233 Shubnikov magnetic point groups, only 13 point groups, i.e. 1, 2, 2′, m, m′, 3, 3m′, 4, 4m′m′, m′m2′, m′m′2′, 6 and 6m′m′, allow the simultaneous appearance of spontaneous electric and magnetic ordering. Even this 13 point group not necessarily satisfy the condition always.
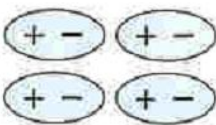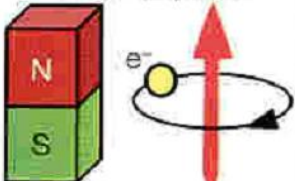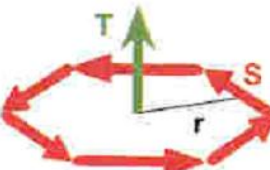
Figure 1.7   Symmetry constraint for different Ferroic order.

This tells why multiferroics are so rare in nature [40]. Definitely the approach will be different from the symmetry consideration to achieve multiferroic materials. Another reason of incompatibility is that all conventional ferroelectric perovskite oxides contain

transition metal (TM) ions with a formal configuration d0, such as Ti^{4+}, Ta^{5+}, W^{6+} (i.e. the TM ions with an empty d -shell). Magnetism, on the contrary, requires transition metal ions with partially filled d shells, as completely filled shells spins add to zero moment and do not participate in magnetic ordering.

1.5   Magnetoelectric multiferroics

Materials, which possess cross-linked responses such as magnetization controlled by electric field and polarization controlled by magnetic field, are actively researched on for the large variety of possible applications. These magnetoelectric multiferroics are extremely significant in the field of memory devices as exemplified by tunnel junctions based on the $BiFeO_3$ system [28, 33, 34]. For practical application, the essential requirements are large value of both the spontaneous polarization, high coupling constant and a good enough insulator. In general, there are a variety of mechanisms that can cause the lowering of symmetry required for a material to exhibit multiferroicity.

1.6   Coexistence of ferroelectricity and magnetism

1.6.1   Independent systems

Borates such as $GdFe_3(BO_3)_4$ is such an example where ferroelectricity comes from active BO_3 groups and magnetism from Fe^{3+} ions [21]. The first route independent system towards perovskite multiferroics was mixing both magnetic TM ions with 'd' electrons and ferroelectrically active TM ions with d^0 configurations at the B-sites while keeping the perovskite structure stabilized. This strategy was first developed by Russian group. $PbFe^{3+}_{0.5}Nb^{5+}_{0.5}O_3$ (PFN) is another such example in which Nb^{5+} causes ferroelectricity and Fe^{3+} causes magnetism. The ordering temperatures are 385 K for ferromagnetism and 183 K for ferroelectricity, hence the coupling is very small [22].

1.6.2 Ferroelectricity by charge ordering (CO)

$LuFe_2O_4$ is ferromagnetic due to the presence of Fe magnetic ion [3]. Below Néel's or Curie's temperature, the Fe ions in $LuFe_2O_4$ form a polar arrangement. That is alternative layers get rich in Fe^{2+} and Fe^{3+}. This is known as site-centered and bond-centered charge ordering between Fe^{2+} and Fe^{3+} ions. It induces different dipole moments at different crystallographic sites, thereby inducing a net dipole moment and hence an electric polarization. Fig 1.8 shows charge ordering in bilayered $Lu(Fe^{2.5+})_2O_4$ with a triangular lattice of Fe ions in each layer. The charge transfer from the top to bottom layer leads to net electric polarization.
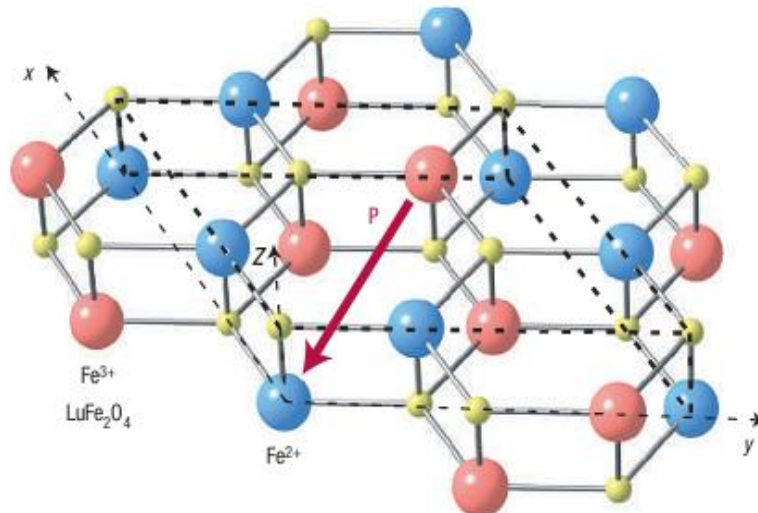
Figure1.8 Ferroelectricity in charge-ordered $LuFe_2O_4$ systems. Red/blue spheres correspond to cations Fe^{3+} and Fe^{2+}.

1.6.3 Geometric Frustration

$YMnO_3$ crystallizes in hexagonal $P6_3mmc$ space group. Due to a large difference in the sizes of Y ion and Mn ion, the MnO_5 polyhedron tilts. Thus, two-thirds of Y ions are distorted upwards and one thirds of Y ions are distorted downwards. This gives a distorted hexagonal structure to $YMnO_3$ [4]. Also, Mn^{3+} ions form trimers (cyclic

compounds). All this leads to a net polarization along the upward direction in the compound. Interestingly, this compound exhibits both ferromagnetic and antiferromagnetic ordering at temperatures $T_N = 80$ K, $T_C = 900$ K respectively. The argument for ferro/antiferromagnetic behavior is spin frustration [3]. Figure 1.9 shows the MnO_5 tilting of $YMnO_3$ [22].
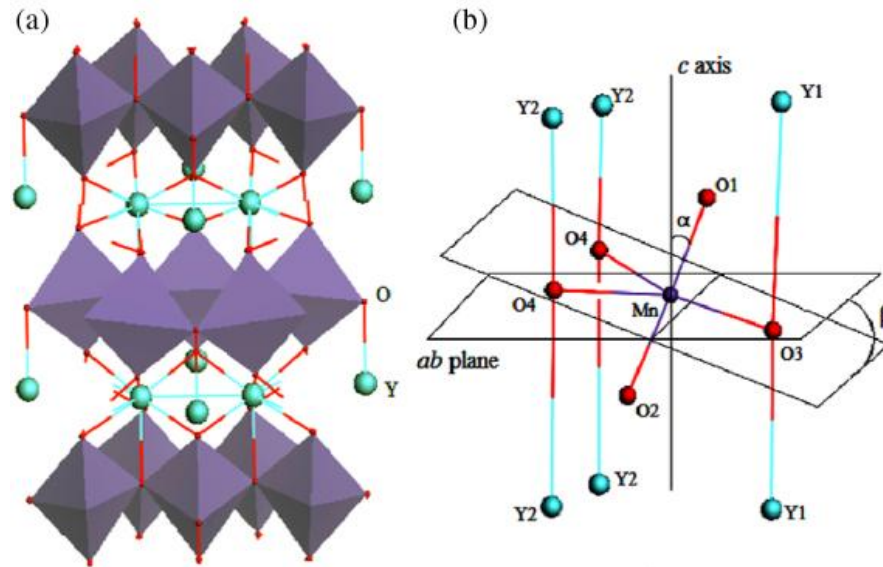
Figure 1.9   Schematic views of (a) the hexagonal $YMnO_3$ (b) the MnO_5 polyhedron with Y layers above and below, the Mn in the center being the doping site.

1.6.4   Lone Pair Driven Ferroelectricity

$BiFeO_3$ exhibits ferromagnetism because of the presence of the Fe magnetic ion (partially filled 'd' orbital) [5]. On the other hand, as the temperature is decreased, due to the presence of the stereo-active lone pair of electrons on the Bi ion, the structure of the compound changes. This lone pair on the Bi ion causes its empty 6p orbital to come closer to oxygen 2p orbital and hybridization between the two occurs. This results in a non-centrosymmetric structure, which is responsible for ferroelectricity.

1.6.5 Magnetism Driven

Complex magnetic ordering

In some multiferroics the centre of symmetry is broken due to the complex magnetic ordering [41]. Fig 1.10 shows the ferroelectric polarization induced by different magnetic ordering such as sinusoidal, cycloidal, conical, etc. Polarization induced by these magnetic ordering would be given by the following equation.

$$P = a \sum_{<i,j>} e_{ij} \times (S_i \times S_j)$$
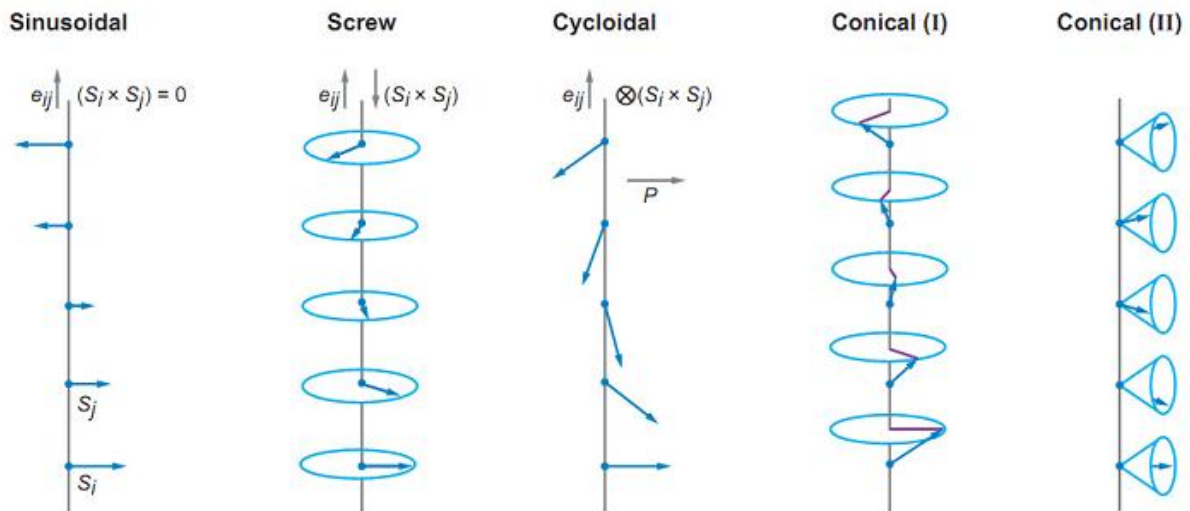
Figure 1.10 Possible collinear and non collinear magnetic ordering.

(a)   Cycloidal ordering

Since the (anti)ferromagnetic and ferroelectric sources are independent in the above mechanisms, there is a weak coupling between the two order parameter. For a strong coupling, ferroelectricity must be induced by magnetism, such as orthorhombic $RMnO_3$, $TbMn_2O_5$, $Ni_3V_2O_6$ and Ca_3CoMnO_6 [6-10]. Here, the coupling is strong because inversion symmetry (a requirement for ferroelectricity) is broken by the magnetic spin ordering. In $TbMnO_3$, Mn^{+3} orders sinusoidally below 42 K which gives net polarization zero according to the above mentioned equation as the direction of spin chain and spin rotation are parallel. But below 27 K, this incommensurate modulated

16

sinusoidal ordering becomes incommensurately cycloidal because of increasing of magnetic moment where the spin chain and spin rotation directions are perpendicular hence a net moment would be developed.

(b)   E – Type Ordering

The non-collinear magnetic structures can be stabilized by either competing interactions (frustration) or anisotropies generated by spin–orbit coupling. These usually lead to reduced transition temperatures and weak induced ferroelectric polarization. In turn, there is another type of so-called collinear multiferroics, which are rare so far but may be more potential since they are less prone to the obstacles mentioned above. One of those comes from E- type antiferromagnetic ordering. In the perovskite manganite series, $HoMnO_3$ was first observed as E-type ordering being multiferroic due to the presence of 'The Exchange Striction Effect', the interatomic distance between parallel spins decreases and the interatomic distance between anti-parallel spins increases [29]. This breaks the inversion symmetry and hence results in a net polarization. A similar E-type ordering induced ferroelectricity is observed in RMn_2O_5 and $RNiO_3$ system [23, 24]

(c)   Longitudinal Spin Ordering

$CoCr_2O_4$ has inverse spinal structure and longitudinal conical spin ordering below the magnetic transition temperature. And again by the Dzyaloshinskii-Moriya Rule, we can see that polarization has non-zero value.

(d)   Disorder-induced

In canted antiferromagnetic oxides such as ortho-ferrites and orthochromites ($YFeO_3$ or $YCrO_3$) with a single ion at the B-site of the perovskite structure, the counter clockwise and the clockwise spin helices are arranged alternatively as shown in Fig. 1.11.a. This

induces the displacement of the oxygen atoms due to inverse DM interaction causing local polarization. In spite of this local polarization, the net polarization in such systems cancels out because of the alternate arrangement of the angles of the canted moments. But it is important to understand that this kind of explanation holds good only for an invariant B-site cation. If there are two different ions in the B-site, A and B, then two arrangements become possible. In the first case Fig. 1.11.b, A and B ions are in alternating position to each other causing oxygen displacement and local polarization, but again the net local polarizations gets cancelled because of the alternate change in the direction of the induced local polarization. In the second case Fig. 1.11.c, random arrangement of A and B cations at the B-site causes not only local polarizations but also a net induced polarization in the system because in such cases the oxygen displacements are not equivalent.
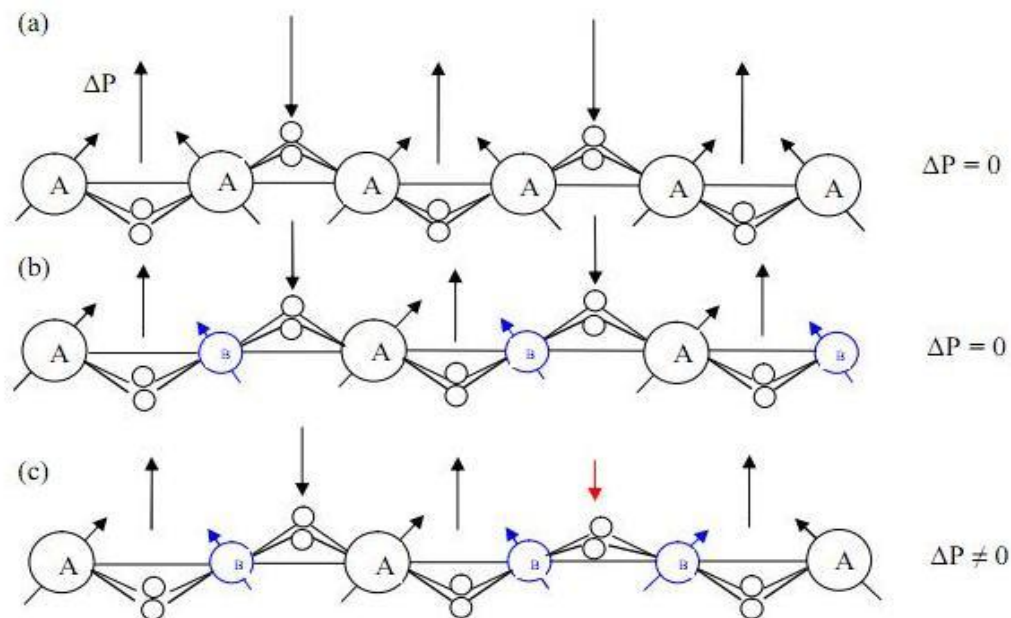
Figure 1.11 Schematic of evolution of ferroelectricity due to disordered spin as adopted from reff.

(e)   Field-induced polar order (RCrO$_3$)

In RCrO$_3$, where R is magnetic rare earth, the very process of measuring polarization, which involves the poling procedure is proposed to cause some small distortion of R ions and their surrounding, producing odd contribution to the crystal field of R and triggering, "releasing" the exchange-striction mechanism [13]. The poling field reduces the symmetry, and the metastable state thus formed can survive after the poling field is released. The main part of polarization arises due to the R-Cr exchange striction, which strongly enhances the distortion initially caused by the poling field. Thus, the poling acts as a trigger, and the metastable "self-poled" state created below T_N^{Cr} is the state which displays a relatively large measured polarization. This picture agrees with the general experimental conclusions summarized for RCrO$_3$. The dominant contribution to the exchange striction comes from the isotropic Heisenberg-like R-Cr exchange. A purely antiferromagnetic G-type ordering of Cr sublattice would not lead to a net non-zero striction, but if there exist weak ferromagnetism of Cr, there would be nonzero striction of the same sign at every (magnetic) R ion, i.e. there would appear net polarization lying in ab-plane. In principle there may also appear effects due to an antisymmetric R-Cr interaction, which could also contribute to polarization.. But in general we expect that such contributions to polarization to be weaker.

1.7   Motivation

This thesis work was motivated for synthesizing new multiferroics expecting large polarization and large magnetoelectric coupling at room temperature. NaRMnWO6 (R≐La, Nd, Tb etc) is expected to show ferroelectricity due to non-centrosymmetric structure [25]. Furter, theory predicts to have a large polarization [27]. TbMnO$_3$ is a

very important material with magnetically induced ferroelectricity at low temperature. With the same structure $SmMnO_3$ does not show multiferroic property due to unsufficient frustration in the ab plane however it has higher magnetic ordering temperature. We have made materials analogous to the $TbMnO_3$ like $Sm_{1-x}Sc_xMnO_3$(x=0.1,0.15,0.2,0.25,0.3) and $Nd_{1-x}Sc_xMnO_3$ (x=0.1,0.15,0.2,0.25,0.3) which shows ferroelectricity. We have discussed possible mechanism for the same. $SmCrO_3$, $SmFeO_3$ are reported to be ferroelectric below its magnetic ordering temperature but with the different proposed mechanism. Since Mn has orbital ordering and strong anisotropic effect it would be immense interest to introduce some disorderness in the Cr and Fe site with the Mn and look at the multiferroic properties on those materials. We have observed ferroelectricity in $SmMn_{0.5}Cr_{0.5}O_3$ where as we also have synthesized $SmFe_{0.5}Mn_{0.5}O_3$ and $SmFe_{0.5}Cr_{0.5}O_3$ but the ferroelectric measurement has been kept for further work due to time limit.

1.8 Bibliography

1. J.G. Zhu, Y.F. Zheng, and G.A. Prinz. *Journal of Applied Physics.* **87**, 9, (2000).

2. J.S. Moodera, L.R. Kinder, T.M. Wong, and R. Meservey. *Phys. Rev.L.* **74**.16 3273(1995).

3. J. V. D. Brink and D. I. Khomskii, *J. Phys. Cond. Matter*. **20**, 434217 (2008).

4. H.Sugie, N. Iwata and K. Kohn, *J. Phys. Soc. Jpn* **71,** 1558 (2002).

5. Y. F. Popov, A.M. Kadomtseva, G.P. Vorobev and A. K. Zvezdin, Ferroelectric **162**, 135 (1994).

6. K. Saito and K. Kohn, *J. Phys. Cond. Matter* **7**, 2855 (1995).

7. S-W. Cheong and M. Mostovoy, *Nature Mate*r. **6**, 13 (2007).

8. J. Okamato et al., *Phys. Rev. Lett*. **98**, 157202 (2007).

9. H. Wu et al., *Phys. Rev. Lett*. **102**, 026404 (2009).

10. T. Kimura et al., *Nature* **426**, 55, (2003).

11. B. Lorenz, Y-Q. Wang and C-W. Chu. *Phys. Rev. B*. **76**, 104405, (2007).

12. B. Rajeswaran et al., *Chem. Mater*. **24** (2012).

13. B. Rajeswaran et al., *Phys. Rev. B* **86**, 214409 (2012) (b) B. Rajeswaran et al., *EPL* **101**, 17001 (2013).

14. C.B. Sawyer and C. H. Tower, *Phys. Rev* **35**, 269 (1930).

15. P.Curie, J. Phys. **3**, 393 (1894).

16. L.D. Landau and E. M. Lifshitz, Electrodynamics of continuous media (Fizmatgiz, Moscow) (1959).

17. I. E. Dzyaloshinskii, *JETP Lett.***10**, 628 (1959).

18. D. N. Astrov, *JETP Lett.* **11**, 708 (1960).

19. H. Schmid, Ferroelectric **162**, 317 (1994).

20. E. Asher, H. Rieder, H. Schmid and H. Stossel, *J. Apply. Phys.* **37**, 1404 (1996).

21. A.F. Gavriliuk et al., *JETP Lett.* **80**,426 (2004).

22. Ning Jiang and X Zhang *J. Phys. Condens. Matter* **24,** 235402, (2012)

23. Gianluca Giovannetti, Sanjeev Kumar, Daniel Khomskii, Silvia Picozzi and van den Jeroen Brink. *Phys. Rev Lett.* **103**, 156401, (2009).

24. T. Kimura, *Annu. Rev. Mater. Res.* **37**, 387, (2007).

25. G. King, S. Thimmaiah, A. Dwivedi, P.M. Woodward, *Chem. Mater.* **19,** 6451, (2007).

26. B. Rajeswaran, P. Mandal, Rana Saha, E. Suard, A. Sundaresan, and C. N. R. Rao *Chem. Mater.* **24**, 3591, (2012).

27. T. Fukushima, A. Stroppa, S. Picozzi and J. M. Perez-Mato. *Phys. Chem. Chem. Phys.* **13**, 12186, (2011).

28. H. Bea, M. Bibes, S. Cherifi, F. Nolting, B. Warot-Fonrose, S. Fusil, G. Herranz, C. Deranlot, E. Jacquet, K. Bouzehouane, A. Barthelemy, *Appl. Phys. Lett.* **89**, 242114, (2006).

29. L. J. Wang, Y. S. Chai, S. M. Feng, J. L. Zhu, N. Manivannan, C. Q. Jin, Z. Z. Gong, X. H. Wang, and L. T. Li , *J. Appl. Phys.* **111**, 114103, (2012).

30. G. Lawes et al, *Phys. Rev. Lett.* **95**, 087205, (2005).

31. T. Kimura, J. C. Lashley, and A. P. Ramirez, *Phys. Rev*. **B73**, 220401, (2006).

32. J. L. Zhu, S. M. Feng, L. J. Wang, C. Q. Jin, X. H. Wang, L. T. Li, Y. C. Li, X. D. Li, and J. Liu, *High Press. Res.* **30**, 265 (2010).

33. P. Mandal et al., *Phys. Rev. Lett*. **107**, 137202, 3591 (2011).

34. N. Dasari et al., *EPL* **99**, 17008 (2012).

35. URL: http://www.semicon.toshiba.co.jp/eng/product/storage/innovation/ challenge/index.html.

36. H. Ishiwara, M. Okuyama, and Y. Arimoto.Ferroelectric Random Access Memories.Springer, Berlin, (2004).

37. J. F. Scott.Ferroelectric Memories. Springer, Berlin, (2000).

38. N. Hur, S. Park, P. A. Sharma, J. S. Ahn, S. Guha, and S.-W. Cheong. *Nature* **429**, 392, (2004).

39. Th. Lottermoser, Th. Lonkai, U. Amman, D. Hohlwein, J. Ihringer, and M.Fiebig. *Nature*. **430,** 541, (2004).

40. N. A. Hill. *Journal of Physical Chemistry.* B**104**, 6694, (2000).

41. M. Kenzelmann, A. B. Harris, S. Jonas, C. Broholm, J. Schefer, S. B. Kim, C. L. Zhang, S.-W. Cheong, O. P. Vajk, and J. W. Lynn. *Phys. Rev. L.* **958**, 087206, (2005).

42. M. Fiebig, Thomas Lottermoser, D. Fröhlich, A.V. Goltsev, and R.V. Pisarev. *Nature*. **419**, 818, (2002).

Chapter 2

Experimental techniques

The details of preparation method of sample and physical measurement techniques used to characterize the samples studied in this thesis are described in this chapter.

2.1   Synthesis of Materials by Solid State Reaction

For synthesizing polycrystalline materials through the solid state reaction, it is necessary to form a new or modified a crystal structure; hence high energy conditions are required. The powders (typical particle size $< 10\,\mu\,m$) of suitable starting materials are ground together in the correct stoichiometric proportions using an agate mortar and pestle. For the work presented here, high purity binary oxides or carbonates of the corresponding cations were used. Grinding the mixture for a longer time results in a homogenous mixture that is very important for solid state reaction. At elevated temperatures, there will be sufficient energy for the constituent ions to migrate through interface which exists between crystal faces of reactant particles and product particle will begin to form. Solid state reactions are very slow because of slow diffusion process. The grain size of product increases as the reaction proceeds. Regrinding and mixing makes new interface between the reacted and un-reacted particles thereby increasing the efficiency of the reaction. The rate of solid state reaction can be increased further by compressing the powder in pellet forms after calcination. This gives small diffusion length and avoids the void space between the reactants. As a matter of fact, well sintered pellets were required for electrical measurement. This can be achieved by heating the pellets at higher temperature for longer duration. The reaction temperature is limited by the melting points of the reactant materials. The rule

of reaction temperature is to heat at 2/3 of the melting point of the reactant material. Sometimes, reducing or oxidizing atmosphere is needed for the required valence state of the cations. The materials, which are very sensitive to the oxidizing atmosphere, inert atmosphere (N_2, Ar) can be used.
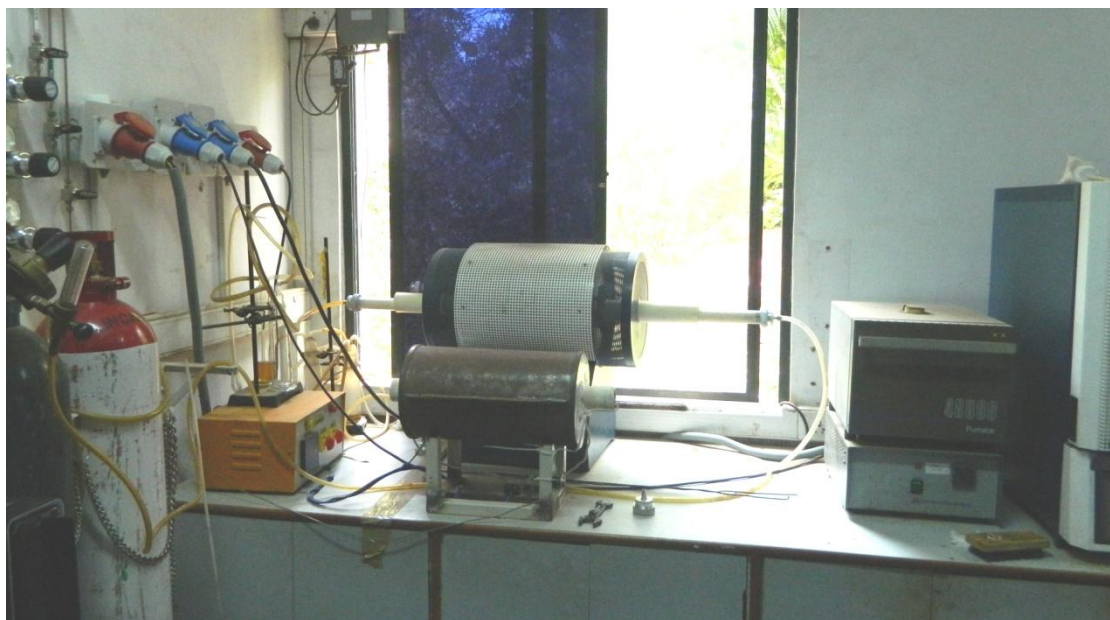
Figure 2.1   Heating arrangements for solid state synthesis.

In our work, most of the materials contain Mn^{+3} cations which can go to Mn^{+4} state while heating at high temperatures in the presence of oxygen. To avoid this, Argon atmosphere was used for synthesizing the Mn^{+3} containing materials. But, there is also a possibility that there is a little amount of oxygen in the commercially available Argon because the boiling point of oxygen and Argon are very near. It was extremely necessary to have only Mn^{+3} valance state of Mn. A mixture of Mn^{+3} and Mn^{+4} valence state can increase the conductivity which is not suitable for electrical measurement. To eliminate the oxygen, the Argon was passed through hot copper turnings maintained at $800^{o}C$. For the heating of copper turnings, a new tube furnace was fabricated. The specifications of this furnace are following. The heating element (coil) is made by Kanthal wire of 1mm diameter (obtained from Heat Process Instrument). Total

resistance of the heating element is 30 ohms. Thermal wool is used for insulation and the whole frame is made by iron stands and sheets. A temperature controller has also been installed for controlling the heating rate and duration. This furnace has temperature limit of 1200 $^\circ$C and heating rate of 20 $^\circ$C/min maximum. Figure 2.1 shows the image of fabricated and commercially available furnace(s) and accessories, used for synthesizing the materials.

2.2   X-ray diffraction pattern and Rietveld Refinement

The high symmetry of crystal structure can give a good X-ray diffraction pattern. If the crystal symmetry is high, the diffraction pattern will consist of well defined and well resolved intense peaks, and the intensity of reflected radiation will vary with the 2θ positions, according to the Bragg's law. This pattern will be sufficient for refining to get the exact crystal structure, lattice parameter, atom positions etc. A profile refinement method of powder neutron diffraction data for the nuclear and magnetic refinement was proposed by Rietveld [1, 2]. Later on, X-ray diffraction was also included with this program. Pattern refinement methods fit a calculated profile pattern to observed powder diffraction data in order to refine both structural and instrumental parameters. In order to achieve the global minimum, the Rietveld refinement method requires space group, approximate lattice parameters and atomic positions. Instrument parameters such as wave length of the X-ray are also needed for the calculations. The peak shapes in the X-ray diffraction data is a combination of Gaussian and Lorentzian functions. The whole method based on the least square of the difference of observed and calculated pattern. If the observed intensities of scattered radiation are y_i for i^{th} data point ('i' denoting 2 θ increment) in the powder diffraction pattern, and calculated intensity is y_{ci}, the relation between them will be the following.

$$y_{c1} = k \, y_1$$

$$y_{c2} = k\, y_{c2}$$

$$\ldots\ldots\ldots$$

$$y_{cn} = k\, y_n$$

The Rietveld method employs a non-linear least-squares refinement in order to solve the above system of equations. The least-squares refinement aims to minimize the sum of the residual over all data points. The residual least square (S_y) is given by,

$$S_y = \sum_{i=1}^{n} w_i\,(y_i - y_{ci})^2$$

The quality of fit for a Rietveld refinement can be evaluated by a difference plot of the calculated and observed profile patterns which should ideally be a straight line. There are several figure of merit to see the goodness of the refinement. We have used the weighted profile residual (R_{wp}), and the expected profile residual (R_{exp}), which are given by,

$$R_{wp} = \left[\frac{\sum_{i=1}^{n} w_i (y_i - y_{ci})^2}{\sum_{i=1}^{n} w_i (y_i)^2} \right]^{\frac{1}{2}}$$

$$R_{exp} = \left[\frac{n - p}{\sum_{i=1}^{n} w_i (y_i)^2} \right]^{\frac{1}{2}}$$

The goodness of fit (χ^2) is given by the following expression

$$\chi^2 = \frac{\sum_{i=1}^{n} w_i (y_i - y_{ci})^2}{n - p} = \left[\frac{R_{wp}}{R_{exp}} \right]^{2}$$

Theoretically this value should approach unity. But in practice, it varies between 1.2 to 1.8 values for a good fitness of a profile [3]. The X-ray diffraction pattern, reported here, was recorded in Bruker D8 Advance Diffractometer.

2.3 Magnetic measurement set up

The magnetic susceptibility measurements, reported in the thesis were performed using Magnetic Property Measurement System (MPMS) which involves superconducting quantum interference device (SQUID) and vibrating sample magnetometer in the temperature range between 2 K to 390 K.

2.3.1 Details of the SQUID Magnetometer

A SQUID Magnetometer of the type Quantum Design MPMS - VSM is build with a helium cryostat and superconducting magnet. A schematic diagram is given in fig 2.2. The helium gas controls the sample temperature. The SQUID detector is a Josephson contact loop which is placed at the core of the apparatus. This is exposed to the field of superconducting magnet and gradually moved through a pick-up coil system.
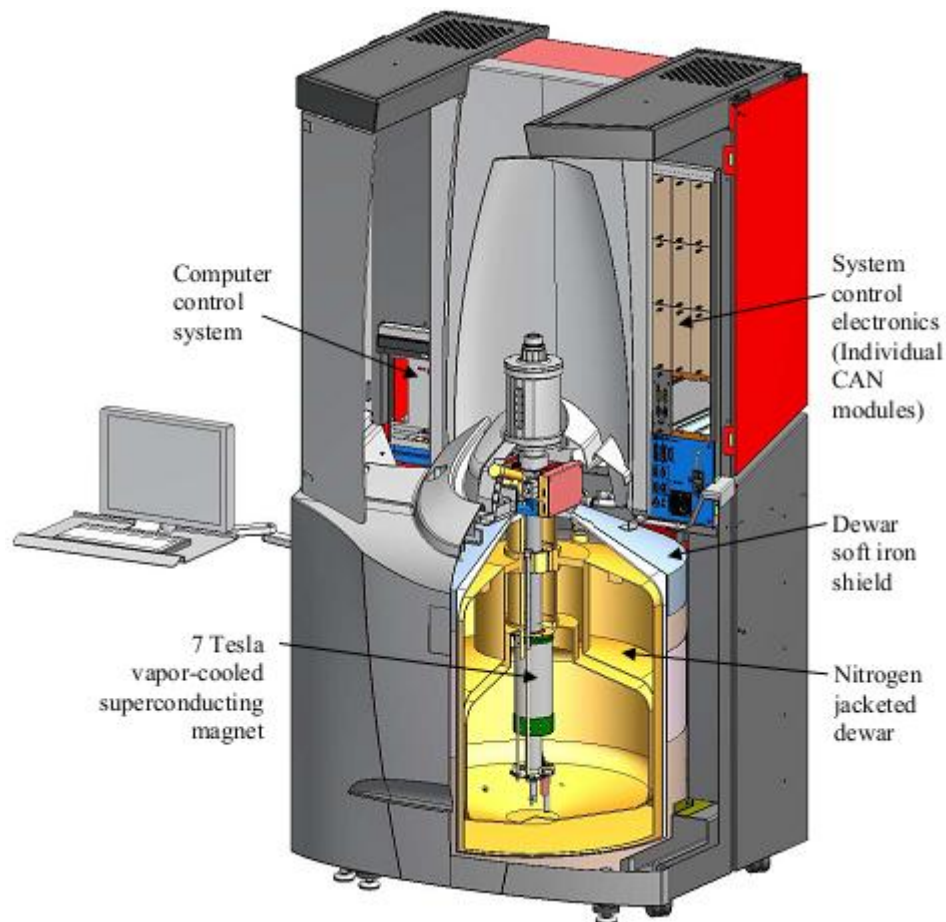
Figure 2.2   Cutaway view of MPMS SQUID VSM

The pick-up coil system is an arrangement of induction coil where the upper and lower single turns are counter wound with respect to the two-turn centre coil [12]. This arrangement rejects interference from nearby magnetic sources. The sample magnetization induces a voltage when it vibrates through the coil according to the Faraday's law. The SQUID detector measures this induced voltage and change it to the magnetization by software. If the oscillation of the sample is sinusoidal then the induced voltage (V_{coil}) is given by,

$$V_{coil} = 2\pi f C m A sin(2\pi f t)$$

Where f and A is the sample oscillation frequency and amplitude respectively, m is the magnetic moment of the sample and C is the coupling constant.

2.3.2 Procedure for magnetization measurements

The sample is mounted on a quartz sample holder with the help of a stand, provided with a mirror for centering the sample position. The quartz holder is attached in the sample probe, which is inserted into the sample chamber of the SQUID. The sample is magnetized by a constant magnetic field and the magnetic moment of the sample is measured, producing a DC magnetization curve M(H) with temperature. During Field Cooled (FC) measurements, a constant field is applied while cooling and the magnetization data is recorded in presence of the constant field. For Zero Field Cooled (ZFC) measurement, no field is applied while cooling and data is recorded in presence of a constant field.

2.4 Pyroelectric current measurement

Pyroelectricity is the ability of certain materials to generate a temporary voltage when they are heated or cooled. The change in temperature modifies the positions of the atoms slightly within the crystal structure, such that the polarization of the material changes[5]. The temporary voltage drives a small current through its internal leakage

path or through outside circuit if it is connected. Now if there is a phase transition from paraelectric to ferroelectric state, there will be change in the pyrocurrent at the transition temperature. This change in the pyrocurrent can be measured after poling the sample from paraelectric to ferroelectric state by applying voltage while cooled through transition temperature. But the major problem we face in this measurement is leakage. There exists a certain value of background current (which ideally should become zero after some time, at a constant temperature) due to finite conductivity of the sample arising from trap charge at the grain boundary, defects, void spaces etc. This can be avoided by achieving a good sintered stoichiometric sample or single crystal so that, the grain boundary and other contribution such as defects, impurity would be less [6]. A special care should be taken for this measurement as artifacts can also cause the pyrocurrent peak. A proper electrode (which could be silver epoxy or gold) should be painted on the surface of the sample to make a parallel plate capacitor. A proper arrangement of circuit with suitable cable (good quality cable which has very less resistance) of minimum length and properly shielding (electromagnetic radiation from the enviroment can also induce voltage and contribute to the current) is also very important. After poling, the capacitor made from the sample is shorted for some time (for highly leaky sample time could be few hours) so that the leakage contribution or the background current level would be decayed. After this, the actual pyrocurrent can be measured with a very sensitive and accurate electrometer. In our work, we have measured this pyrocurrent by Keithley 6517A electrometer. The measured current can be integrated with time to get the polarization. The equation would be

$$P = \frac{\int I dt}{A}$$

Where I is the measured pyrocurrent and A is the area of the sample.

The sample was mounted in a modified multi-probe which was inserted to the sample chamber of PPMS (Physical Property Measurement system) where helium cryogenic system is used for cooling of the sample and one can apply a maximum field of 9 T. We can measure the pyrocurrent in presence of magnetic field as well. A picture of the whole set up is given in fig 2.3.
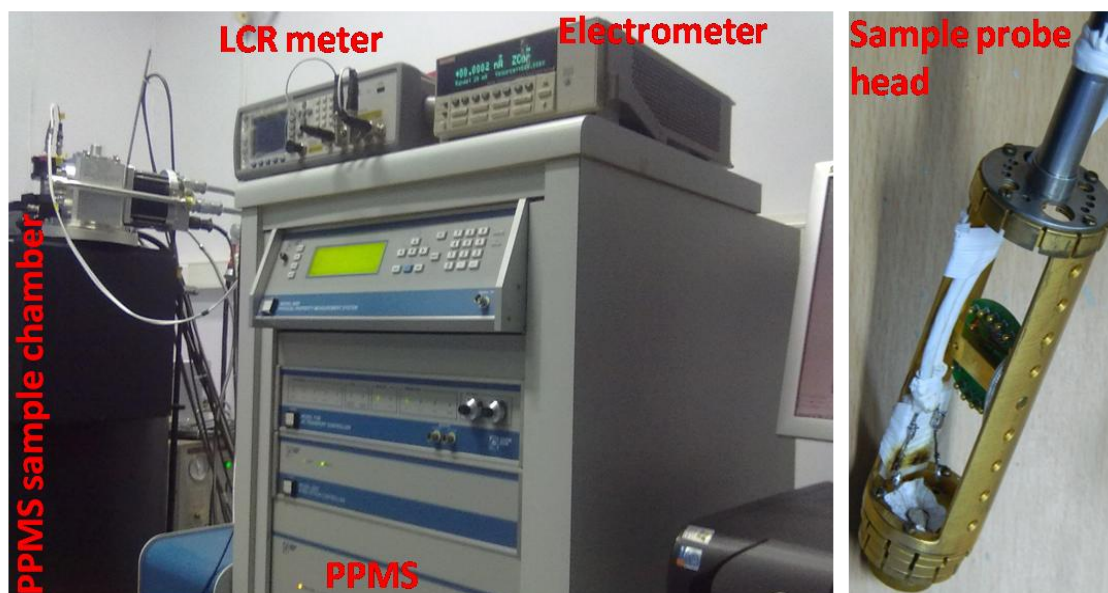
Figure 2.3 Left panel - Physical Property measurement System arranged with electrometer and LCR meter; right panel - sample probe head.

2.5 P-E Loop measurement

The conventional and straightforward way of ferroelectric measurement is P-E Loop which is measured using a Sawyer-Tower circuit (fig2.4) [8]. In this measurement, the sample is connected in series with known capacitor so the total charge stored in the sample can be known by calculating the charge stored in the standard capacitor with the given voltage since the stored charge cannot be measured directly. The charge can be integrated out with time to calculate the polarization. A triangular voltage pulse is given for measuring the P-E loop.
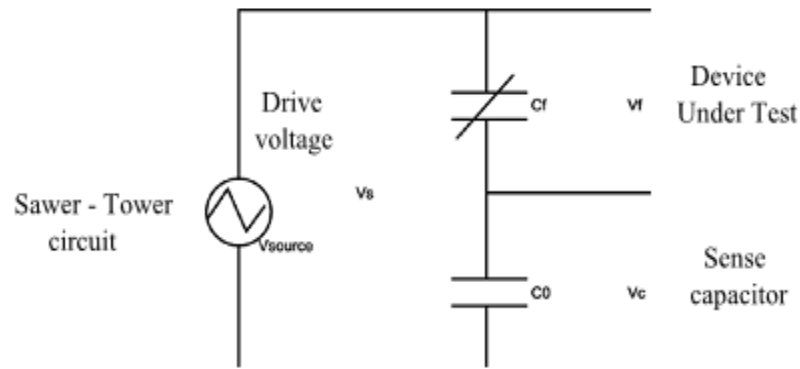
Figure 2.4   Standard Sawyer-Tower circuit diagram.

The triangular voltage pulse consists of step increment of voltage as shown in fig 2.5.
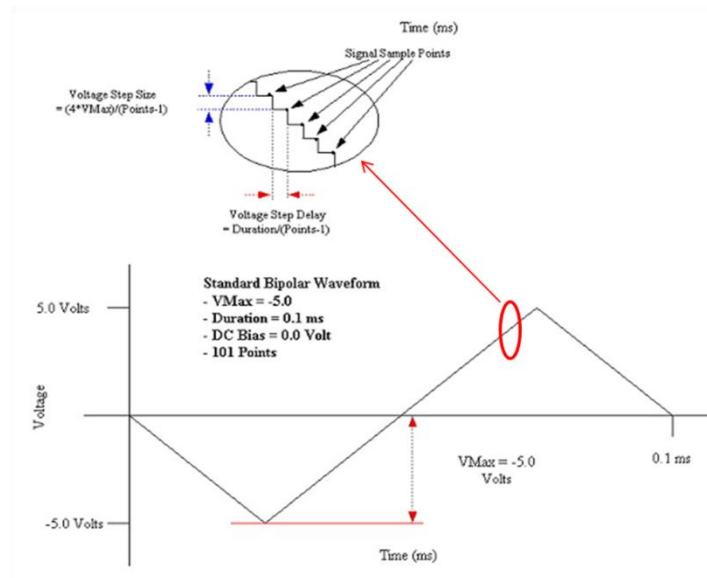
Figure 2.5   Triangular voltage pulse, Zoomed area shows step increment voltage.

In particular the change of voltage can lead to a change in current which in turn changes the charge stored that is integrated with time. It is important to note that polarization being a relative quantity, a preset pulse is given before measuring the actual polarization of the triangular pulse to set a known polarization which is taken as the base point for the measurement. The whole set up of the measurement is inbuilt with Precision Workstation Ferroelectric Tester from Radiant Technology. The sample may not be always ideal ferroelectric. In fact, when the value of ferroelectric polarization is very less and the other contributions such as capacitive, resistive or a

combination of both are relatively high, the PE Loop would be very different to the ideal loop. The different PE loops that one can obtain for such samples are given in fig. 2.6 to compare with our result. Finally, an ideal PE loop with all the important parameter is also given in the fig.2.7.
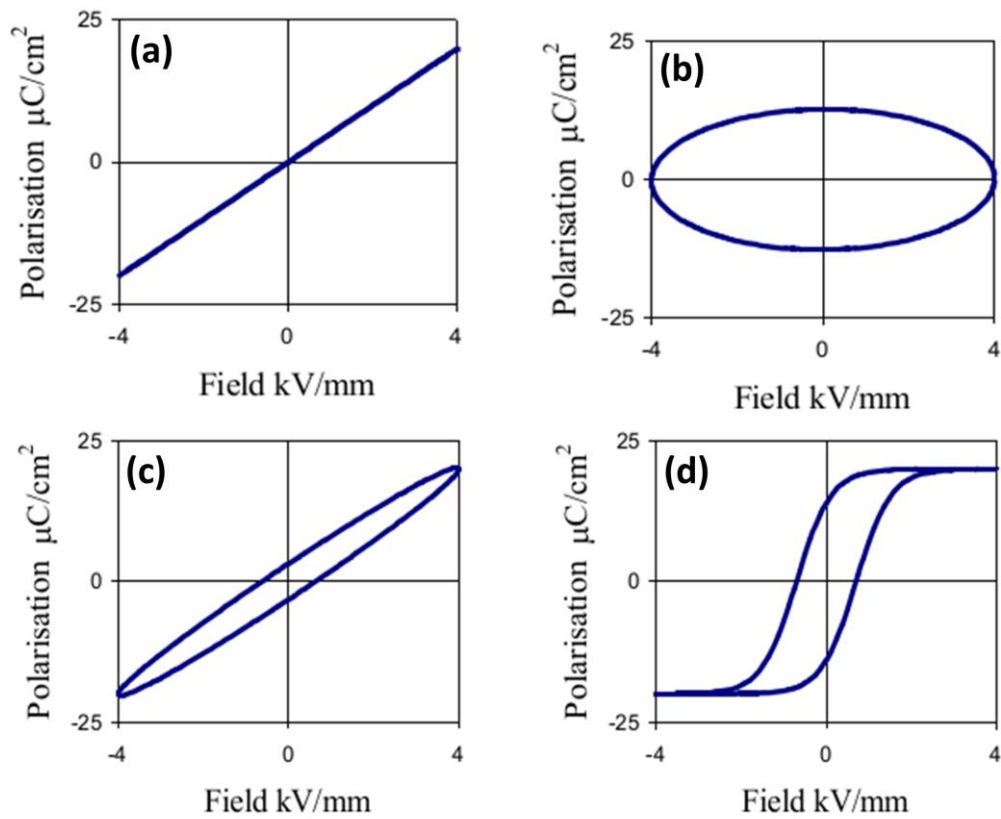
Figure 2.6   (a) Ideal linear capacitor response, (b) Ideal resistor response, (c) Lossy capacitor response and (d) Non linear ferroelectric response.
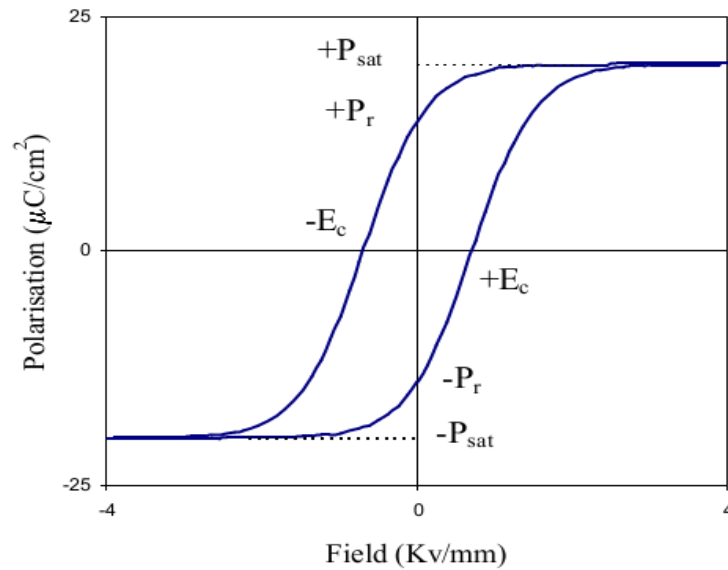
Figure 2.7   P-E Hysteresis loop parameters for a ferroelectric material.

2.6   Piezoelectric measurement

The measurement of strain field loops S-E is obviously important for actuation applications. The slope of the S-E loop is the piezoelectric coefficient, d_{33}, one of the most important design parameters for use as actuators.
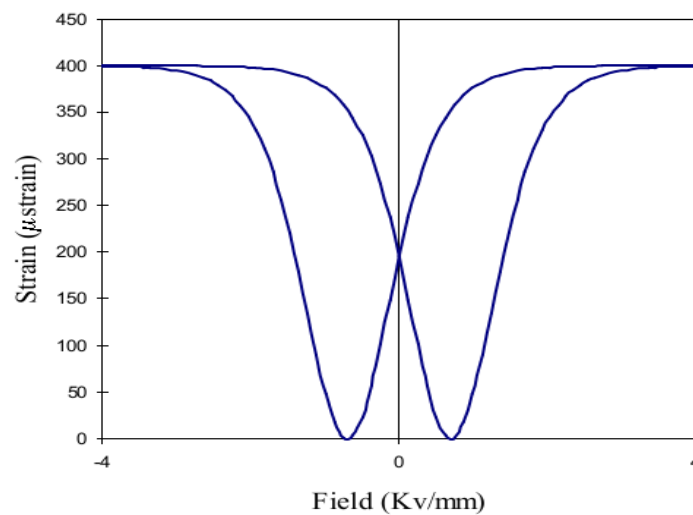
Figure 2.8   Schematic of a S-E loop exhibiting a butterfly loop

Measurement of S-E loops also allows investigation of the onset of massive non linearity in the strain with the appearance of 'butterfly loop'. The strain is often, but not always, proportional to the square of the polarization. The strain can be measured by

35

using a photonic sensor connected with the above mentioned P-E Loop measuring set up. A Schematic of a S-E loop exhibiting a butterfly loop is shown in the fig. 2.8.

2.7   Double Wave Method (DWM)/ Positive Up Negative Down (PUND)

When the intrinsic polarization value is less compared to the other effects (discussed in the last PE-Loop measurement technique), it becomes very difficult to measure the intrinsic polarization [6]. The issue is closely related to the experimental difficulty in determining the polarization of polycrystalline specimens particularly with considerable conductivity by conventional PE-loop measurement or Pyroelectric current measurements performed after a poling procedure under high dc electric fields which causes a high leakage current. The major problem that we encounter with polycrystalline samples are grain boundary, porosity and oxygen non-stoichiometry which causes large leakage current and space charge effects [23]. The space charge refers to the surface charges that can be trapped in the grain boundary of the polycrystal or the ferroelectric domain boundary during an electric poling procedure. This does not allow a complete poling of the sample. To overcome this problem, we have used a recently developed technique Double Wave Method (DWM) and also called positive-up negative-down (PUND) method, which uses successively two positive and two negative electrical pulses, to directly measure P-E hysteresis loops [9]. It can be noted that even in this measurement there is a preset pulse before measuring the final loop. After pre-poling, the polarization value is taken as zero and the measurement of polarization for the given PUND pulse begins. The full analysis of the data and technique is explained by fig. 2.9.
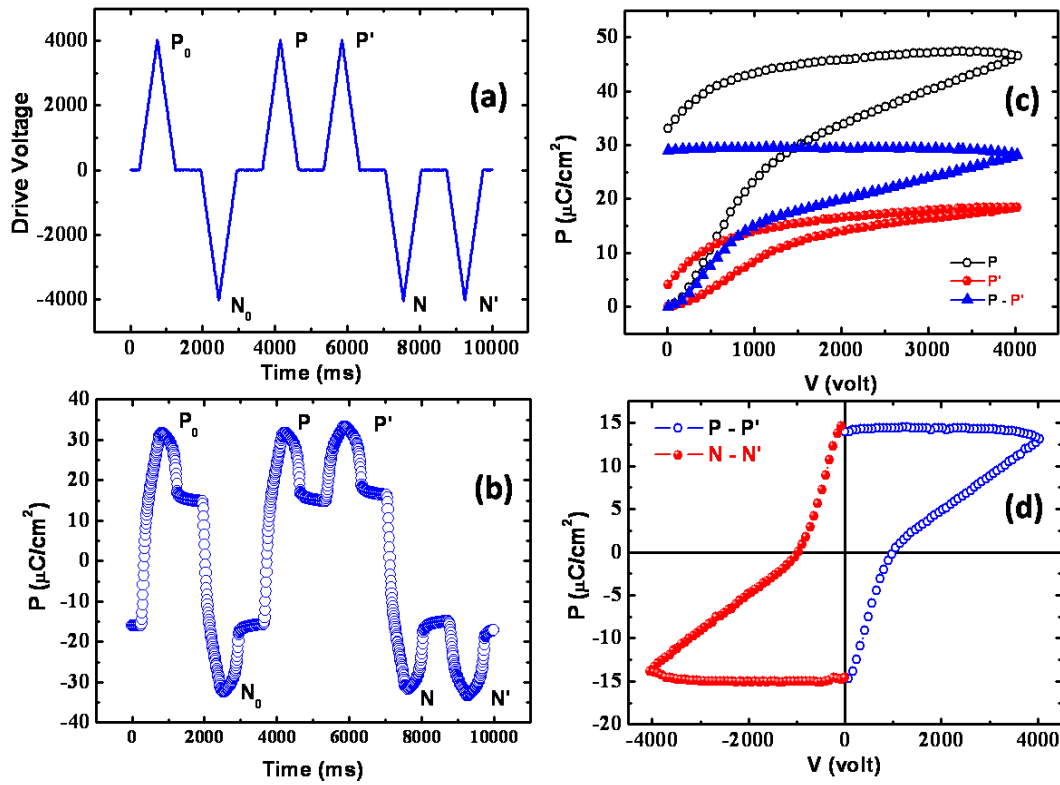
Figure 2.9 DWM result of BaTiO$_3$ (a) The drive voltage profile for measuring the polarization, (b) the response polarization of BaTiO$_3$ for the given voltage profile, (c) extracted polarization value for the P (total polarization including ferroelectric part) and P′(excluding ferroelectric part) pulses, origin of polarizations shifted to zero, blue curve shows the subtracted polarization value, contain only ferroelectric polarization and (d) shows the complete ferroelectric loop, combining the P-P′ and N-N′, where value is shifted by the factor of half to calculate the remnant polarization.

PUND results can be analyzed by time-dependent current curve also. The measured charge can be differentiated with time to get the current. Current can be converted into current density by dividing with the thickness of the sample. Ferroelectric components is marked by its peak-like feature in the response pulses of Positive (P) and Negative (N) electric fields, while they are absent for those of Up (P′) and Down (N′) electric fields. Figure 2.10 explains this result [11].
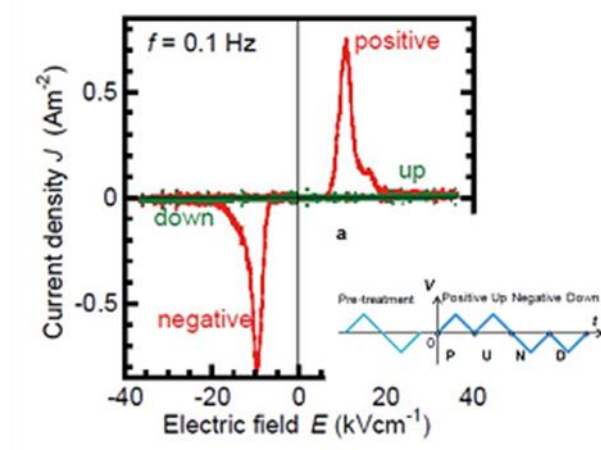
Figure 2.10   Current density v/s Electric field graph, can be extracted from PUND result. Red curve shows the ferroelectric peak for the both Positive (P) and Negative (N) pulses, green curve shows the absence of ferroelectric polarization in the Up (P′) and Down (N′) pulses.

2.8   Second-Harmonic Generation (SHG) measurement

Second-harmonic generation (SHG), or frequency doubling, can be defined as the conversion of a wavelength of light into half its original, i.e. $\lambda_1 \rightarrow \frac{1}{2}\lambda_1$ which can be exhibited by a non centrosymmetric material. Usually a commercially available Nd-YAG laser (1064 nm output) is used for this measurement. The output of SHG will appear in the visible range at 532 nm (green), so one can actually visualize the SHG. In the present case, the sample (polycrystalline powder) was placed in a fused silica capillary tube and the measured SHG data was compared with that of the known materials such as Urea and KDP.

2.9   Dielectric measurement

Normally, at the ferroelectric transition is accompanied by a dielectric anomaly. The dielectric constant can be obtained by capacitance measurement and the corresponding energy dissipation can be obtained by loss measurement. The charge stored in a

capacitor is $Q = CV$ where, V is the applied voltage and C is the capacitance. For a parallel plate capacitor, the capacitance can be written as

$$C = \frac{\epsilon_0 \epsilon_r A}{d}$$

Where ϵ_0 and ϵ_r are the permittivity of vacuum and relative permittivity of the media. For a given ac sinusoidal voltage $(v_0 \sin \omega t)$ to measure the impedance of the material, a complex dielectric (ϵ_r^*) constant can be calculated.

$$\epsilon_r^* = \epsilon_r' - j\epsilon_r''$$

And
$$\tan \delta = \frac{\epsilon_r''}{\epsilon_r'}$$

Where ϵ_r' is real (permittivity) and ϵ_r'' is complex quantity.

In the dielectric study the dielectric constant $C = \frac{\epsilon_r'}{\epsilon_0}$ and loss $(\tan \delta)$ is measured with respect to temperature or frequency or both. The frequency dependence of dielectric constant and loss is very important to understand the dielectric nature of a material. For a ferroelectric transition the dielectric constant and the loss both should not change with the frequency. The dielectric loss is indicative of some dielectric relaxation. Dielectric relaxation is the response of non interacting dipoles to an external ac field. Briefly, when an AC signal is applied, the dipoles try to follow the polarity of the signal but after a certain frequency $(f > f_c)$ the dipole cannot follow the polarity and relaxes. In our work, Agilent 4294A Impedance analyzer was used to measure the dielectric constant and loss over the range of frequency 1 kHz to 1 MHz.

2.10   Bibliography

1.   H. M. Rietveld. *Acta Crystallographica.* **22**, 151 (1967).

2.   H. M. Rietveld. *Journal of Applied Crystallography.* **2**, 65 (1969).

3.   Vitalij K Pecharsky, Peter Y Zavalij. *US Springer.* **777**, 133 (1974).

4.   The measurement, instrumentation, and sensors handbook. 32–113 1999.

5.   http://en.wikipedia.org/wiki/Pyroelectricity.

6.   S M Feng, Y S Chai, J L Zhu, N Manivannan, Y S Oh, L J Wang, Y S Yang, C Q in and Kee Hoon Kim. *New Journal of Physics.* **12**, 073006, (2010).

7.   Igor Lubomirsky and Oscar Stafsudd *REVIEW OF SCIENTIFIC INSTRUMENTS,* **83**, 051101, (2012).

8.   C B Sawyer and C H Tower, *Phys Rev.* **35**, 269, (1930).

9.   Fukunaga and Noda. *J. of Phys. Soc. of Japan*, **77,** 064706, (2008).

10.   P. Lunkenheimer et.al. *Nat.Mat*. **11.** 755 (2012).

11.   Nat. Horiuchi and Tokuraet. al. **463**, 789, (2010).

12.   Thesis "SYNTHESIS AND CHARACTERIZATION OF Sm-BASED ORTHOFERRITE COMPOUNDS, SmFe1-xMnxO3"   IBRAHIM BALA USMAN.

Chapter 3

Are the layered and rock-salt ordered perovskite oxides, NaRMnWO$_6$ (R=La, Nd and Tb) multiferroic?

3.1 Introduction

In the history of multiferroic research, there is a classical strategy to make polar, non centrosymmetric oxides, wherein due to the lack of spatial centre of symmetry, ferroelectric polarization appears. Crystallographically, a material can be considered to be a polar if it is a member of one of the following 10 polar crystal classes (1, 2, 3, 4, 6, m, mm2, 3m, 4mm or 6mm) [1]. The materials constituting polar group, can give a lot of interesting and technologically useful properties such as ferroelectricity, piezoelectricity, second order non linear optical behavior etc. For ferroelectric behavior, there is an additional requirement that the polarization has to be switchable (bipolar) with the reversal of electric field. There are some strategies for making polar materials. The presence of Second order Jahn-Teller (SOJT) distortion (octahedrally coordinated d^0 transition metals Ti^{+4}, Nb^{+5}, W^{+6} etc.) and stereo-active lone pair (Te^{+4}, Pb^{+2}, Bi^{+3}, Se^{+4} etc.) electrons in the perovskite oxides have been the most important strategy in ferroelectric material research e.g. BaTiO$_3$ and PbZr$_{0.5}$Ti$_{0.5}$O$_3$. The

perovskite is one of the most flexible and versatile host structures for accommodating a variety of ions and thus give rise to fascinating properties. Perovskites are also known to exhibit multiferroic properties where electric, magnetic or any other ferroic ordering appears simultaneously in one phase. This makes the material interesting from technological as well as scientific point of view. Interestingly, the magnetic and ferroelectric ordering were thought to be mutually exclusive with each based on the mechanism of classical ferroelectrics. Therefore, the first multiferroic material was a great surprise [14, 15]. Later, several new routes have been adapted to find multiferroicity. The perovskites, $BiFeO_3$ and $BiMnO_3$, exhibit multiferroic properties where the presence of stereochemically active Bi^{+3} ions gives ferroelectricity while the Fe^{+3} ions provide magnetism [1, 2]. Many of the improper multiferroic material such as $Tb(Dy)MnO_3$ are also perovskites where incommensurate spiral magnetic ordering has been found to induce ferroelectric polarization.

The ideal perovskite structure is cubic where three dimensional framework of corner sharing BO_6 octahedra forms 12 coordinated surrounding of 'A' site cation. But the possibility of 'A' as well as 'B' site substitutional flexibility and compositional range of both cations make this structure more important and interesting. Recently, a 50:50, in 'B' site as well as in 'A' site substituted double perovskite compound (AABBO6) has drawn much attention where B - B′ cation order in a rock salt fashion and A - A′ cations shows a layered long range arrangement. These compounds are interesting from a structural point of view because 'A' site layered arrangement is rare in stoichiometric perovskite structure, although it is common in non-stoichiometric structural arrangement ($AABBO_5$). Recently 'A' site layered arrangement has been found in some compounds ($NaRMnWO_6$, R = La, Nd, Tb) [5]. It was shown that the layered ordering in the 'A' site gives bond instability which can be compensated by the

presence of a highly charged d^0 cation on one of the B-sites [4, 5]. Fig. 3.1 shows the structure of $NaTbMnO_6$ where we see both the ordering. The presence of four distinct cation sites makes this material more interesting. All these compounds are shown to be crystallize in $P2_1$ symmetry at room temperature [5]. Further, the magnetic ordering is also interesting. $NaLaMnWO_6$, $NaNdMnWO_6$ and $NaTbMnWO_6$ orders antiferromagnetically (AFM) at low temperatures below 15 K [5]. Neutron diffraction in $NaLaMnWO_6$ has shown that the Mn^{2+} ions order commensurately AFM as a consequence of Mn–O–W–O–Mn superexchange. But when Nd is substituted for La^{3+} ions the magnetic sub-lattices order simultaneously into an incommensurate structure. $NaTbMnWO_6$ showed two magnetic phase transitions upon cooling, one at 15 K and another $\approx$ 9 K which is due to the coupling between two different magnetic sublattices Mn^{+2} and Tb^{+3} [6]. So the presence of Jahn Teller W^{+6} ion and magnetic ions makes this family of oxides potentially attractive for multiferroic properties.
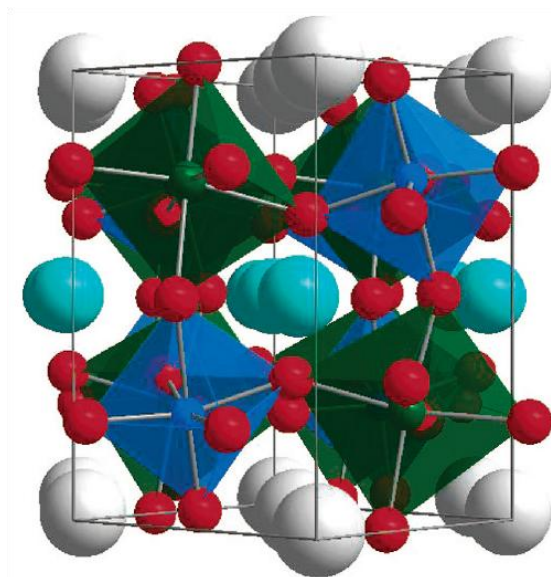
Figure 3.1 Crystal structure of $NaTbMNWO_6$. The blue and green small spheres are W^{+6} and Mn^{+2}, respectively. Small red sphere is O^{-2}. Large light gray and aqua spheres are Na^+ and Nd^{+3} ions, respectively.

Most strikingly, based on the density functional theory and group theory analysis it has been claimed that the calculated electric polarization resulting from the polar distortion can be as large as $16\mu C/cm^2$ [7]. It has been proposed that two octahedral tilting modes and the additional presence of the A-A′ cation ordering makes the structure polar [7].

Therefore, these materials have generated a great deal of interest due to the structural aspects discussed above. We see that there has been a lot of work on these materials in structural as well as magnetism aspects by using monochromatic X-ray and neutron powder diffraction whereas the electrical properties are yet to be explored. So it is very important to measure the electric polarization on these materials. However, although these materials are reported to be non-centrosymmetric, the X-ray and neutron diffraction patterns can be fitted with both $P2_1/m$ and $P2_1$ where the former is centrosymmetric and the later is non-centrosymmetric with a very small difference in intensity and the satellite peaks which makes determination of structure ambiguous. Currently, investigation of centre of symmetry dependent electrical properties like pyroelectricity, piezoelectricity, and ferroelectricity are of great importance. In view of this, we have investigated the electrical properties of three compounds namely, $NaLaMnWO_6$, $NaNdMnWO_6$ and $NaTbMnWO_6$.

3.2   Experimental section

3.2.1   Synthesis

All compounds, reported here, were synthesized by conventional solid state route. The starting materials Na_2CO_3 (from Spectrochem), La_2O_3, Nd_2O_3, Tb_4O_7 (from Alfa Aesar), Mn_2O_3, WO_3 (from Sigma Aldrich) were taken as obtained [99.9%]. Synthesis was aided by use of $MnWO_4$ which was initially made by simply mixing and heating of WO_3 and Mn_2O_3 in air at 1300° C for 24 hours. Since, all the rare-earth (RE) sesquioxides (RE_2O_3) are very sensitive to the carbon dioxide and moisture (formation of $R_2(CO_3)_3$, $3H_2O$, these were preheated at 950^oC for 10 h. Because of the volatility of Na_2CO_3, a 5% extra (according to weight percentage) Na_2CO_3 was used. Finally Na_2CO_3, rare-earth oxide and $MnWO_4$ were mixed thoroughly in agate mortar pestle

and heated at 800 ^{o}C in air for 8 hours. It was again ground and heated at 850 ^{o}C for 6 hours in the form gas (5% H_2 and 95% Ar mixture) to reduce Mn^{+3} to Mn^{+2}. Finally the materials were sintered at 1000 ^{o}C in form gas for 12 hours. Since Na_2CO_3 is volatile, the compounds were not heated above 1000 ^{o}C and for longer duration.

3. 2.2   Characterization by Powder X-ray diffraction

X-ray power diffractions were collected on a Bruker D8 Advance Diffractometer (30kV, 30mA). Scans were recorded over a 2θ range 10° to 80°. Structural refinements were carried out by using Rietveld method.

3.2.3   Magnetic measurements

The variation in magnetic susceptibility with temperature was carried out with a Quantum Design MPMS SQUID VSM in the temperature range of 2 K to 300 K.

3.2.4   Electrical measurement

For electrical measurement silver paint was used to make the electrodes on the polycrystalline sintered samples and DWM for gold. Positive-Up Negative-Down (PUND) or Double Wave Method (DWM) was done in Precession Workstation of Radiant Technology. Piezoelectric measurements were also performed by ferroelectric tester of Precession Workstation by Radiant Technology. Dielectric properties were measured in Agilent E4980A LCR meter and pyrocurrent was recorded by Keithley model 6517A electrometer in the 10 K to 320 K temperature range. Second Harmonic Generation (SHG) measurements were done by DCR-11 Laser with 1064 nm wavelength [13].

3.3   Results and discussion

3.3.1   Structure

The XRD pattern of NaTbMnWO$_6$ showed a small impurity peak which were assigned to Tb$_4$O$_7$. Additional heating cycles were unsuccessful for eliminating this impurity. X-ray pattern along with Rietveld refinement have been shown in the fig 3.1. a, b, c. The color of the NaRMnWO$_6$ (R = La, Nd, Tb) varied depending on the synthesis temperature. After first heating, they appeared green and turned yellow when sintered at 1000 °C. The powder X-Ray Diffraction patterns of these compounds with different color were indistinguishable. The green color is because of the presence of Mn^{+3} ions in trace amount which could go to Mn^{+2} by further heating in form gas at 1000 ^{o} C [5].

A detailed crystallographic study is reported for the similar kind of materials based on HRTEM, synchrotron X-ray, neutron diffraction where both 'A' site and 'B' site cation ordering give incommensurately modulated crystal structure [9, 5, 6]. The modulation depends mainly on the tolerance factor, where the assignment to the space group P2$_1$/ m (centrosymmetric) is consistent with the 'out of phase' rotation a$^-$a$^-$c^0 of the octahedra. Further decreasing the size of 'A' site cation gives another 'in phase' rotation (a^{0}a^{0}c$^+$) and finally it becomes (a$^-$a$^-$c$^+$) which corresponds to P2$_1$ (non-centrosymmetric) space group. The presence of the additional rotation is important because it destroys the inversion center and allows the formation of a polar structure. It is proposed that SOJT distortion drives a displacement of the W^{+6} cation, which in turn stabilizes layered ordering of the Na$^+$ and (La^{3+}, Nd^{+3} or Tb^{+3}) cations. These two distortions are inter-related to each other and the removal of one leads to the disappearance of the other. It is very difficult to solve the crystal structure from the power X-ray diffraction as it is a (3+2) dimensional ordering i.e. rock-salt ordering and chessboard ordering.

Fig 3.2. a, b, c shows the Rietveld refinement on the room temperature powder X-ray of $NaLaMnWO_6$, $NaNdMnWO_6$ and $NaTbMnWO_6$, respectively. These show a very good agreement to the reported X-ray diffraction analysis [5]. All the compounds are fitted well with the $P2_1$ space group. The lattice parameters of all these compounds, extracted from Rietveld refinement, are shown in table 3.1. It is observed that the lattice parameters are decreasing with the decreasing tolerance factor which is expected if the octahedral tilting distortion increases with the decreasing of tolerance factor [16]. Tolerance factor is calculated based on the average cation size for both 'A' and 'B' site. $P2_1/m$ can also fit the X-ray pattern but neutron diffraction study, as reported gives better goodness of fit with the $P2_1$ space group [5].

Table 3.1   Lattice parameters, tolerance factor (t) and color of the compounds, $NaRMnWO_6$ (R= La, Nd and Tb) with the monoclinic structure (space group $P2_1$)

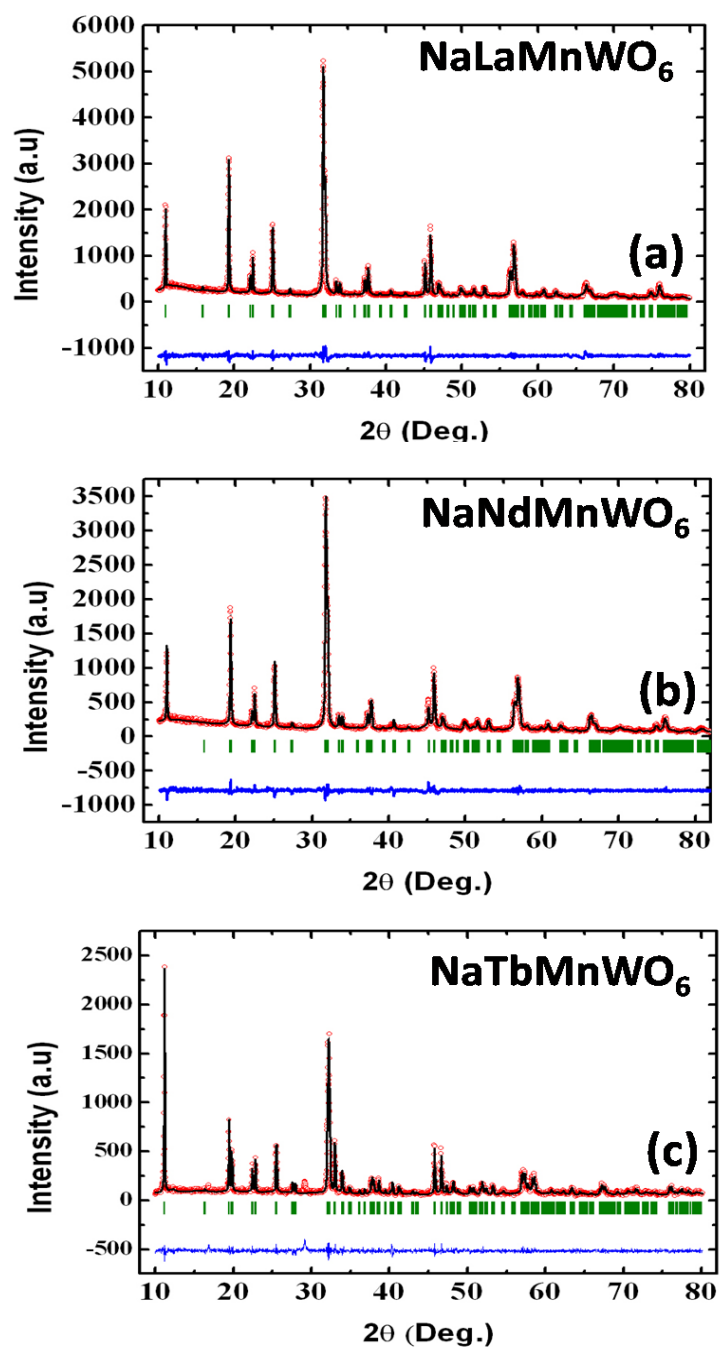| Compound name	a (Å)	b (Å)	c (Å)	β (deg)	Cell volume (Å)^3	t	Color
$NaLaMnWO_6$	5.5890(2)	5.5990(2)	8.0328(3)	90.218(3)	251.37(2)	0.93	Greenish-yellow
$NaNdMnWO_6$	5.5113(3)	5.5926(4)	7.9842(5)	90.373(2)	246.09(2)	0.91	yellow
$NaTbMnWO_6$	5.4245(3)	5.5847(3)	7.9243(4)	89.645(2)	240.06(2)	0.91	Yellow

Figure 3.2   Rietveld refinements on room temperature powder X-ray patterns. (a) NaLaMnWO$_6$, (b) NaNdMnWO$_6$, (c) NaTbMnWO$_6$. Red circles, black lines, blue lines below, green vertical lines are representing observed, calculated, difference intensity and Bragg's positions, respectively.

3.3.2   Magnetic Properties

Figure 3.3 shows magnetic moment versus temperature data and Curie-Weiss. It is observed that all three samples order antiferromagnetically at low temperature within 6 K to 15 K. The Néel temperature for all the compounds has been shown in the table 3.2. From the Curie-Wiess plot, the Wiess constant and effective moment (μ_{eff}) have been calculated from the best fit linear regime (150 K to 300 K) and compared with the theoretical value in the table 3.2. This shows a good agreement with the reported value and observed value. Using the relation $\mu = g(S(S + 1))^{1/2}$, μ_B is 5.92 for Mn^{+2}, where g = 2.0023 and S = 5/2. For the sample containing magnetic rare-earth the total magnetic moment were be calculated by this formula $(\mu_{total})^2 = (\mu_{Ln})^2 + (\mu_{Mn})^2$. We also see that the magnetization in $NaTbMnWO_6$ increases at low temperature, which is [3,5,10]. The low temperature antiferromagnetic ordering could be explained by the trilinear coupling of Mn^{+2} i.e. Mn^{+2}-O-W^{+6}-O-Mn^{+2} due to superexchange interaction. So, the lower cation size should give higher T_N as the average bond distance decreases [table 3.2].

Table 3.2   Weiss constant, μ_{eff}, T_N (K) and tolerance factor (t) of ($NaRMnWO_6$: R= La, Nd and Tb)   * to be calculated

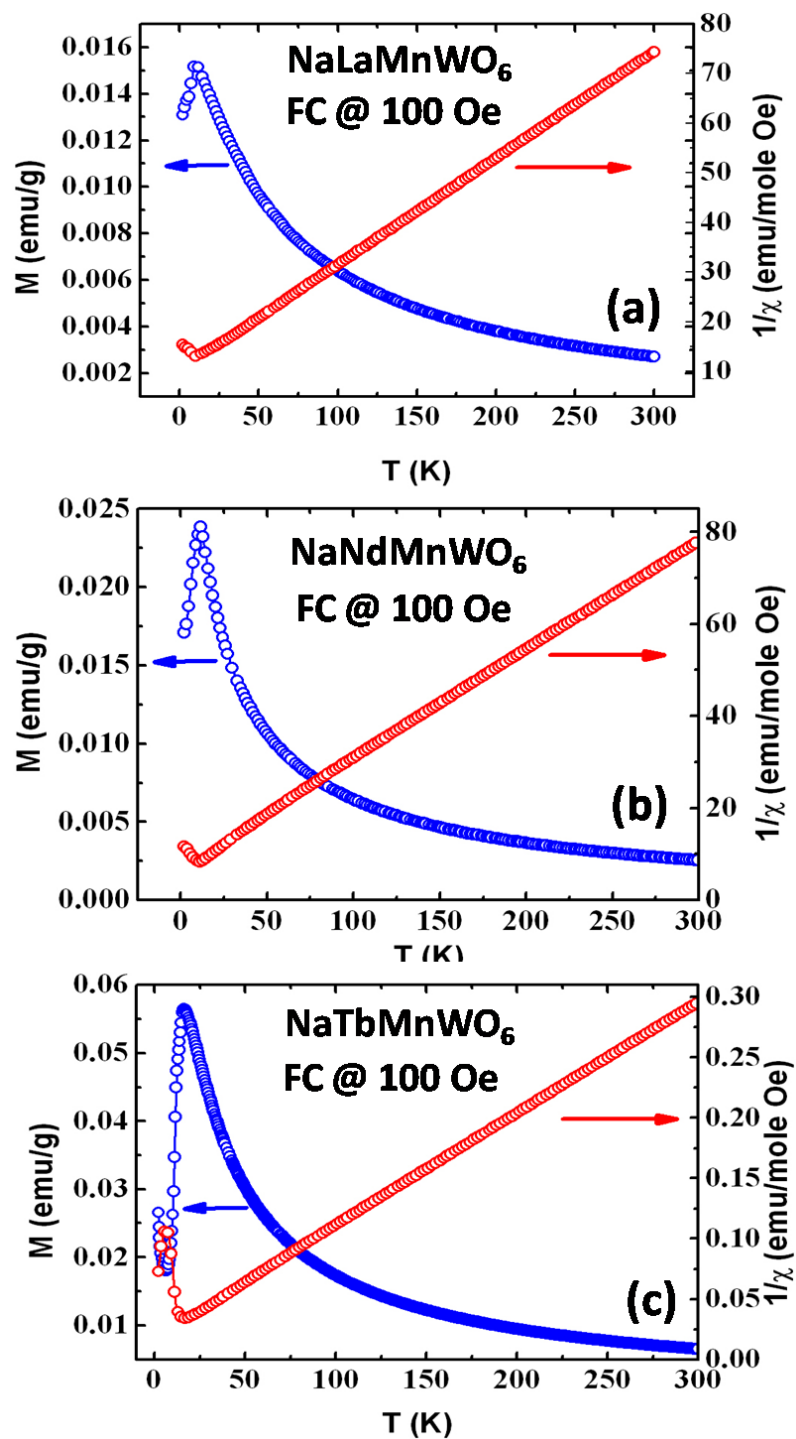| Compound name	Weiss constant	μ_{eff} (μ_B)	T_N (K)	t
$NaLaMnWO_6$	46.44	6.1	10	0.93
$NaNdMnWO_6$	28.17	5.8	11	0.91
$NaTbMnWO_6$	24.05	*	15	0.91

Figure 3.3 Magnetization *vs*. temperature (blue circle left axis) and $1/\chi_m$ *vs*. temperature plot (red circle right axis) of (a) $NaLaMnWO_6$ (b) $NaNdMnWO_6$ (c) $NaTbMnWO_6$.

3.3.3   Electrical properties

3.3.3.1 PUND and Hysteresis measurement

For the investigation of ferroelectric polarization at various temperatures in low temperature regime we have used single PUND [see chapter 2.4-2.9 for experimental details].

In the figure 3.4, conventional $P - E$ loop measured data at various temperatures (15 K, 77 K, 150 K, 300 K) with voltage pulse frequency 1000 Hz and 10 Hz for $NaLaMnWO_6$ where lossy loop is observed. This kind of loop is actually an indication of leaky material, i.e it has other polarization contribution such as resistive and capacitive rather than ferroelectric contribution (see chapter 2.7). In brief, when the extra contribution such as dielectric or resistive polarization dominates, the original ferroelectric polarization, if any, sometimes becomes invisible in the loop. So with this, it is confirmed that material may has little polarization or may not be ferroelectric in this case.

For further confirmation, we did PUND measurements. The detail of the experimental procedure is explained in chapter 2.7. However, in brief it may be mentioned here that the PUND is a good technique to observe the intrinsic ferroelectric polarization, especially, where the ferroelectric polarization is very less compared to the other source of polarization such as, leakage, capacitance and resistance. These extra sources of polarization will be more pronounced in the conventional ferroelectric loop measurement. In contrast, PUND uses two consecutive Positive and Negative pulses where the first pulse, for both polarity, gives the total polarization (including ferroelectric part) and the second pulse gives only other contributions of polarization (excluding ferroelectric part). By subtracting the polarization for the two consecutive positive or negative pulses, we can extract the intrinsic ferroelectric polarization [17].

Following this measurement procedures for $NaLaMnWO_6$, we observed only a flat, almost zero polarization even up to high applied electric field (190 kV/cm) for both at 1000 Hz and 10 Hz frequencies fig. 3.4. These results indicate that $NaLaMnWO_6$ is not a ferroelectric.

Figure 3.4 P-E loop (upper panels for 1000 Hz, 10 Hz) and PUND result (lower panels for 1000 Hz, 10 Hz) for $NaLaMnWO_6$. Different colors show temperature dependent measured data.

Results of PUND were further analyzed by time-dependent current curve (see Chapter 2.7). Figure 3.5 shows and electric fields and its response pulses at each temperature. For this material to be ferroelectric, we should observe a peak in response to the first negative pulse. But we see that only paraelectric components are dominant in the 1st and 2nd response pulses. The peak-like feature from FE component is absent from the 1st response pulse at each temperatures. The results of positive and up electric fields are similar except for its polarity, hence they are not shown. Hence, the time-dependent current curves also support for the evidence of non ferroelectricity in the sample $NaLaMnWO_6$ from 15 K to 300 K temperature.

Figure 3.5 Time-dependent current curves for NaLaMnWO$_6$. Left colum shows first negative and Right column shows second negative pulses and its responses. Different colors show temperature dependent measured data.
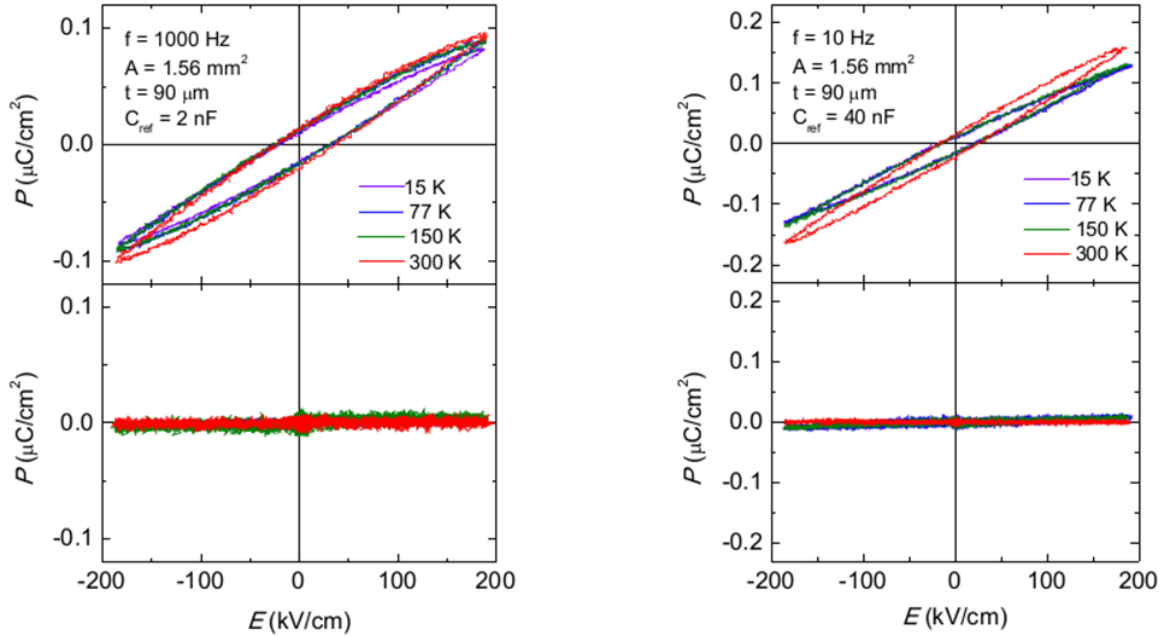

Figure 3.6 P-E loop (upper panels for 1000 Hz, 10 Hz) and PUND result (lower panels for 1000 Hz, 10 Hz) for NaNdMnWO$_6$. Different colors show temperature dependent measured data.
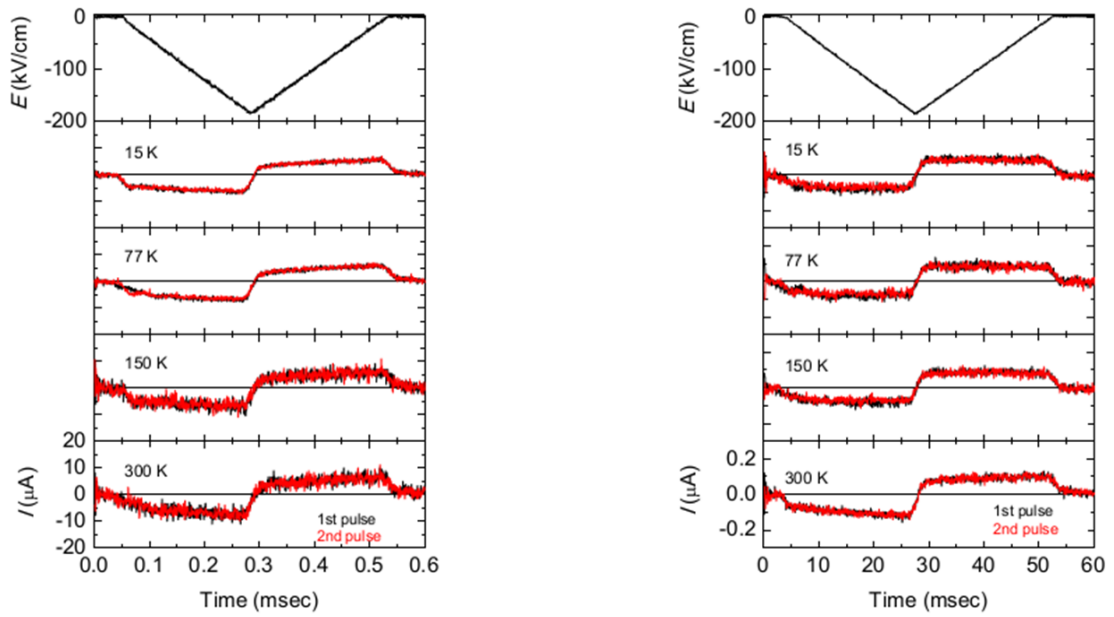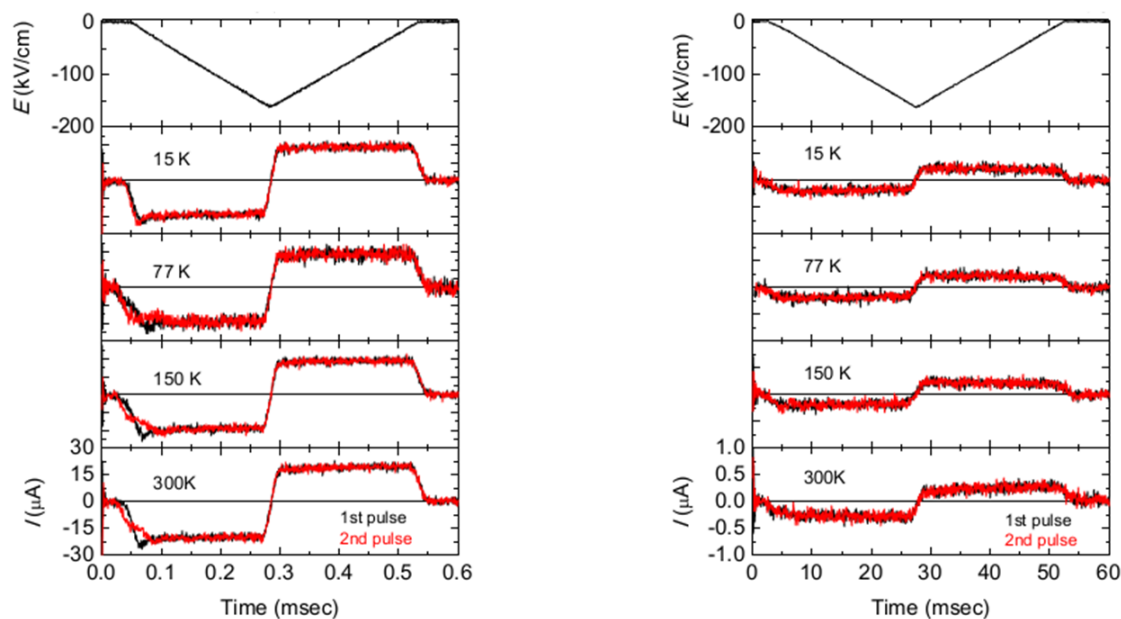
Figure 3.7   Time-dependent current curves for NaNdMnWO$_6$. Left colum shows first negative and Right column shows second negative pulses and its responses. Different colors show temperature dependent measured data.
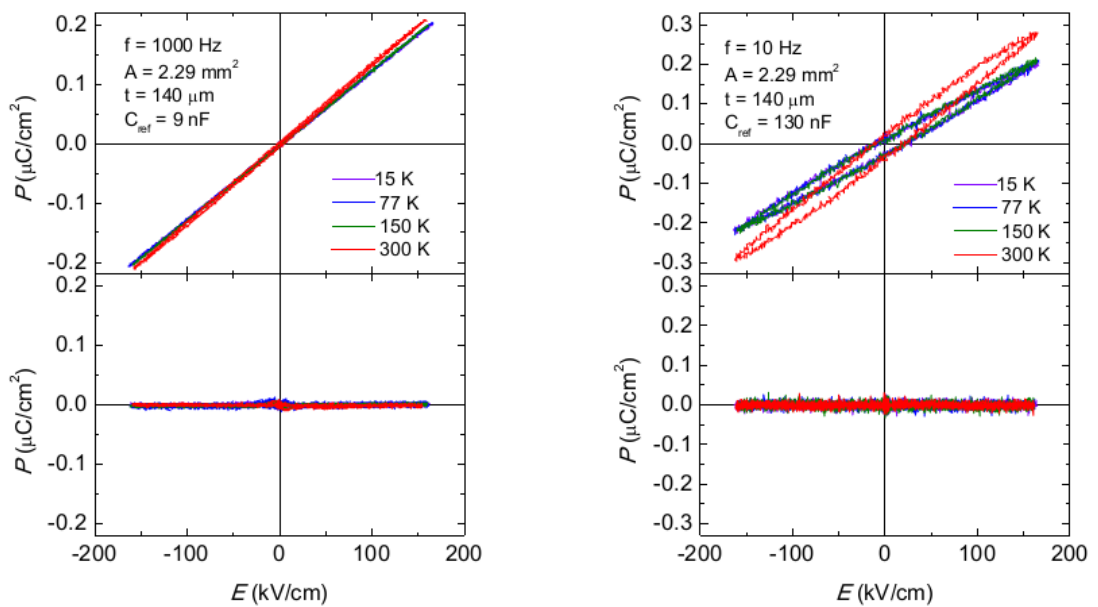
Similar measurements were also made for the compound; NaNdMnWO$_6$ that also do not exhibit ferroelectric nature as shown in fig.3.6 for conventional P-E loop as well as PUND measurement. The current curves with time are shown in fig. 3.7 which were interpreted on similar lines discussed above.

These investigations clearly suggest that these materials are not ferroelectric. In order to explore the symmetry related properties, we have carried out piezoelectric and Second SHG measurements [11, 12]. Surprisingly, both the measurements did not show any evidence for non-centrosymmetric structure. In the SHG measurement data, we observed almost zero signal compared to KDP and urea. These results undoubtedly resolve that these materials do not possess non-centrosymmetric structure.

3.3.3.2 Dielectric constant and Pyroelectric measurements

To probe the other electrical properties of these newly discovered materials, we have measured dielectric constant as well as pyroelectric current in the low temperature regime (350 K to 10 K). We have observed a sharp anomaly in the dielectric constant for a broad range of frequency at just below the room temperature for all the compounds. Figure 3.8 shows such dielectric anomaly at $T \approx 274$ K for $NaTbMnWO_6$. Different colors represent the dielectric constant measured at different frequency. The dielectric constant peak intensity decreases with the increasing measurement frequency. The peak position is almost fixed for different measurement frequency which suggests that this anomaly do not correspond to any relaxation behavior. Similarly we have observed this anomaly in the dielectric loss measured data also at $T \approx 274$ K.

It is to be noted that there is a small change in the temperature of the dielectric anomaly as well as loss for different compounds. To understand the origin of this dielectric anomaly, we have carried out pyroelectric current measurements on $NaTbMnWO_6$. Here, the pyrocurrent was measured after a poling procedure with the both direction (+100 V and -100 V).
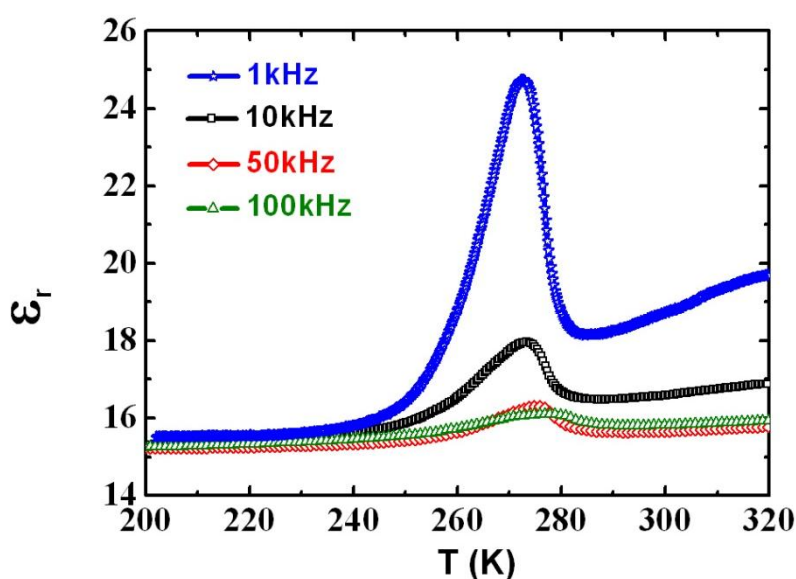
Fig 3.8 ε_r *vs.* T for $NaTbMnWO_6$ at different frequencies.
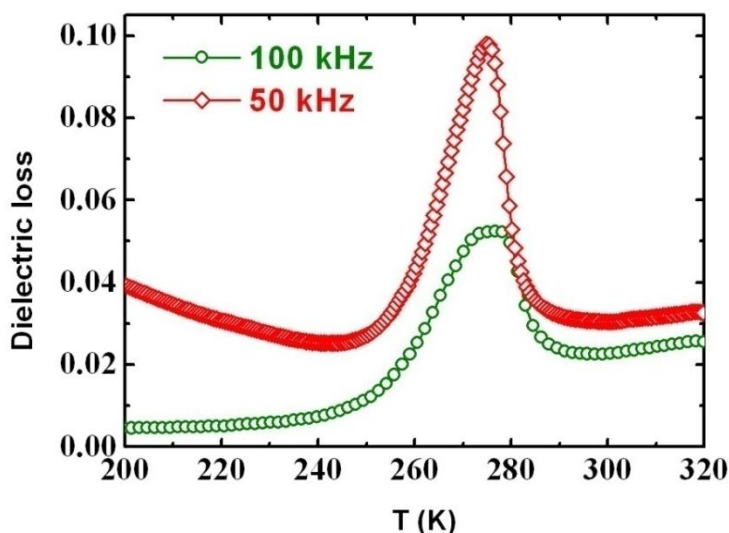
Fig 3.9 Variation of dielectric loss with temperature for NaTbMnWO$_6$ at different frequencies.

We observe that the pyrocurrent starts increasing above 240 K with a small peak around 280 K, where the dielectric constant shows a peak as shown in fig. 3.10 , nearly same temperature (T ≈ 278 K), where dielectric constant was observed (T ≈ 274 K). Because of huge back ground current, we observed the peak with less intensity. It should be mentioned that in addition to the pyrocurrent peak we also observe peak in the leakage current measurement which is unusual.
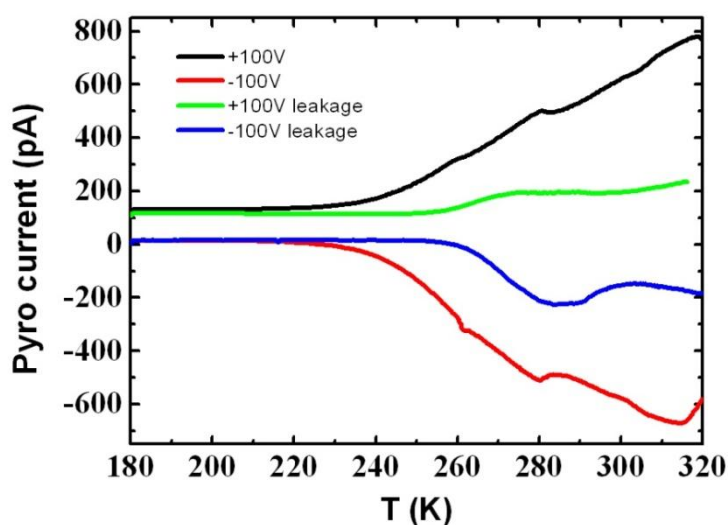
Fig. 3.10 Pyrocurrent measured data of NaTbMnWO$_6$. Black and red shows the pyrocurrent after poling and blue and green shows the leakage current.

Similarly, the pyrocurrent peak is observed for all the three compounds with a little difference in the temperature. We have shown the results of pyrocurrent peak for NaNdMnWO$_6$ in fig.3.11, where pyrocurrent was measured after poling with both the positive (+100 V) and negative (-100 V) voltages.
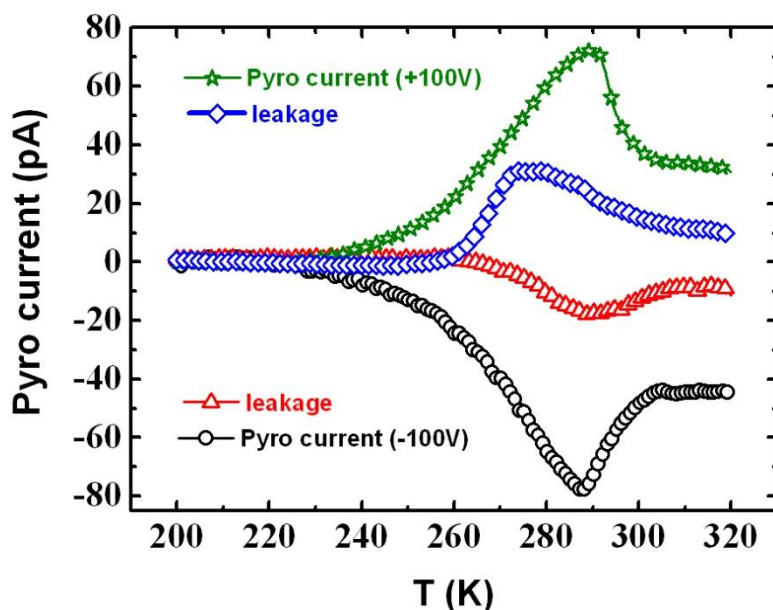
Figure 3.11   Reversal of pyrocurrent peak for NaNdMnWO$_6$ confirming bipolar nature. Presence of pyrocurrent peak in the leakage current.
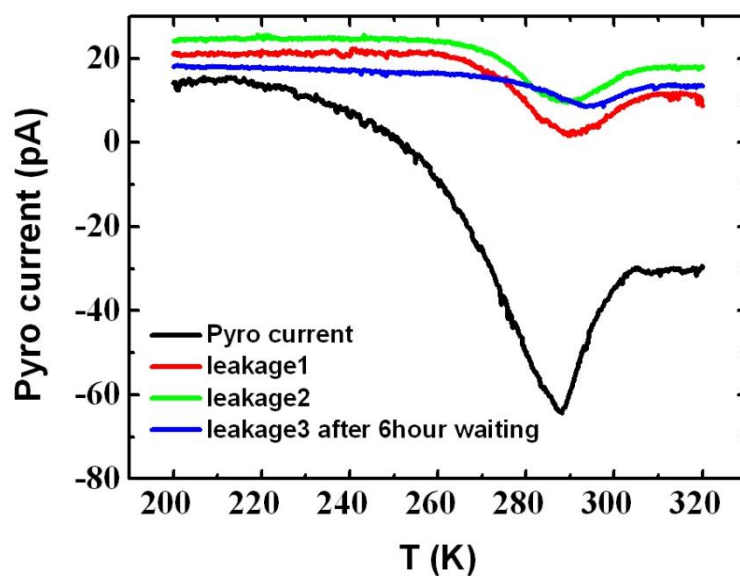
Figure 3.12 Pyrocurrent peak with different waiting time after poling with (-100 V)

We observe the peak at 280 K for this sample. Again, the peak was observed while measuring the leakage current as shown in fig.3.11.

For further investigation of this unusual leakage current peak in the leakage, we have carried out a leakage current measurement as shown in the fig. 3.12 for the $NaNdMnWO_6$ with different waiting time after poling, which shows the decay of the pyrocurrent with less intense pyrocurrent peak. We have measured the pyrocurrent without poling which also showed the pyrocurrent peak at the same temperature, as shown after poling, although the intensity was very less. The peak intensity was quite high when it was measured after poling procedure.

Clearly the anomalies in dielectric constant (also dielectric loss) and pyrocurrent are not related to ferroelectric polarization but seem to indicate some structural changes at ≈ 274 K for $NaTbMnO_6$. However, for better physical insights further investigations are necessary.

3.4   Conclusion

In conclusion, we did not observe any ferroelectric polarization from normal hysteresis loop as well as PUND measurement at various temperatures between 300 K and 15K. SHG and piezoelectric measurements also confirmed the absence of non-centrosymmetric crystal structure. Based on our experiments we conclude that the materials, $NaRMnWO_6$ (R=La, Nd and Tb) do not exhibit ferroelectric polarization and may not possess non-centrosymmetric crystal structure. A strong anomaly in dielectric constant as well as in pyrocurrent data near room temperature indicates a possible structural change.

3.5   Bibliography

1.   J. Wang, et al., *Science* **299**, 1719 (2003).

2.   T. Kimura, S. Kawamoto, I. Yamada, M. Azuma, M. Takano, and Y. Tokura, *Phys. Rev.* B **67**, 180401 (R) (2003).

3.   Graham King, Andrew S. Wills and Pattrick M. Woodward. *Phys. Rev. B* **79**, 224428, (2009).

4.   M.C. Knapp, P.M. Woodward. *J. Solid State Chem.* **179**, 1076, (2006).

5.   G. King, S. Thimmaiah, A. Dwivedi, P.M. Woodward. *Chem. Mater.* **19,** 6451, (2007).

6.   S. Garcia-Martin, E. Urones-Garrote, M.C. Knapp, G. King, P.M. Woodward. *J. Am. Chem. Soc.* **130,** 15028, (2008).

7.   T. Fukushima, A. Stroppa, S. Picozzi and J. M. Perez-Mato. *Phys. Chem. Chem. Phys.*, **13**, 12186, (2011).

8.   Jingshan Hou, Xin Yin, Fuqiang Huang, Weizhong Jiang. *Materials Research Bulletin*. **47**, 1295, (2012).

9.   Susana Garc í a-Mart í n,Graham King, Gwilherm Nénert, C. Ritter, and Patrick M. Woodward. *Inorg. Chem.* **51**, 4007, (2012).

10.   Graham King, Lora M. Wayman, Patrick M. Woodward. *Journal of Solid State Chemistry*. **182,** 1319, (2009).

11.   Fukunaga M and Noda Y. *J. Phys. Soc. Japan.* **77**, 064706, (2008).

12.   Scott J F, Kammerdiner L, Parris M, Traynor S, Ottenbacher V, Shawabkeh A and Oliver W F. *J. Appl.Phys*. 64787, (1988).

13.   Kang Min OK, Eun Ok Chi and P. Shiv Halasyamani. *Chem. Soc. Rev.* **35**, 710, (2006).

14.   D. N. Astrov, Sov. *Phys. JETP*. **11**, 708, (1960).

15.   E. Asher, H. Rieder, H. Schmid, and H. Stossel, *J. Appl. Phys.* **37**, 1404, (1966).

16.   Goldschmidt, Victor M. *Die Naturwissenschaften.* **21,** 477, (1926).

17.   The measurement, instrumentation, and sensors handbook. 32–113.

Chapter 4

Multiferroicity in disordered orthorhombic perovskite oxides SmM$_{0.5}$M$'_{0.5}$O$_3$, Where M, M$'$ = Fe, Cr and Mn (M ≠ M$'$)

4.1 Introduction

The recent discovery of spin-driven ferroelectricity and giant magnetoelectric effect has created remarkable interest in the emerging field of multiferroic research from both scientific and technological point of view [1-5]. *Multiferroics* and *magnetoelectrics* have been studied for more than four decades. A *magnetoelectric multiferroic* can be defined as a material where, magnetization can be altered by electric field and vice versa [25]. In most of the multiferroics, the difference in temperature scale between ferroelectric ordering and magnetic ordering is significantly vast and the origin of these two properties are independent, which leads to a very weak coupling between them. But, from the technological point of view, e.g. development of low power consuming 'spintronics', where external electric field controls the ferromagnetism, strongly coupled cross-linked responses are required. This problem was addressed after the discovery of a new class of multiferroics, showing a large magnetoelectric effect in orthorhombically distorted perovskites Tb(Dy)MnO$_3$. The low temperature magnetic

ordering, however, limits the use of these materials in the fabrication of devices. There has been a lot of effort to achieve an efficient mutual control of electricity and magnetism at higher temperature to address the problem. In spite of such focused effort in finding out candidate materials which show stronger coupling at workable temperature, there are not many materials known till today which can be used as a magnetoelectric multiferroic in practical device applications [1].

In Tb(Dy)MnO$_3$, the ferroelectricity originates from a cycloidal or spiral spin structure [1]. This spiral ordering is observed only in smaller size of rare-earth manganites (Tb, Dy, Gd) below 27 K where the nearest neighbor exchange interaction is ferromagnetic and next nearest neighbor interaction is antiferromagnetic, in the *ab* plane. In particular this two opposing magnetic interactions frustrates the magnetic ordering in the *ab* plane and a spiral spin ordering appears. Spiral spin breaks the spatial inversion symmetry that eventually results in spontaneous electrical polarization. The microscopic origin can be explained by inverse DM interaction and the net polarization can be given by following expression.

$$\boldsymbol{P} = a \sum_{<i,j>} \boldsymbol{e_{ij}} \times (\boldsymbol{S_i} \times \boldsymbol{S_j})$$

Where $\boldsymbol{S_i}$ and $\boldsymbol{S_j}$ are two neighboring spin vectors, '*a*' is the spin orbit coupling constant and $\boldsymbol{e_{ij}}$ is the spin chain wave vector. So, for efficient polarization, a high spin orbit coupling (a) is required.

But, the ground state of higher rare-earth size (La-Eu) manganites is only paraelectric and A-type antiferromagnetic. It is to be noted that in this case the next nearest neighbor AFM interaction is not strong enough to induce frustration in the *ab* plane. Basically, smaller size rare-earth cations give smaller Mn-O-Mn bond angle which in turn make the next nearest neighbor interactions stronger [18].

On the contrary, $SmMnO_3$ has not evoked much interest, primarily due to the perceived absence of ferroelectricity, although it possesses the same structure like $TbMnO_3$. Furthermore, $SmMnO_3$ has a distinct feature of temperature induced magnetization reversal, where magnetization varies from positive to negative values through zero magnetization at compensation temperature (T*). This phenomenon is usually observed in Néel's N type antiferromagnetic compounds where the two different magnetic sublattice moments cancels each other because of different temperature dependence of the constituent sublattices [18]. Most interestingly, $SmMnO_3$ shows a large magnetocapacitive effect at around T* [9].

There has been a recent study of ferroelectricity on isostructural RE orthochromites ($RCrO_3$), which also have been shown to exhibit fairly large polarization 0.2 to 0.8 $\mu C/cm^2$, below T_N of Cr^{+3} but only when the RE ion is magnetic. It has been suggested that the ferroelectricity arises because of combined effect of 3d - 4f exchange interaction of Cr^{+3} ions and R^{+3} ions triggered by an applied poling electric field. Remarkably, $SmFeO_3$, which was perceived to be non ferroelectric earlier, has been shown to be ferroelectric at room temperature with very small polarization [4]. It was proposed that the combined effect of canted AFM ordering and the two non equivalent spin pairs were driving the ferroelectric polarization [12]. The most striking thing is that the T_N of Fe^{+3} is well above room temperature (670 K). The ever increasing interest on $RFeO_3$ and isostructural $RCrO_3$ and $RMnO_3$ is rekindled after the report on $SmFeO_3$, as it meets both the major challenging demands in multiferroic family, cross coupling of electric and magnetic order parameters and the enhanced temperature scale for practical applications. But the polarization value is of lesser magnitude.

On summary, $SmFeO_3$ has higher T_N but less polarization. On the other hand, $SmCrO_3$ has T_N below T_{RT} (room temperature), but the polarization is fairly high compared to

the $SmFeO_3$. Based on the RE size in $RMnO_3$, Mn^{+3} ions have a distinct property of non-collinear spiral ordering or frustrated magnetism and canted weak ferromagnetism (WFM) at low temperature. The ionic radii of Mn^{+3}, Cr^{+3} and Fe^{+3} ions are very similar [5] and all compounds [$SmMO_3$ (M=Mn, Cr Fe)] are crystallized in P*bnm* space group [21,7,6]. In order to explore this magnetically induced ferroelectricity, in these materials, with the knowledge that the $T_N > T_{RT}$ and high ferroelectric polarization, a systematic study of disordered RE perovskite oxides ($SmMn_{0.5}Cr_{0.5}O_3$, $SmFe_{0.5}Cr_{0.5}$ and $SmFe_{0.5}Mn_{0.5}O_3$) is performed and explored here.

4.2. Experimental section

4.2.1. Synthesis

The polycrystalline $SmMn_{0.5}Cr_{0.5}O_3$, $SmFe_{0.5}Cr_{0.5}O_3$ and $SmFe_{0.5}Mn_{0.5}O_3$ compounds were made by conventional solid state route. Sm_2O_3 and Fe_2O_3 were preheated at 1000 ^oC for 12 hours in air. Then stoichiometric quantities of Sm_2O_3, Mn_2O_3, Cr_2O_3 and Fe_2O_3 were taken in an agate mortar pestle and thoroughly mixed. Mixtures were then heated at 1100, 1200, 1300 ^oC sequentially with intermittent regrinding. Finally the powder was pressed into pellets and sintered at 1400 ^oC for 15 hours. $SmMn_{0.5}Cr_{0.5}O_3$ and $SmFe_{0.5}Mn_{0.5}O_3$ compounds were heated in pure Argon atmosphere to avoid Mn^{+4} ionic states. Mn^{+4} decrease the resistivity, thereby increasing the leakage current during the electrical measurement. If the leakage current contribution is more, then it is extremely difficult to quantify the intrinsic polarization. To avoid this, argon was purified by passing through hot (800 ^oC) copper turnings. It is to be noted that $SmFe_{0.5}Cr_{0.5}O_3$ was heated in air only.

4.2.2   Characterization

Powder X-ray patterns were taken by Bruker-D8 Advance Diffractometer (30mA current at 1.54 Å wavelength) over a 2θ range 10° to 80° at room temperature. Phase purity was checked from X-ray diffraction pattern and Rietveld pattern matching was carried to find the lattice parameters.

4.2.3.   Magnetic measurements

Magnetic measurements were done in Squid VSM (Quantum Design, USA). Temperature dependent FC magnetization recorded at 100 Oe in the temperature range of 2 K to 390 K. M *vs.* H data was recorded at 2 K.

4.2.4   Electrical measurement

For electrical measurement silver paint was used to make the electrode on the polycrystalline well sintered samples. Dielectric properties were measured in Agilent E4980A LCR meter and pyrocurrent was recorded by Keithley 6517A electrometer. Both the measurements were carried out using the multifunctional probe using the Physical Properties Measurement System (PPMS, Quantum Design). Positve Up Negetive Down (PUND) / Double Wave Method (DWM) measurements were done in Precission Workstation Ferroelectric tester of Radiant Technology. For DWM the custom made voltage profiles were made from Microsoft office Excel [For details see chapter 2].

4.3   Results and discussions

4.3.1   Structure

Rare earth ortho-chromites ($SmCrO_3$) and ortho-ferrites ($SmFeO_3$) are known to crystallize in $GdFeO_3$ type orthorhombic structure. All three $SmCrO_3$, $SmFeO_3$ and $SmMnO_3$ possess centrosymmetric P*nma* crystallographic space group. The ionic radii of Mn^{+3}, Fe^{+3} and Cr^{+3} are 0.645 Å, 0.645 Å and 0.615 Å, respectively, shows no marked difference. $SmCrO_3$, $SmFeO_3$ and $SmMnO_3$ can form a complete solid solution with same crystal structure. The all three synthesized compounds are found to be crystallized in centrosymmetric P*nma* space group. All the calculated lattice parameters are listed in table 4.1.

Figure 4.1   Rietveld refinement on the X-ray pattern of $SmFe_{0.5}Cr_{0.5}O_3$. Red circles, black line, blue line and green vertical lines are representing observed pattern, calculated pattern, difference, Bragg's positions of the peaks, respectively.

Figure 4.1, shows X-ray diffraction pattern at room temperature along with Rietveld refinement data of $SmFe_{0.5}Cr_{0.5}O_3$ compound. Pattern matching shows that the

compound does not have any impurity. Similarly, in Fig 4.2 $SmMn_{0.5}Cr_{0.5}O_3$ X-ray pattern and Rietveld refined data has been shown. We see the refined data fits well with the observed data, showing no impurity peak except some intensity mismatch between recorded pattern and calculated pattern which could be due to preferred orientation. Although, refinement give rise a little higher $\chi 2$ (goodness of fit) value but, the lattice parameters are very similar to the $SmFe_{0.5}Cr_{0.5}O_3$, as expected due to the fact of similar ionic radii of the Fe^{+3} and Mn^{+3} [5]. For $SmFe_{0.5}Mn_{0.5}O_3$, the Rietveld refined data and X-ray pattern is shown in the Fig 4.3.

Figure 4.2   Refinement on the X-ray pattern of $SmMn_{0.5}Cr_{0.5}O_3$. Red circles, black line, blue line and green vertical lines are representing observed pattern, calculated pattern, difference, Bragg's positions of the peaks respectively.
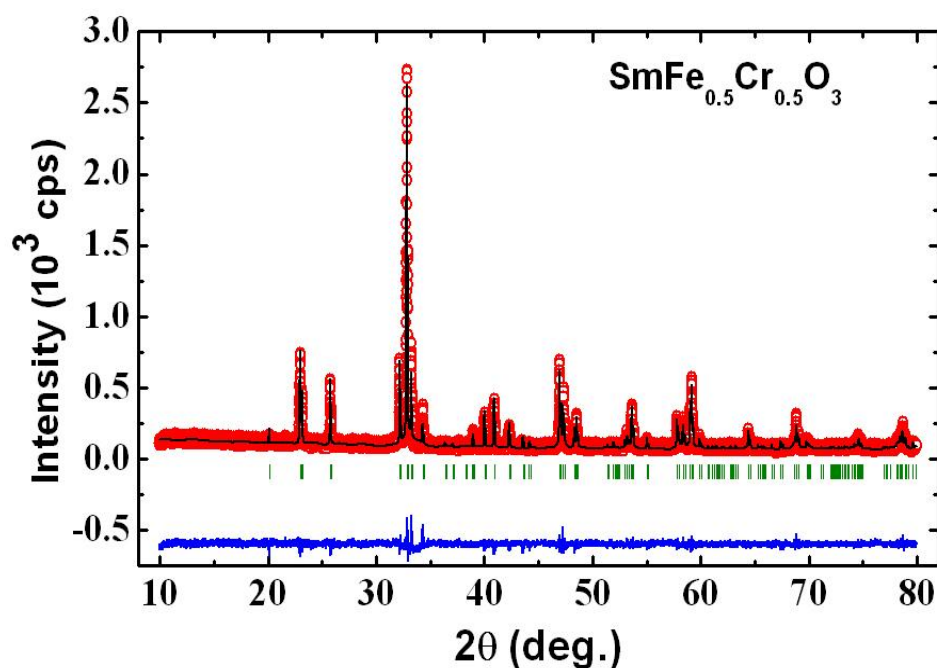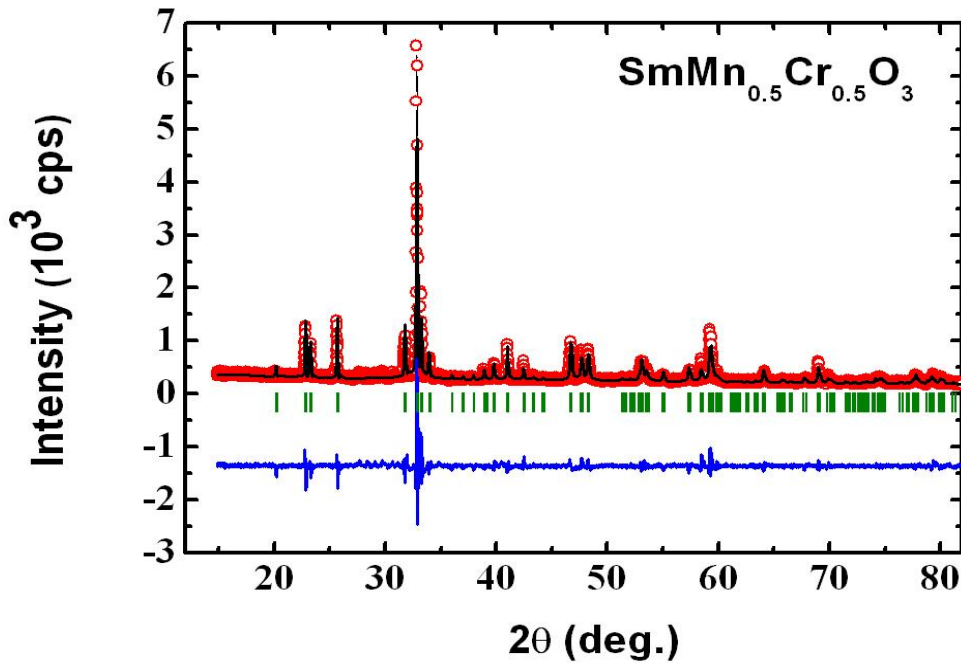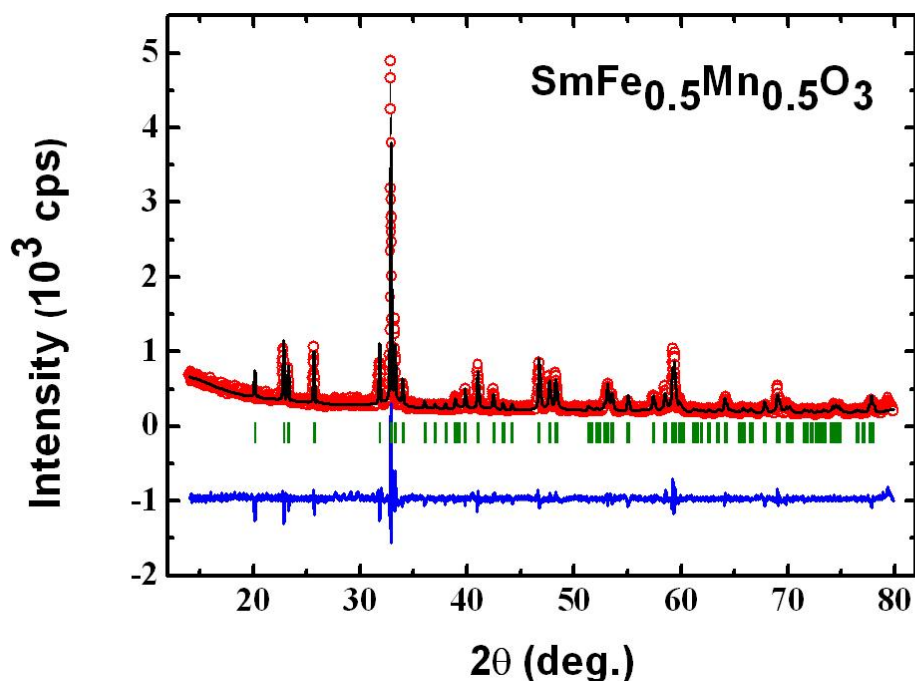
Figure 4.3 Reitveld refinements on the X-ray pattern of $SmFe_{0.5}Mn_{0.5}O_3$. Red circles, black line, blue line and green vertical lines are representing observed pattern, calculated pattern, difference, Bragg's positions of the peaks respectively.

A little mismatch between the recorded and calculated intensity is observed which give rise a little higher $\chi 2$ value for this compound also. The mismatch in intensity was observed in the Mn substitute compound only. So the reason could also be the multivalent state of Mn^{+3}. Table 4.1 contains all three synthesized and parent ($SmMO_3$; M= Mn, Cr and Fe) compound's lattice parameter for comparison [21, 7, 6]. We notice that the lattice parameter and cell volume are very similar to their parent compound lattice parameters and also consistent with the ionic size of the Fe^{+3}, Mn^{+3} and Cr^{+3}.

Table 4.1 Lattice parameters and unit cell volume: (all compounds have P*nma* space group).

Compound formula	a (Å)	b (Å)	c (Å)	Unit cell volume ($Å^3$)
$SmFe_{0.5}Cr_{0.5}O_3$	5.3850(1)	5.5532(1)	7.6806(1)	229.696(7)
$SmFe_{0.5}Mn_{0.5}O_3$	5.3801(0)	5.6165(0)	7.6224(0)	230.332(0)
$SmMn_{0.5}Cr_{0.5}O_3$	5.3802(0)	5.6221(0)	7.6255(0)	230.662(0)
$SmFeO_3$	5.3784	5.5690	7.6944	230.47
$SmCrO_3$	5.369	5.494	7.684	225.68
$SmMnO_3$	5.358	5.825	7.483	233.55

4.3.2 Magnetic Properties

The FC magnetization *vs.* Temperature data of $SmFe_{0.5}Cr_{0.5}O_3$, $SmFe_{0.5}Mn_{0.5}O_3$, and $SmMn_{0.5}Cr_{0.5}O_3$ are shown in figure 4.4, 4.5 and 4.6, respectively. In FC measurement, the sample was cooled to low temperature from high temperature through its T_N (Néel temperature) in presence of a DC magnetic field of 100 Oe. The T_N, where the magnetic moment starts increasing from paramagnetic region, for all samples was identified and has been shown in the table 4.2. The temperature induced spin reorientation (T_{SR}) temperature was observed from the FC magnetization data. The spin directions sometimes may start moving from one crystallographic direction to some other crystallographic direction e.g. from the canted AFM to nearly collinear AFM below some temperature which is known as spin reorientation temperature (T_{SR}) [22, 23], similar to the Morin transition observed in hematite [8].

We see in fig 4.4 (a) that the $SmCrO_3$ has the AFM ordering temperature (T_N) at 197 K. This material shows spin reorientation at T ≈ 50 K, but the net moment does not go to negative value. Spin reorientation is relevant here because of interplay between Dzyaloshinsky-Moriya interaction and magnetic anisotropy. It is reported that $SmCrO_3$, orders in G- type AFM configurations, goes through three following magnetic structures as $\Gamma_1(A_x, G_y, C_z)$, $\Gamma_2(F_x, C_y, G_z)$ and $\Gamma_4(G_x, A_y, F_z)$ [Bertaut notation][20]. Γ_2 and Γ_4 structure allow spin canting while Γ_1 shows no spin canting. It shows the collinear magnetic structure Below ≈ 30 K. $SmMnO_3$ is reported to be A-type AFM [9]. From fig. 4.4(b), we see that the AFM ordering (T_N) is ≈ 60 K and below T_N, there is sharp fall in the magnetization which goes to negative value through compensation point (T*) ≈ 10 K. T* is temperature, where the magnetization becomes zero due to antiferromagnetically coupled two different magnetic sublattices. Here, Sm^{+3} and Mn^{+3} are antiferromagnetically coupled fig. 4.5 [19]. In the $SmMn_{0.5}Cr_{0.5}O_3$, there is a disordered arrangement of Mn^{+3} and Cr^{+3} in the B site of the ABO_3 perovskite. Mn^{+3}-Cr^{+3} interactions should be more pronounced than Mn^{+3}-Mn^{+3} and Cr^{+3}-Cr^{+3} interactions since the inherent extent of disorder is 1:1 for the ions.
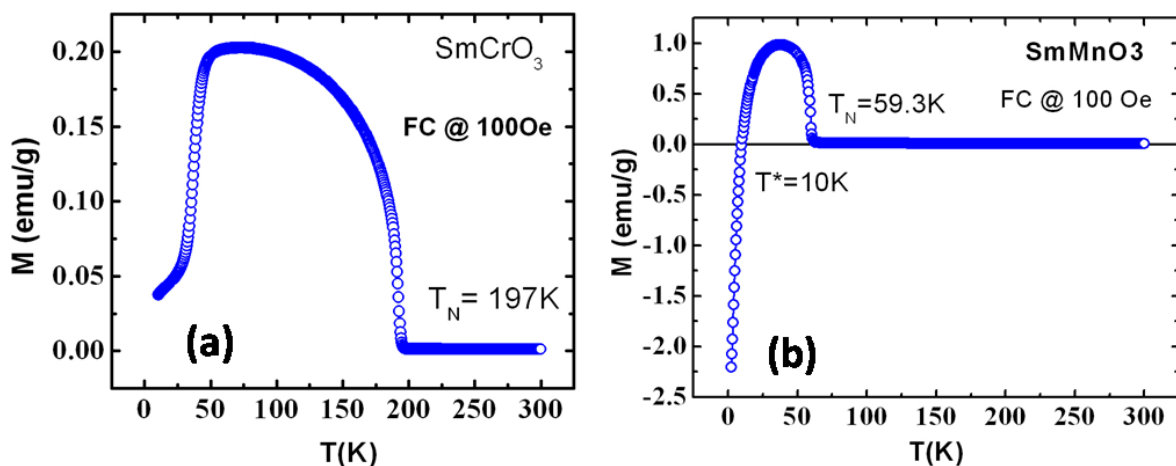

Figure 4.4   FC M *vs*. T data of (a) $SmCrO_3$ (b) $SmMnO_3$

The FC magnetization data of $SmMn_{0.5}Cr_{0.5}O_3$ is given in the fig. 4.5(b), shows the magnetic ordering temperature (T_N) at ≈ 100 K which lies in between the magnetic ordering of $SmMnO_3$ (≈ 60 K) and $SmCrO_3$ (≈ 197 K). We see a decreasing trend below ≈ 10 K, which can be due to the antiferromagnetically coupled Sm^{+3} and canted Mn^{+3} moments. But there is no spin reorientation at higher temperature, similar to that, observed in $SmCrO_3$. Further, there is no change, observed in the magnetization data at the individual ordering temperature of both the $SmMnO_3$ and $SmCrO_3$ compound. This indicates the combined effect of Mn^{+3} and Cr^{+3} ordering rather individual ordering of Mn^{+3} and Cr^{+3} ions. Therefore the magnetic ordering temperature increases from 60 K to 100 K. The occurrence of ferroelectricity, as a consequence of combined effect of both the disordered ions at this magnetic ordering temperature is quite interesting to look at. However, the nature of magnetic structure of this new compound is unknown where the parent compounds contain both the A-type and G-type magnetic ordering. It is also interesting to observe the total net canted AFM or WFM moment being increased to a larger extend value compared to both the parent compounds. Magnetic frustration would also increase which is desired for spiral magnetic ordering which is a major driving force for magnetically induced ferroelectric polarization.
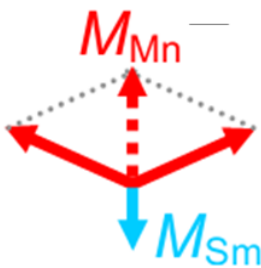
Fig. 4.5   Antiferromagnetic coupling between canted Mn^{+3} and Sm^{+3} magnetic moment.

The compound remains weak ferromagnetic state at low temperature as revealed by M *vs.* H data at 2 K (fig 4.7.b). Fig 4.7.b shows unsaturated loop even after applying 6 T field. It has been reported that $YFe_{0.5}Cr_{0.5}O_3$ and $YFe_{0.5}Mn_{0.5}O_3$ shows canted AFM ordering with WFM due to DM interaction while Cr^{+3} and Mn^{+3} ions shows single ion

magnetic anisotropy. The competition between DM interaction and Single Ion Anisotropy (SIA) gives rise to temperature induced magnetization reversal [10,11]. Figure 4.6.c shows the temperature dependence of magnetization of $SmFe_{0.5}Mn_{0.5}O_3$. This exhibits similar spin reorientation behavior around 300 K, as discussed above for the $SmCrO_3$. However the net moment does not go to negative values. A similar competition between SIA of Mn^{+3} and DM interaction of Fe^{+3} and Mn^{3+} exists in $SmFe_{0.5}Mn_{0.5}O_3$ which gives rise to canted AFM moment. However, there is also an induced moment on the rare-earth ion making the qualitative understanding of the phenomenon quite complicated and unique. It is necessary to note that in $SmMn_{0.5}Cr_{0.5}O_3$, a high value of canted moment may arise as a consequence of both Mn^{+3} and Cr^{+3} ions, and their corresponding SIA. It is proposed that the magnetization reversal is a common phenomenon in distorted perovskites where mixed magnetic ions of different anisotropies are present.

From fig 4.6.a, it is observed that $SmFe_{0.5}Cr_{0.5}O_3$ does not show magnetization reversal although there are two different magnetic ions (Mn^{+3} and Fe^{+3}). Furthermore, we see a very low magnetic moment value for $SmFe_{0.5}Mn_{0.5}O_3$ compound compared to $SmMn_{0.5}Cr_{0.5}O_3$ which also confirms the competition between the canted Fe^{+3} and Mn^{+3} moments.
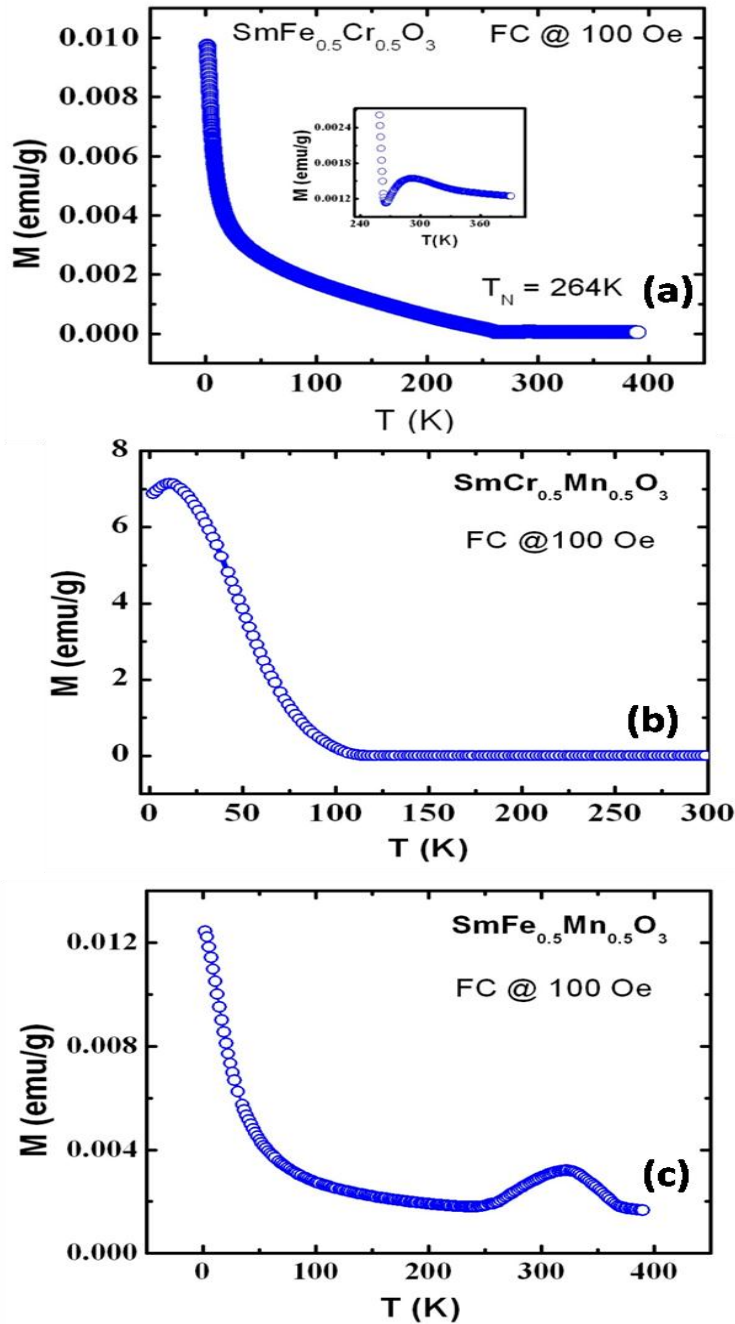
Figure 4.6   Field cooled (100 Oe) M *vs.* T data of (a) $SmFe_{0.5}Cr_{0.5}O_3$ (b) $SmMn_{0.5}Cr_{0.5}O_3$ (c) $SmFe_{0.5}Mn_{0.5}O_3$.

The net moment effectively becomes very less and is accounted to be due to Sm^{+3} (induced by 3d magnetic moment) ion and net canted Fe^{+3} and Mn^{+3} moments. In the recent study on ferroelectricity of RE orthochromites, it has been shown that the ferroelectricity arises because of the interplay of moments of the 3d transition metal ion

and RE 4f magnetism, which also leads the rare-earth to be ordered at lower temperature.

Figure 4.7 M *vs.* H data at 2 K of (a) $SmFe_{0.5}Cr_{0.5}O_3$ (b) $SmMn_{0.5}Cr_{0.5}O_3$ (c) $SmFe_{0.5}Mn_{0.5}O_3$.

From fig 4.7(c), we see a tiny hysteresis area at 2K which again can be accounted to the small Sm^{+3} moment. In $SmFe_{0.5}Cr_{0.5}O_3$, the intera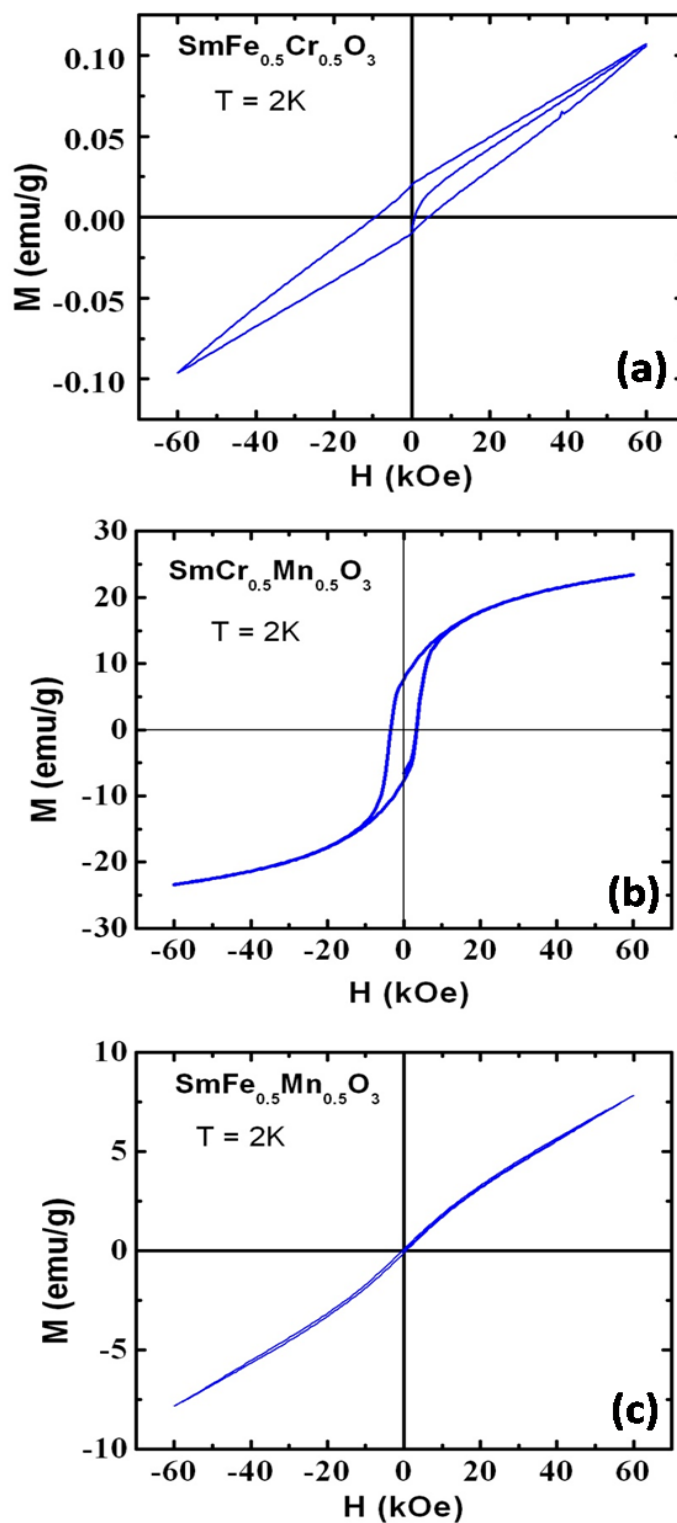ction is more between Fe^{+3} and Cr^{+3} compared to $Fe^{+3} - Fe^{+3}$ and $Mn^{+3} - Mn^{+3}$ as there is 1:1 disorder. The T_N for $SmFeO_3$ is 670 K [12] and for $SmCrO_3$ it is 197 K. From the fig. 4.6(c) we notice that the T_N is around 264 K for $SmFe_{0.5}Cr_{0.5}O_3$. Below T_N, the magnetization increases monotonously, exhibiting the canted AFM moment. This canting is further confirmed by the occurrence of hysteresis loop without saturation in the M $vs.$ H measured data at 2 K as shown in fig. 4.7.a. At low temperature, below 50 K, the moment increases rapidly because of the induced moment on the rare-earth (4f) ion due to the 3d magnetic moments of the transition metal ions. This compound combines two mechanisms, one is the antisymmetric DM interactions of the disordered spins of Fe^{3+} and Mn^{+3} competing each other and the other is the induced moment on the RE ion by the transition metal ion. In the succeeding discussion, the interesting ferroelectric properties induced by different magnetic aspects are elucidated.

Table 4.2 List of T_N and T_{SR} for parent compounds and synthesized compound.

Compound name	T_N (K)	T_{SR} (K)
SmMnO3	60 K	--
SmCrO3	197 K	50 K
SmFeO3	670 K	--
$SmFe_{0.5}Cr_{0.5}O_3$	264 K	--
$SmMn_{0.5}Cr_{0.5}O_3$	100 K	--
$SmFe_{0.5}Mn_{0.5}O_3$	370 K	350 K

4.3.3 Ferroelectric properties

The objective of this chapter was to probe the ferroelectric properties in the presence and in absence of external magnetic field. The major challenging problem in this kind of polycrystalline material is the determination of intrinsic polarization, as leakage contribution is quite large and the ferroelectric polarization is smaller. For example, a challenging issue to ascertain whether, in the E-type antiferromagnetic spin arrangement, (e.g $HoMnO_3$) large ferroelectric polarization exists or not [24]. This issue is closely related to the intriguing experimental difficulty in determining the polarization of polycrystalline sample. The most conventional method for the measurement of ferroelectric polarization is the pyroelectric current measurement. The pyroelectric current measurements are done after poling process through the magnetic ordering temperature under high dc electric fields which may cause large leakage current, generation of space charge due to poor sample quality, porosity, oxygen deficiency, etc, in a polycrystalline sample. It results in incomplete electric poling and space charge effects also [14]. The space charge or surface charges can be trapped in the grain boundary of polycrystal or the ferroelectric domain boundary during the electrical poling procedure. The space charge can be trapped above the transition temperature or below the transition temperature and can be a source of erroneous charges, which will interfere with intrinsic pyroelectric current. Hence the pyroelectric current measurements are subject to significant errors. If these undermining effects are dominant, then it could be difficult sometimes to get well defined pyroelectric peak itself.

An alternative method is a direct measurement of the P–E hysteresis loop using the Sawyer–Tower circuit [15]. However, even this method is also unreliable when

relatively large leakage currents exists which result a distorted, unsaturated hysteresis curves for smaller values of ferroelectric polarization [24]. A recent significant development of a new technique to measure intrinsic polarization irrespective of space charge, leakage, or grain boundary effect is termed as Positive-Up and Negative-Down (PUND) which is also called as Double Wave Method (DWM) [16].

4.3.3.1   Pyrocurrent measurement

For pyroelectric measurement, initially we have poled the $SmMn_{0.5}Cr_{0.5}O_3$ from 260 K to 10 K, with an applied electric field of +1.33 kV/cm. After poling the sample was shorted for 5 h at 10 K for minimizing the leakage current. Pyrocurrent was then measured while warming up from 10 K to 260 K. This procedure was followed for - 1.33 kV/cm field also. The above mentioned measurement was done in presence of 0 T, 2 T and 3 T magnetic fields. The pyrocurrent was integrated upon time to obtain the charge, which was finally divided by the area of the sample to get the polarization. It is interesting to note that the ferroelectric polarization is observed in presence of magnetic field, whereas there was no indication of polarization arising in absence of magnetic field. Figure 4.8 shows ferroelectric polarization of $SmMn_{0.5}Cr_{0.5}O_3$ and pyroelectric current peaks (inset) obtained from pyroelectric measurements in presence of magnetic field 3T. The switching of polarization occurs when the sample was poled with negative field as shown in the fig. 4.8. The calculated polarization value is around 0.012 $\mu C/cm^2$ for an applied 1.33 kV/cm poling field, where the leakage current was corrected in the measured pyroelectric current. The figure shows that the ferroelectric polarization arises in the vicinity of 150 K. This result demonstrates the development of the spontaneous polarization well above the T_N (100 K) (fig 4.6.b) of the measured

sample. It is to be noted that there was no visible change in magnetization as well as dielectric anomaly observed at 150 K.
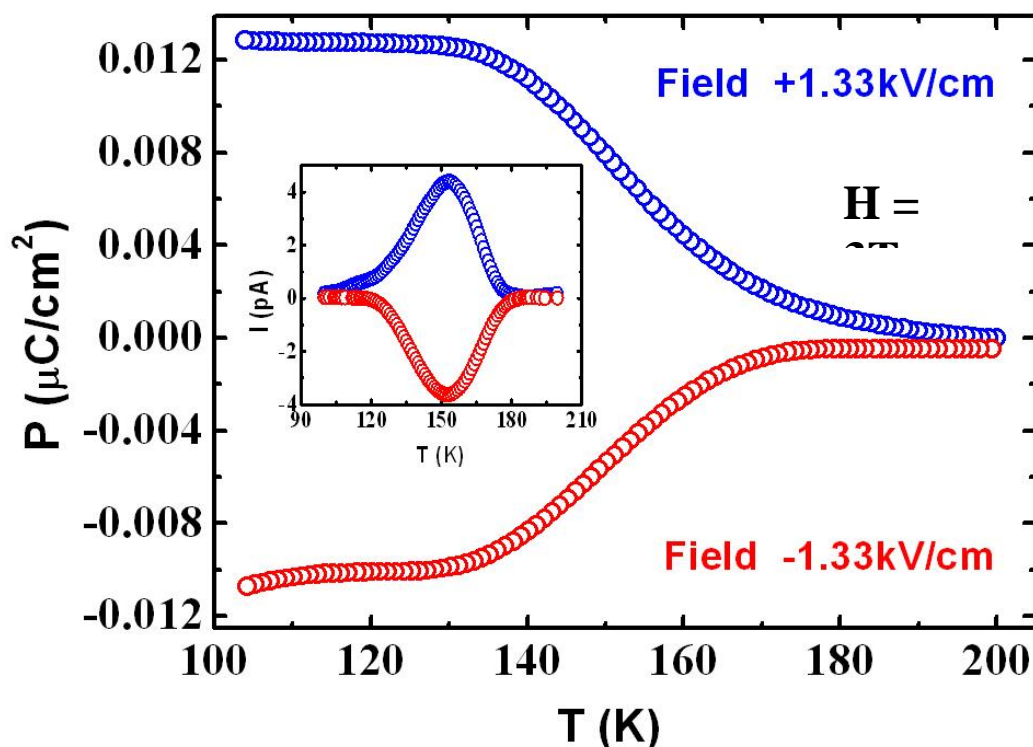

Figure 4.8 Integrated ferroelectric polarization of $SmMn_{0.5}Cr_{0.5}O_3$. Inset shows the measured pyroelectric current. Blue circles, and red circles represent the polarization for positive and negative poling field respectively.

The ferroelectric polarization is observed at the 150 K for applied 2 T magnetic field also. However, a marked change of polarization value is not observed. It is quite strange that the ferroelectric polarization arises only in presence of magnetic field at around 150 K, wherein it was expected to arise around 100 K i.e at the magnetic ordering temperature, driving factor. It is obvious that the magnetic ordering of Mn^{+3} or Cr^{+3} is not inducing the moment to Sm^{+3} which would result in ferroelectric polarization like $SmCrO_3$ or $SmFeO_3$, where Sm^{+3} gets displaced because of Cr^{+3} or Fe^{+3} moment respectively [13].

4.3.3.2 Ferroelectricity measurement by DWM technique

For the measurement technique see chapter 2.7. Fig. 4.9 shows the voltage profile of the triangular pulse (f = 0.5 Hz, V_{max} = 200 V), for the polarization measurement at 2 T magnetic field, applied on the sample. Initial three pulses were given to pole the sample before measuring the final polarization data. Consecutive positive (P, P') and negative (N, N') pulses give the required polarization values for calculation of intrinsic ferroelectric polarization.
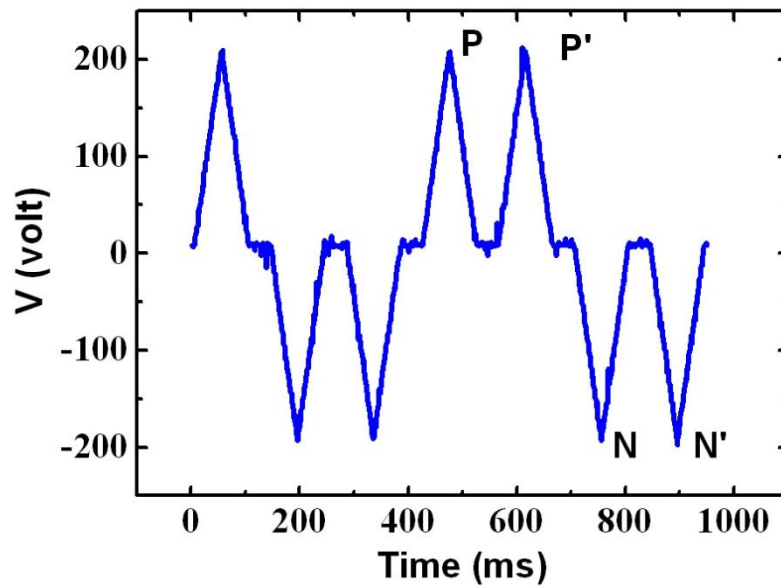
Figure 4.9   Drive voltage pulses for DWM measurement of $SmMn_{0.5}Cr_{0.5}O_3$.

Fig. 4.10 shows the recorded polarization data of $SmMn_{0.5}Cr_{0.5}MnO_3$ in presence of 2 T magnetic field in response to the voltage profile, as shown in the fig 4.9. The Calculated ferroelectric contribution after subtraction from P and P' for positive half and N and N' for negative half is shown fig 4.11, where the arbitrary initial polarization value is taken as zero and both positive and negative half is shifted by factor of 2 (see chapter 2.7 for details). The calculated remnant polarization is $0.02 \mu C/cm^2$ which is similar with the pyroelectric measurement. It is to be noted that the voltage applied for

DWM is 200 V and 100 V for pyroelectric current measurement which tells that this polarization value is closed to saturation polarization.
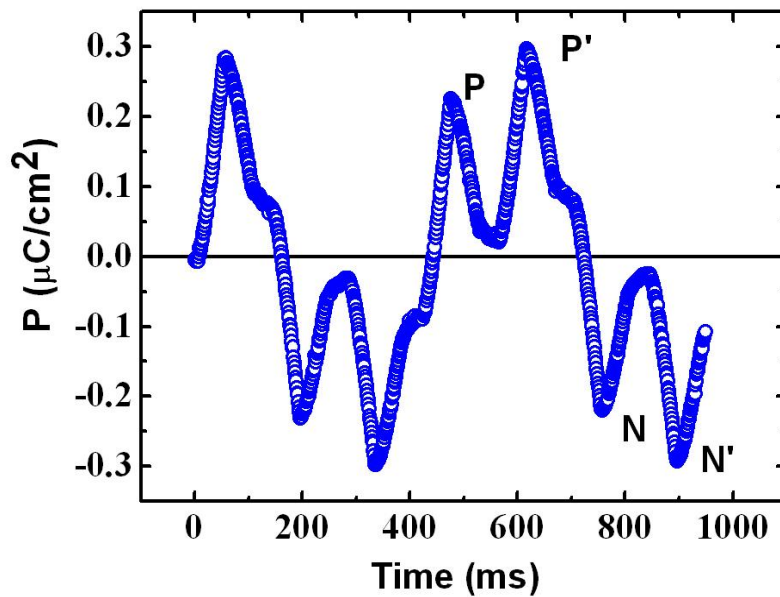
Figure 4.10   Measured polarization of $SmMn_{0.5}Cr_{0.5}O_3$ for the given voltage pulse.
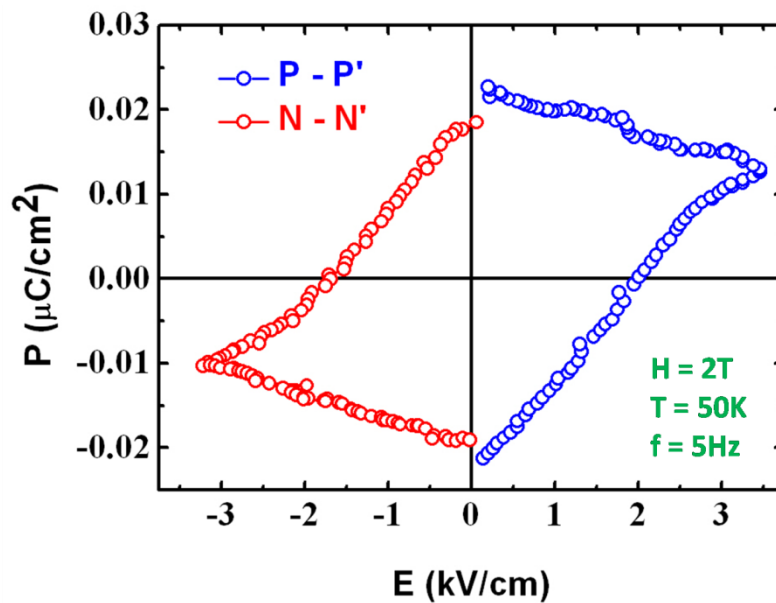
Figure 4.11   DWM result of $SmMn_{0.5}Cr_{0.5}O_3$

The nature of the loop suggests that there is resistive and capacitive polarization contribution which does not allow the polarization to get saturated, with only the first positive (P) or negative (N) pulse and hence polarization is added to the second pulse also. This gives some extra remnant polarization which could be avoided by measuring

84

the loop with very low frequency. Unfortunately the instrument limitation does not allow such possibility. Consequently, this appears in the loop as an increasing trend of polarization for the decreasing applied voltage (fig 4.11). The loop also shows that the ferroelectric polarization is not saturated even while applying the maximum possible field of 3.5 kV/cm. We also have performed DWM in absence of magnetic field at cryogenic temperature 10K as well as liquid nitrogen temperature (77K) where we did not observe a meaningful polarization from the obtained noisy, asymmetric apparent unsaturated loop.

DWM and Pyrocurrent measurement establishes that the polarization arises in the presence of magnetic field. This polarization is quite unusual as the transition temperature is above the magnetic ordering temperature, and the polarization appears in presence of magnetic field. As of now, the actual reason is unclear. From our previous experience of working with both disordered systems as well as ferroelectricity due to induced moment of the transition metal ion on the rare-earth ion, it is possible that both the aforementioned mechanisms may be at play simultaneously in the system. The actual extent of how these two contrasting mechanisms interplay to give rise to the ferroelectricity remains to be understood. The fact of ferroelectric polarization occurrence, at a temperature (> 50 K) greater than the magnetic ordering temperature indicates that disorder [17] or induced magnetic moment alone does not lead to ferroelectricity. It is to be noted that the Cr sublattice orders around 197 K, indicating that the induced moment on Sm^{+3} onsets in the vicinity of 197 K, complicating the origin of ferroelectric polarization in this system. It is also very important to measure the polarization of $SmFe_{0.5}Mn_{0.5}O_3$ and $SmFe_{0.5}Cr_{0.5}O_3$, which would help us to understand the origin of ferroelectricity and to explore what is actually happening in the disordered as well as 4f -3d interacting system.

4.4 Conclusion

Ferroelectricity is established in $SmMn_{0.5}Cr_{0.5}O_3$ in presence of magnetic field below 150 K temperature by measuring pyroelectric current and using DWM. The magnetic ordering temperature is observed at 100 K, which gives a paradox on the origin of the ferroelectricity. The actual reason of ferroelectricity is unknown. We have proposed some possible reason based on 3d-4f interaction and spiral spin ordering. Further work is required to explore this occurrence of ferroelectricity. The study of our other two synthesized materials, $SmFe_{0.5}Cr_{0.5}O_3$ and $SmFe_{0.5}Mn_{0.5}O_3$ is very important to investigate the disorder and rare-earth induced effect for this kind ferroelectric polarization occurrence.

4.5   Bibliography

1.   T. Kimura, T. Goto, H. Shintani, K. Ishizaka, T. Arima and Y. Tokura. *Nature*, 55, **426**, (2003).

2.   M. V. Mostovoy. *Phys. Rev. Lett.* **96**, 067601, (2006).

3.   H. Katsura, N. Nagaosa, and A. V. Balatsky. *Phys. Rev. Lett.,* **95**, 057205, (2005).

4.   Fiebig, M., Lottermoser, T., Frohlich, D., Goltsev, A. V. and Pisarev, R. V. *Nature*, **419**, 818 (2002).

5.   R. D. Shannon. *Acta Cryst*. **A32**, 751 (1976).

6.   Sangaletti, L.;Depero, L.E.;Allieri, B.;Nunziante, P.;Traversa, E. *Journal of the European Ceramic Society* **21**, 719 (2001).

7.   B. Nelson, *Zellmer university park USA ICDD grant-in-aid.* (1988).

8.   F. J. Morin, *Phys. Rev.* **78**, 819 (1950).

9.   Jong-Suck, Ayato Iyama, H. Nakamura, T. Kimura et al *Physical Review B* **82**, 212403 (2010).

10.   Jinhua Mao,Yu Sui,Xingquan Zhang et al, *Applied Physics Letters* **98**, 192510 (2011).

11.   P. Mandal, A. Sundaresan, C. N. R. Rao, A. Iyo, P. M. Shirage, Y. Tanaka,C. Simon, V. Pralong, O. I. Lebedev, V. Caignaert, and B. Raveau, *Phys.Rev. B* **82**, 100416 (R) (2010).

12.   Jung-Hoon Lee, Young Kyu Jeong, J H Park, J F. Scott *Physical Review L.* **107**,117201 (2011).

13.   B. Rajeswaran, P. Mandal, Rana Saha, E. Suard, A. Sundaresan, and C. N. R. Rao. *Chem. Mater*. **24**, 3591, (2012).

14.   Okazaki K and Maiwa H , *Japan. J. Appl. Phys*. 313113, (1992).

15.   Sawyer C B and Tower C H *Phys. Rev*. 35269 (1930).

16.   Fukunaga M and Noda Y *J. Phys. Soc. Japan,* 77064706 (2008).

17.   B. Rajeswaran,P. Mandal,Rana Saha,E. Suard, A. Sundaresan at al *Chem. Mater.* **24**, 3591, (2012).

18.   J.B. Goodenough, science, New York,1963, pp 165-185; (b) J. Kanamori. *Phys. Chem. Solids*, **10**, 87 (1959).

19.   4. L. Néel, *Ann. Phys. (Leipzig*) **3**, 137 (1948).

20.   E.F. Bertaut. Magnetism III, edited by G.T.Rado and H. Suhl. *Academic Press*, **149** (1968)

21.   Choithrani, R.;Rao, M.N.;Chaplot, S.L.;Gaur, N.K.;Singh, R.K. **11**, 073041 (2009).

22.   H.Homer and C.M.Varma *Phys. Rev. Let*. **20**, 16, 1968.

23.   P. Mandal, Venkata Srinu Bhadram, Y. Sundarayya, Chandrabhas Narayana, A. Sundaresan, and C. N. R. Rao. *PRL* **107**, 137202 (2011).

24.   S M Feng, Y S Chai, J L Zhu, N Manivannan, Y S Oh, L J Wang, Y S Yang, C Q Jin and Kee Hoon Kim. *New J. Phys.* **12** 073006 (2010).

25.   L. D. Landau and E. M. Lifshitz, *Electrodynamics of continuous media* (Fizmatgiz, Moscow), (1959)

Chapter 5

Ferroelectricity in $R_{1-x}Sc_xMnO_3$: (R=Nd and Sm & $0.1 \leq x \leq 0.3$)

5.1   Introduction

Research on multiferroics has got an immense interest with the discovery of perovskite orthorhombic rare-earth manganites as a very rich family where the entire rare-earth manganite series goes through the various interesting magnetic phase transitions and in some special regime, for example in $RMnO_3$ (R=Tb, Dy), it exhibits ferroelectricity at the onset of (some particular) magnetic ordering [1- 4, 15, 16, 29]. Figure 1 shows the phase diagram of the orthorhombic rare-earth manganite series [9]. Initially it was thought that magnetic and electric orderings are mutually exclusive so it was very difficult to think of ferroelectric ordering coming from magnetic ordering. In these compounds, the ferroelectricity is not just an accidental consequence but, it has magnetic origin which can give very high control of one by changing the other. This was the primary motivation in technological point of view such as spintronics, storage devices [28, 30]. It was a big breakthrough when $TbMnO_3$ was found to show a complete flip of electric polarization from c direction to a crystallographic direction by application of magnetic field along b direction [2]. In particular, a sinusoidal magnetic

ordering starts developing below T_{N1} = 41 K (Néel temperature for magnetic ordering) which is paraelectric but below T_{N2}= 27 K, the Mn^{+3} moments order in a cycloidal fashion and exhibits a remarkable ferroelectricity [2]. The cycloidal (spiral) magnetic ordering break the spatial inversion symmetry because the change of sign of all coordinates inverts the direction of rotation of cycloidal ordering hence develops spontaneous electrical polarization. This symmetry breaking phenomenon can be explained by inverse Dzyaloshinskii- Moriya interaction which causes spin ion displacements from the spin ion chain due to magnetic frustration and lattice relaxation.
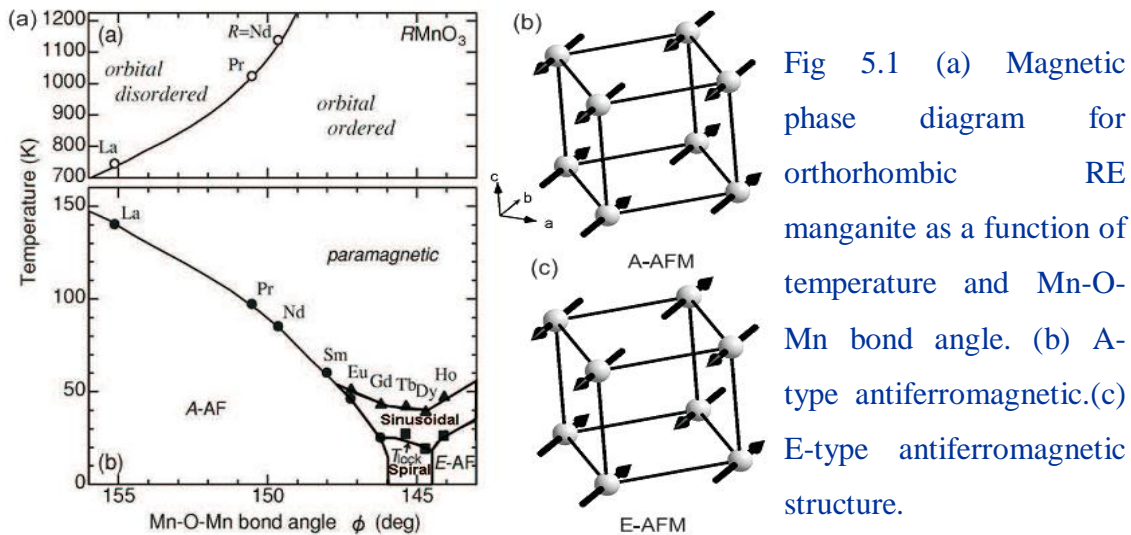

Fig 5.1 (a) Magnetic phase diagram for orthorhombic RE manganite as a function of temperature and Mn-O-Mn bond angle. (b) A-type antiferromagnetic.(c) E-type antiferromagnetic structure.

In manganites with smaller rare-earth size, [(Tb, Dy) MnO_3], because of the Mn^{+3} orbital ordering, the *ab* plane nearest neighbor interaction is ferromagnetic and the next nearest neighbor interaction is antiferromagnetic which frustrates the A-type AFM spin structure and give rise to an incommensurate collinear sinusoidal modulation along *b* direction (below 41 K for TbMnO₃) which is paraelectric. For further lowering the temperature, the magnetization increases in magnitude and a spiral spin ordering state becomes energetically more favorable (below 28K in TbMnO₃) which induces the polarization. The microscopic picture of induced polarization is given in the

introduction. In short, the induced polarization considering spin orbit coupling is given by the following equation:

$$\boldsymbol{P} = a \sum_{<i,j>} \boldsymbol{e}_{ij} \times \left(\boldsymbol{S_i} \times \boldsymbol{S_j} \right)$$

Where $\boldsymbol{S_i}$ and $\boldsymbol{S_j}$ are two neighboring spin vectors, '*a*' is the spin orbit coupling constant and $\boldsymbol{e}_{ij}$ is the spin chain wave vector. For manganites with much smaller rare-earth size [(Ho-Lu) MnO$_3$], it shows commensurate collinear E-type antiferromagnetic ordering with ferromagnetic zigzag spin chains (Fig. 5.1.c). Here, the ferroelectricity has different origin. Polarization is expected to arise from a gain in the band energy which produces hopping of e$_g$-electrons along the FM chain, and overcomes the competing elastic energy by displacing the ions [12]. From the phase diagram (Fig. 5.1.a), we see that the ground state of rare-earth manganites with higher radius have A-type anti-ferromagnetic ground state [Fig. 5.1.b] where the next nearest neighbor interaction is not sufficiently high to allow the frustration [1]. Because of this, there exist no spiral spin ordering below T$_N$. As a consequence, RMnO$_3$ with R = La to Eu do not exhibit ferroelectricity at the onset of magnetic ordering, however, these materials exhibit magnetic ordering at high temperature compared to the lower size rare-earth manganites [9]. The variation of size of the rare-earth gives a variation on the Mn-O-Mn bond angle which governs the strength of the superexchange interaction according to Goodeough- Kanamori rule [6]. In *Pnma* space group (RMnO$_3$), the orbital part of the wave function imposes antisymmetric symmetry in the *ab* plane and magnetic interaction becomes ferromagnetic whereas the mirror symmetry perpendicular to the c-axis results in the same orbital occupation along the c-axis which gives antiferromagnetic interactions along the c-axis. This is likely to be Mn-O-Mn (180°) superexchange interaction. When the Mn-O-Mn bond angle becomes less due to the

lower size rare- earth cation, the next nearest neighbor interaction starts dominating which is anti-ferromagnetic in nature and the competition between ferromagnetic and anti-ferromagnetic interactions frustrates the magnetic ordering. On further lowering of rare-earth size, the manganites ($YMnO_3$) crystallize in hexagonal phase at ambient pressure condition which is beyond the scope of our work. The boundary between two ordering (Spiral and A-type AFM ordering) approximately lies on Gd where an applied magnetic field enhances the non-collinear spiral ordering and induces ferroelectricity. The behavior of $GdMnO_3$ is very important which gives an idea of importance of the rare earth size in multiferroic behavior. The desired properties mentioned above can be achieved by mimicking the rare-earth size to Tb or Dy. For example, $Eu_{1-x}Y_xMnO_3$ ($0.55 < x > 0.3$) has the orthorhombic perovskite structure and undergoes ferroelectric transitions similar to those in $(Tb,Dy)MnO_3$. More interestingly, there is no report which discuss about the role of rare-earth magnetism in the rare-earth manganites in inducing multiferroicity [10]. The ferroelectricity in these materials is mainly associated with the rare-earth size.

Another new mechanism of multiferroicity is 3d - 4f magnetic interaction which is completely different from whatever we have discussed so far. Rare-earth chromites and ferrites both order antiferromagnetically (G-type) and exhibit ferroelectricity at the onset of magnetic ordering temperature. Unlike, rare-earth manganites, the rare-earth chromites and ferrites remain canted antiferromagnetic for all the rare-earth ions including Yttium. The magnetic rare earth plays an important role which has been prove by showing (Eu, Lu or Y) CrO_3 as non ferroelectric [13]. The microscopic reason of induced polarization lies in two major factor, first is poling field which breaks the inversion symmetry (rare-earth displace from centre of symmetry temporarily) and secondly the transition metal ion (namely Cr^{+3}, Fe^{+3}) gives a large induced magnetic

moment to the rare-earth site which stabilizes the distorted scenario (by 3d- 4f magnetic interaction) and thus the polarization arises due to displacement of R-ions.

Considering aforementioned fact, we wanted to establish the multiferroicity in the case of larger size rare-earth cations (La-Eu), which are reported to be non ferroelectric but have higher magnetic ordering temperatures. We chose to substitute Sc^{+3} ion at the rare-earth (Nd, Sm and Eu) site. Sc^{+3} have ionic size smaller than Y^{+3} ion. Goldsmith tolerance factor (t) for ABO$_3$ perovskite, where r_A, r_B, r_O are the ionic radius of A, B cation and oxygen anion is given by the following equation[17].

$$t = \frac{r_A + r_O}{\sqrt{2}\,(r_B + r_O)}$$

The following table shows different crystal structure according to the tolerance factor (t) [18].

Table 5.1　　Possible structures of ABO$_3$ from Goldsmith tolerance factor.

Goldschmidt tolerance factor (t)	Structure
> 1	Hexagonal
0.9-1	Cubic
0.71 - 0.9	Orthorhombic/Rhombohedral

From calculation of average radius of rare-earth and Sc^{+3} ion (r_A), we see that Sc^{+3} substitution level of as low as 15% can provide Goldsmith tolerance factor analogous to the TbMnO$_3$ [19]. Sc^{+3} could be easily substituted compared to other transition element in the rare-earth site because the formation of rare-earth scandats (RScO$_3$) need very high temperature and long duration of heating [14].

5.2   Experimental section

5.2.1   Sample preparation

The starting materials Nd_2O_3, Sm_2O_3, Eu_2O_3, Tb_4O_7 and Gd_2O_3 (rare-earth binary oxides) and Mn_2O_3, Sc_2O_3 (transition metal oxides) were used as obtained 99.9%. The rare-earth materials were preheated at 900 ^{o}C for overnight since all rare-earth are, to some extent, prone to be carbonated and moisturized to form $[R_2(CO_3)_3,3H_2O]$. The stoichiometric amount of rare-earth, Sc_2O_3 and Mn_2O_3 necessary for $Nd_{1-x}Sc_xMnO_3$ (x = 0.1, 0.15, 0.2, 0.25, 0.3) and $Sm_{1-x}Sc_xMnO_3$ (x = 0.1, 0.2, 0.3) were taken into agate mortar pestle and mixed thoroughly. The mixtures were heated at 1100, 1250, 1300 ^{o}C sequentially with intermittent grindings. Finally the powders were pressed into pellets and heated at 1400°C for 15 h for sintering. Manganese exhibit multi-valance state and it can go to Mn^{+4} oxidation state in presence of oxygen which gives high conductivity which is not suitable for electrical measurement. To avoid this, we heated all the compounds in Argon (Ar) atmosphere which was further purified by passing through hot (800 ^{o}C) Cu turnings to remove oxygen impurity present in the Ar.

5.2.2   Characterization by Powder X-ray diffraction

Powder X-ray patterns were taken by Bruker-D8 Advance Diffractometer (Cu K_α 1.54 Å wavelength) over a 2θ range 10° to 80° at room temperature. Phase purity and lattice parameters were obtained from X-ray data Rietveld refinement.

5.2.3   Magnetic measurements

Magnetic measurements were performed in Squid VSM (Quantum Design, USA). Field cooled magnetization versus temperature (M *vs.* T) at 100 Oe was recorded in the temperature range 2 K to 390 K and magnetization versus applied magnetic field data (M *vs.* H) were recorded at 5 K and 20 K.

5.2.4 Electrical measurement

For electrical measurements, silver paint was used to make the electrode on the polycrystalline well sintered samples. Dielectric properties were measured with Agilent E4980A LCR meter and pyrocurrent was recorded by Keithley (model 6517A) electrometer in the temperature range 10 K to 320 K. For pyrocurrent measurement, the samples were poled by cooling the sample from high temperature to low temperature under an applied electric field in presence or in absence of magnetic field. At low temperature, the samples were shorted for some few hours to allow for decaying the leakage current [experimental section]. Finally, pyrocurrent was measured while warming at 4 K/min rate. Both the measurements were performed in Physical Properties Measurement System (PPMS, Quantum Design).

5.3 Results and discussions

5.3.1. Structure

Rietveld refinement on the X-ray data of $Nd_{1-x}Sc_xMnO_3$ (x =0.0, 0.1, 0.15, 0.2, 0.25, 0.3) and $Sm_{1-x}Sc_xMnO_3$ (x = 0, 0.1, 0.2, 0.3) show that they all the samples crystallize in orthorhombic perovskite structure with space group *Pnma*, as expected since, the parent $NdMnO_3$, $SmMnO_3$ are of the same space group. For scandium substitution, beyond 30%, impurity phase ($ScMnO_3$) arises. All the X-ray patterns along with Rietveld refinements have been shown in the fig. 5.2. (a, b, c, d, e and f) for $Nd_{1-x}Sc_xMnO_3$ (x =0, 0.1, 0.15, 0.2, 0.25, 0.3) and fig. 5.3. (a, b, c and d) for $Sm_{1-x}Sc_xMnO_3$ (x = 0, 0.1, 0.2, 0.3). We infer from the study of $Nd_{1-x}Y_xMnO_3$ that the substitution of Y^{+3} (smaller ion) at the Nd^{+3} site, results in decreasing of *a*, *c* lattice parameters and a slight increase of *b* lattice parameter which results in overall decrease of unit cell volume [7]. Similarly, substituting Sc^{+3} (smaller ion) in R^{+3} (Nd, Sm) should also give lowering of unit cell volume with the increasing of substitutional concentration, according to the average radius of R^{+3} and Sc^{+3}.

In contrast, it is observed that, the lattice parameters *a*, *c* increase and *b* decreases with the increasing concentration of substituent (Sc^{+3}). The lattice parameters of all synthesized compounds is listed in table 5.2. Figure 5.4 shows the variation of lattice parameters with substitutional concentration in $Nd_{1-x}Sc_xMnO_3$ (x = 0, 0.1, 0.15, 0.2, 0.25, 0.3). The change of unit cell volume has also been shown in right axis of the same graph which shows that the cell volume increases with the Sc^{+3} concentrations. Compared to the parent compound ($NdMnO_3$), the decreases of lattice parameter *b* in $Nd_{0.9}Sc_{0.1}MnO_3$ is much more, than the increment of *a* and *c* lattice parameter, which results in overall decrease of unit cell volume.
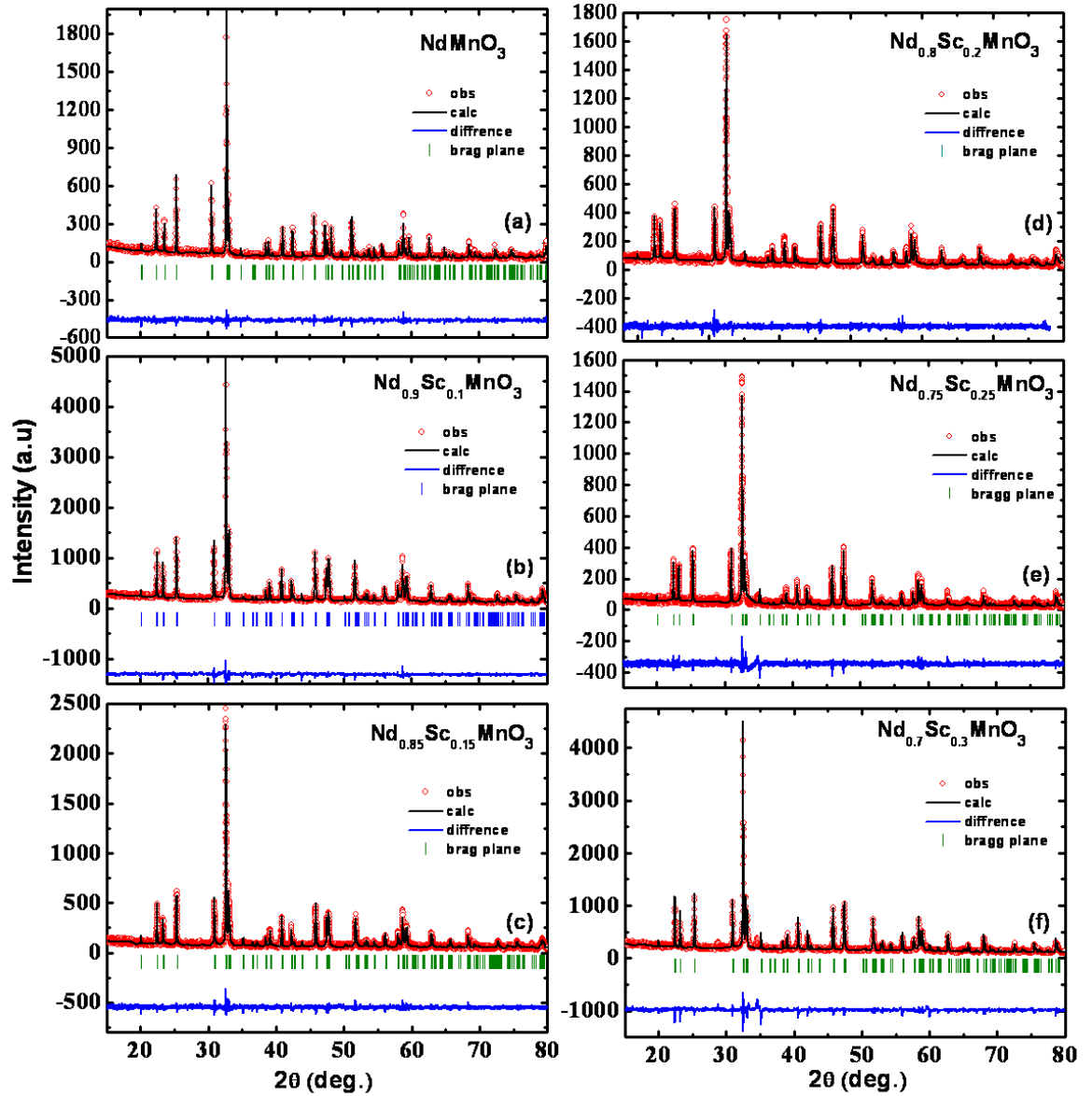
Figure 5.2 Rietveld refinement on the X-ray diffraction data (a) NdMnO$_3$ (b) Nd$_{0.9}$Sc$_{0.1}$MnO$_3$ (c) Nd$_{0.8}$5Sc$_{0.15}$MnO$_3$ (d) Nd$_{0.8}$Sc$_{0.2}$MnO$_3$ (e) Nd$_{0.75}$Sc$_{0.25}$MnO$_3$ (f) Nd$_{0.7}$Sc$_{0.3}$MnO$_3$, where red circles, black lines, blue lines, green vertical lines show observed, calculated, difference intensity and Bragg's planes correspond to the peak, respectively.
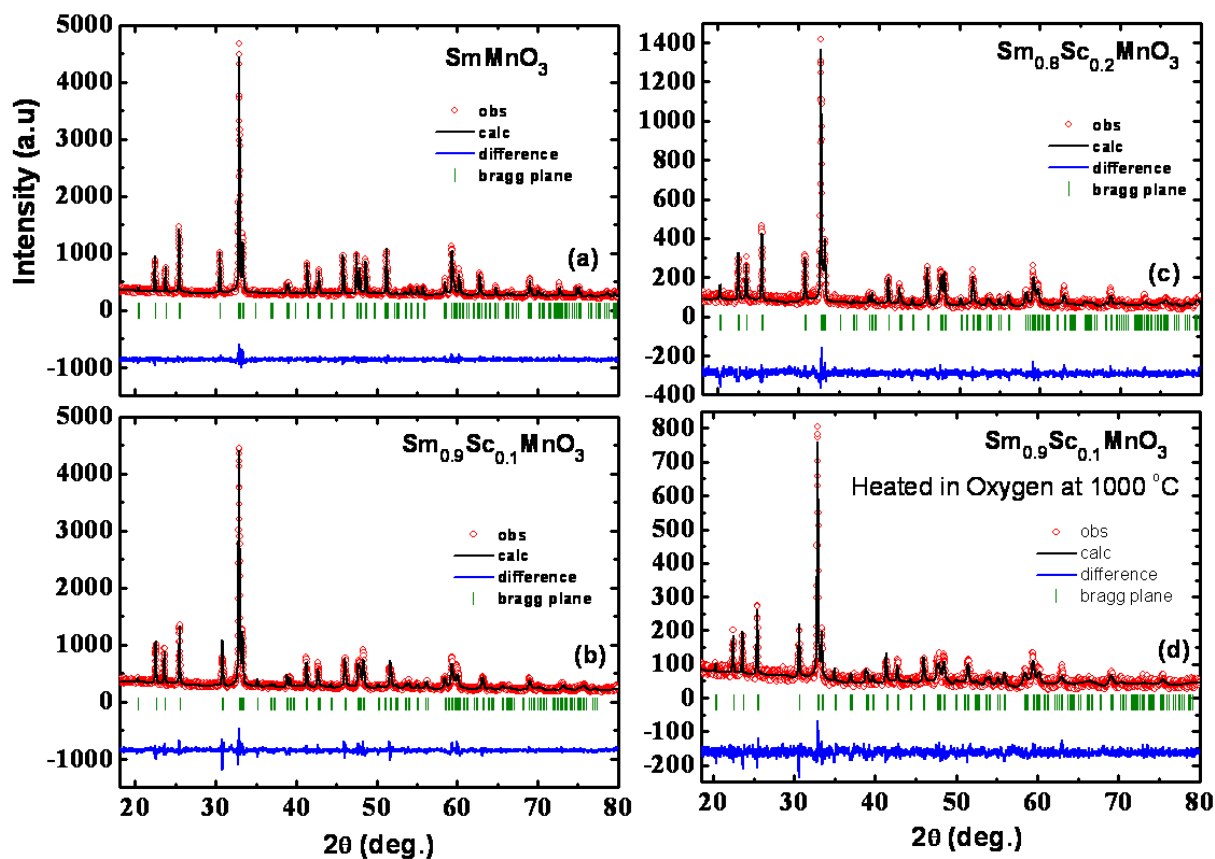
Figure 5.3 Rietveld refinement on the X-ray diffraction data of (a) $SmMnO_3$ (b) $Sm_{0.9}Sc_{0.1}MnO_3$ (c) $Sm_{0.8}Sc_{0.2}MnO_3$ (d) $Sm_{0.9}Sc_{0.1}MnO_3$, after heating in oxygen at 1000 ^{o}C for 20 hour.
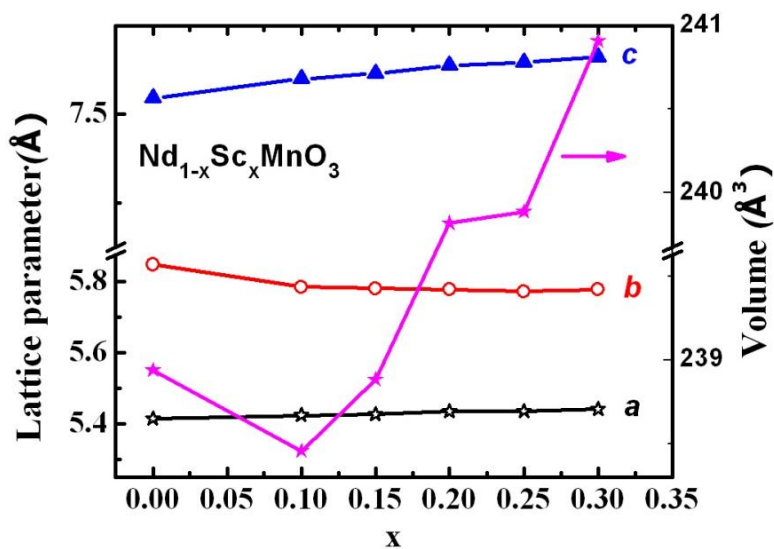

Figure 5.4 Lattice parameter (left Y axis) and lattice volume (right Y axis) changing with Sc^{+3} substitution in $NdMnO_3$.

Table 5.2   Lattice parameters of all synthesized compounds.

Compound name	a (Å)	b (Å)	c (Å)	Volume (Å)^3	X^2
$NdMnO_3$	5.415	5.848	7.545	238.94	1.40
$Nd_{0.9}Sc_{0.1}MnO_3$	5.423	5.786	7.510	235.65	1.58
$Nd_{0.85}Sc_{0.15}MnO_3$	5.427	5.781	7.615	238.91	1.43
$Nd_{0.8}Sc_{0.2}MnO_3$	5.435	5.778	7.637	239.82	1.31
$Nd_{0.75}Sc_{0.25}MnO_3$	5.435	5.772	7.646	239.89	1.77
$Nd_{0.7}Sc_{0.3}MnO_3$	5.442	5.778	7.662	240.91	2.19
$SmMnO3$	5.366	5.857	7.482	235.16	1.21
$Sm_{0.9}Sc_{0.1}MnO_3$	5.368	5.795	7.523	234.04	2.45
$Sm_{0.8}Sc_{0.2}MnO_3$	5.378	5.795	7.555	235.44	1.50

5.3.2. Magnetic Properties

$NdMnO_3$ is a canted antiferromagnet with $T_N \approx 75$ K. Surprisingly, we observe a magnetization reversal for the entire Sc substituted compounds, $Nd_{1-x}Sc_xMnO_3$ (x= 0.1 to 0.3) as shown in fig.5.5. We see a sharp decrease in magnetization below 20 K and it goes through zero magnetization (compensation point) to a negative value (opposite to the applied field direction). The magnetization reversal phenomenon is unusual and rare. It was first predicted by Néel in ferrimagnetic compounds where two magnetic sublattices have different temperature dependence and hence may get cancelled at a particular temperature when both the moments are antiferromagnetically coupled [20-24]. In the whole rare-earth manganite series, only $SmMnO_3$ shows such magnetization reversal in its ground state because of antiferromagnetically coupled Sm^{+3} and canted Mn^{+3} moments [11]. This is also observed in $La_{1-x}Gd_xMnO_3$ when the Gd^{+3} ion concentration is increased above 25%. Here the Gd^{+3} moments are antiferromagnetically coupled to the canted Mn^{+3} moments [25]. In another example, $Nd_{1-x}Ca_xMnO_3$ (x= 0.06 to 0.15) consisting of exchange coupled weak ferromagnetism of canted Mn^{+3} moment and ferromagnetism (Mn^{+3}-O-Mn^{+4}) due to double exchange. These two different magnetism (weak ferromagnetism and ferromagnetism) differ in sign in the f-d exchange interaction. The Nd^{+3} moment order antiparallel to the weak ferromagnetic Mn^{+3} moments and parallel to the Mn^{+3} in the ferromagnetic phase. At low temperature, the antiferromagnetic coupling of both the weak ferromagnetic and ferromagnetic moments to the Nd^{+3} moments lead to a compensation and hence negative magnetization [26].

In the present case, upon substitution of Sc^{+3} in both $NdMnO_3$ (fig.5.5) and $SmMnO_3$ (fig.5.6) cases, the net positive moment below T_N increases. It implies that the canting of Mn^{+3} increases with increasing Sc^{+3} concentration. In particular, the decrease of

average radius of 'A' site cation provides much frustration in the *ab* plane as the bond angle (Mn^{+3}-O-Mn^{+3}) decreases. Another aspect of Sc^{+3} doping in 'A' site is that, it decreases the rare-earth concentration.
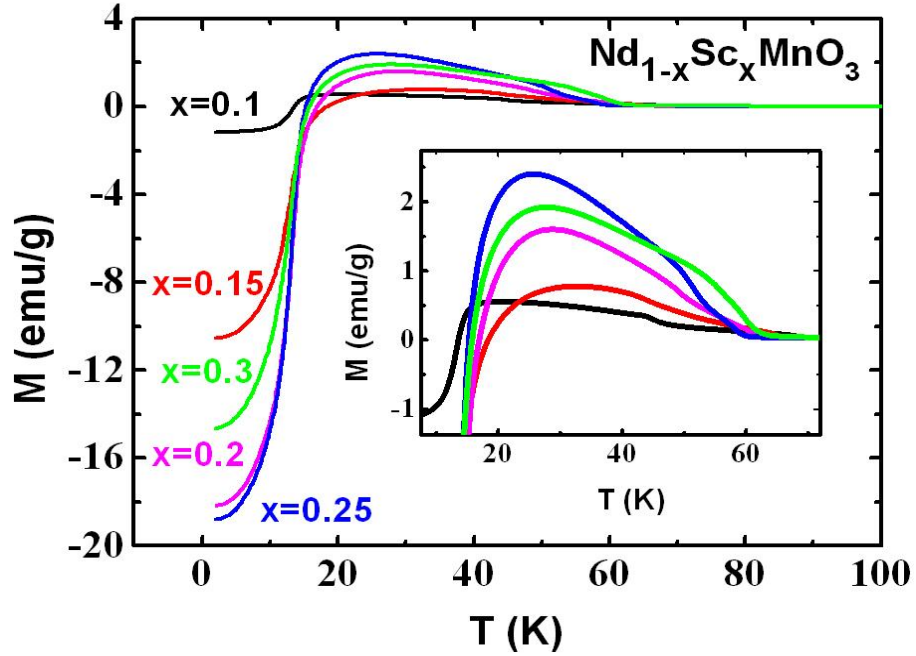

Figure 5.5   FC (100 Oe) M *vs.* T data of Nd$_{1-x}$Sc$_x$MnO$_3$ (x=0, 0.1, 0.15, 0.2, 0.25, 0.3).
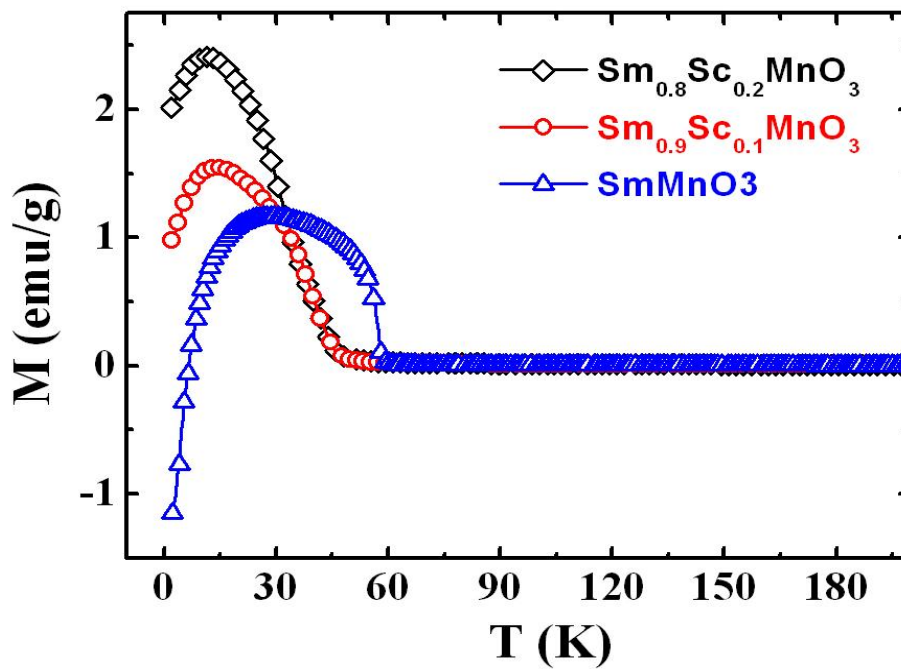

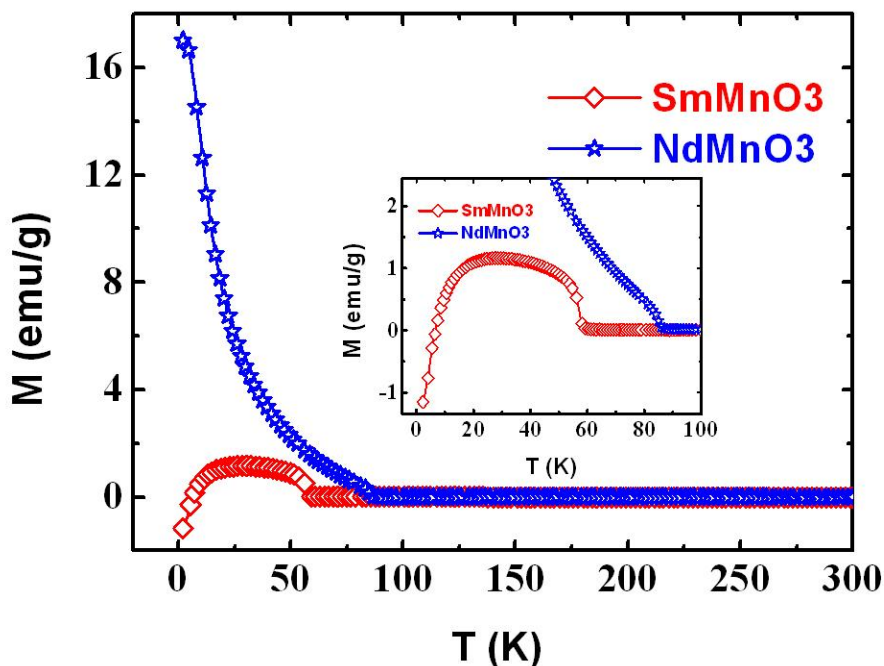**Figure 5.6**   FC (100 Oe) M *vs.* T data of Sm1-xScxMnO$_3$ (x=0, 0.1, 0.2).

Figure 5.7   FC (100 Oe) M *vs.* T data of SmMnO$_3$ and NdMnO$_3$.

So the rare-earth moment decreases with the increasing Sc^{+3} ion substituent concentration. It is observed from the fig 5.5 and fig 5.6, that the extent of decrease of the rare-earth moment is much higher than the extent of enhancement of canted Mn^{+3} moments. Figure 5.7 shows that Nd^{+3} ion has large moment as compared to Sm^{+3} ion moment. As a result, with increasing the concentration of Sc^{+3}, the magnetic moment of Nd^{+3} decreases to a much lower value than the increased canted moment of Mn^{+3}. Also, it can be noted that the Nd^{+3} moment is antiferromagnetically coupled to the canted Mn^{+3} moments like in SmMnO$_3$ [27]. Thus, in Sc^{+3} substituted NdMnO$_3$, the magnetization reaches compensation around 15 K and exhibits magnetization reversal due to the opposite Nd^{+3} moments. This is observed for the entire substitutional range of Sc^{+3} ion. But, the negative moment increases up to the 25% Sc^{+3} substitution and above this the negative moment again becomes small [fig. 5.5]. Therefore, it is also clear that with the increasing substitutional concentration, the Mn^{+3} moment increases to higher values while the Nd^{+3} moment decreases. This is a clear indication of

increasing magnetic frustration with the decreasing average radius of 'A' site cation by substituting Sc^{+3}. Substitution of Sc^{+3} in parent $SmMnO_3$ does not show magnetization reversal which is characteristics of the parent $SmMnO_3$ compound as observed from fig. 5.6. The similar reason can be exploited here. We see Sm^{+3} ion has smaller moment than Nd^{+3} ion [fig. 5.7]. When Sm^{+3} is diluted further by Sc^{+3}, Sm^{+3} moment becomes much smaller while, the canted Mn^{+3} moments are enhanced due to increasing Mn^{+3} canting. On net, moments of Sm^{+3} and Mn^{+3} do not cancel each other, thus are antiferromagnetically coupled and only a decreasing trend of the net negative moment is observed. Initially, it was suspected that the decrease in the moment on the substituted compound could be due to some magnetic defect also, such as phase impurity, oxygen vacancies, presence of Mn^{+4} ions etc. We have performed magnetization versus temperature measurement for $Sm_{0.9}Sc_{0.1}MnO_3$ compound, which was further annealed in different atmospheres such as oxygen with different duration and Ar at 1000 ^{o}C after final sintering. Fig 5.8 shows that there is a very small change (inconsistent with heat treatment) on the net moment and T_N (Néel temperature) but over all magnetization behavior is same.

Since, all the compounds, after annealing in different atmosphere, are single phase as confirmed by X-ray diffraction pattern, the magnetization reversal is an intrinsic property of these compounds. Figure 5.9 shows that compensation temperature decreases with the increasing magnetic field. This can be explained by the increasing canted moment in presence of external magnetic field. This was further confirmed by M *vs.* H study of $Nd_{1-x}Sc_xMnO_3$ at 5 K, (fig 5.10) where we see an unsaturated hysteresis loop due to combined rare-earth and canted Mn^{+3} magnetic moments.
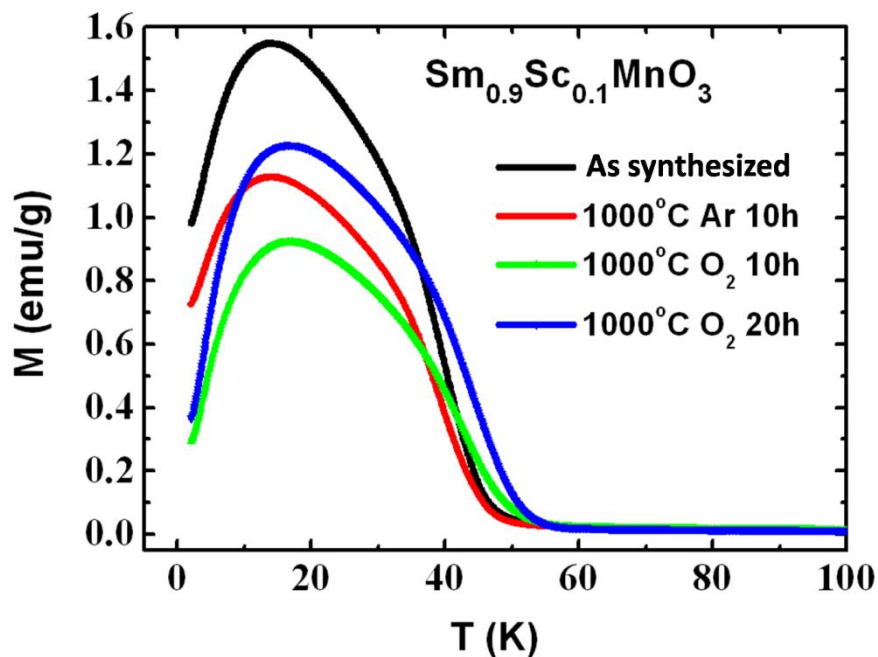
Figure 5.8   FC (100 Oe) M *vs.* temperature data of $Sm_{0.9}Sc_{0.1}MnO_3$. Black curve represents for as synthesized and Red, green, blue represent for compound annealed in different condition.
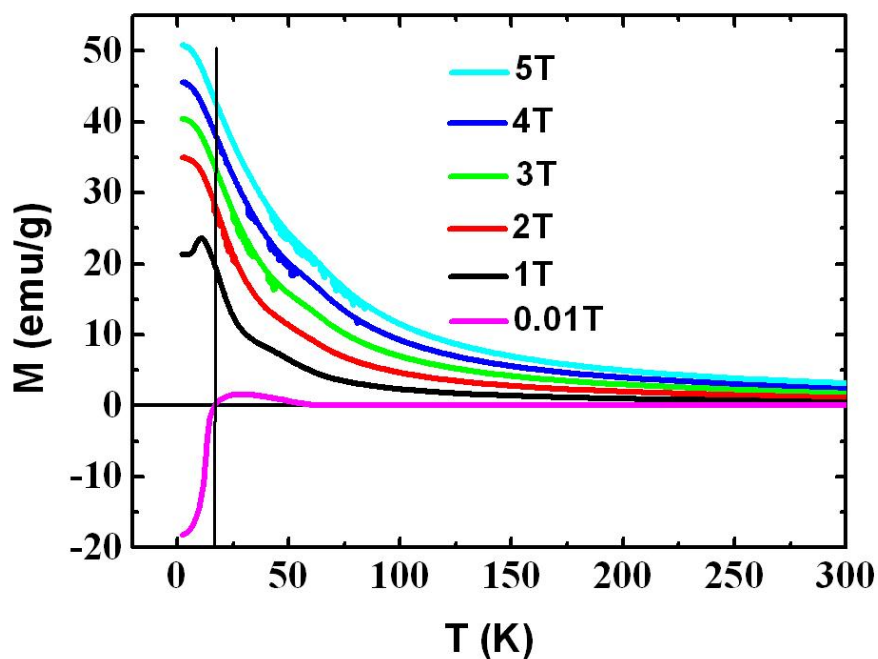

Figure 5.9   Field dependent FC, M *vs.* T data of $Nd_{0.8}Sc_{0.2}MnO_3$.
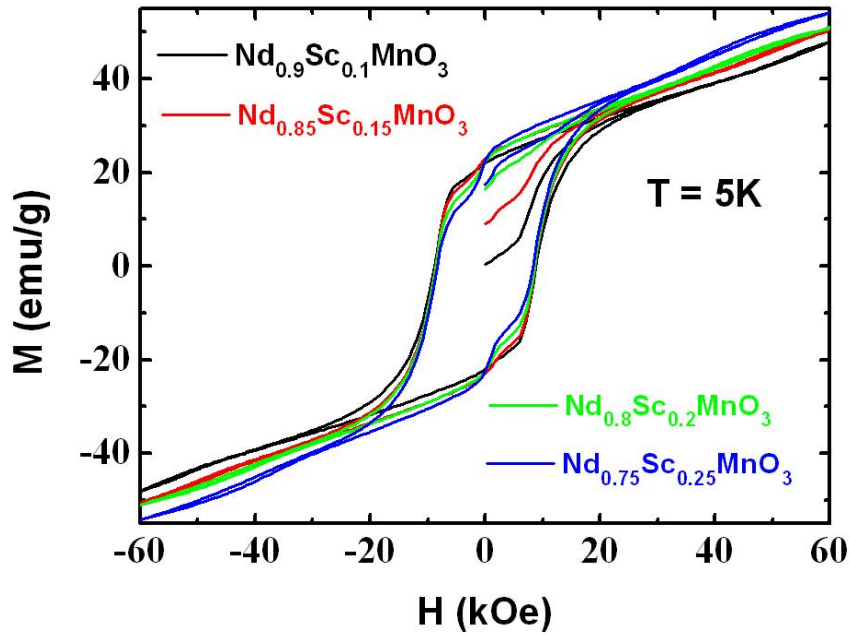
Figure 5.10   M *vs.* T data at 5K for Nd$_{1-x}$Sc$_x$MnO$_3$ (x=0.1, 0.15, 0.2, 0.25 and 0.3).

With increasing concentration of Sc^{+3}, the net moment increases, which once again confirms the increase in canted Mn^{+3} moments [fig 5.10]. Upon careful inspection, it is found that the net moment decreases after 25% substitution of Sc^{+3}. This is consistent with the FC magnetization data [fig 5.5], which shows after 25% substitution of Sc^{+3}, the canted Mn^{+3} moments starts dominating over the rare earth moment.
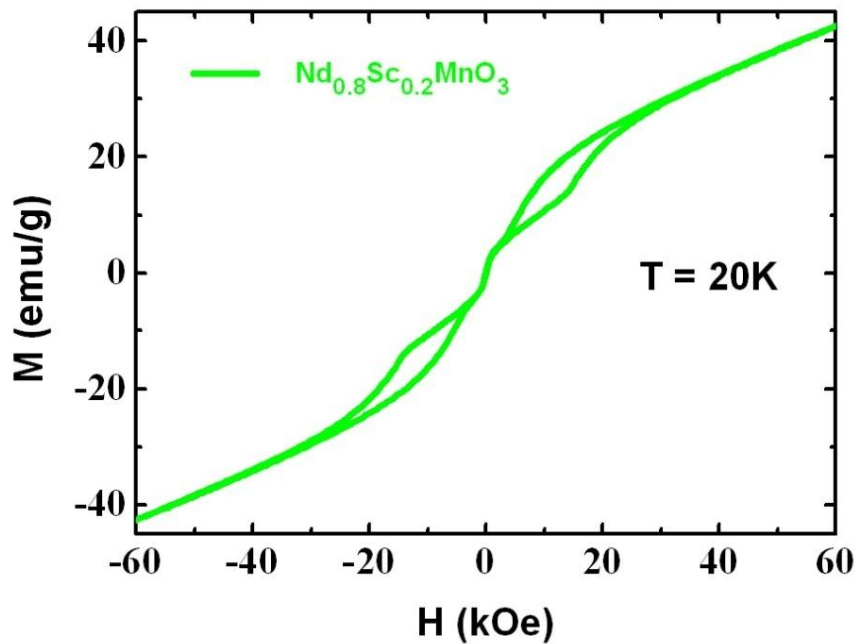

Figure 5.11   M Vs H data of Nd$_{0.8}$Sc$_{0.2}$MnO$_3$ at 20 K.

107

Figure 5.11   shows magnetization versus temperature data for $Nd_{0.8}Sc_{0.2}MnO_3$ at 20 K. We observe here halves for the M *vs.* H loop. The compound has a compensation point just below 20 K, which can be shifted with the applying magnetic field. With the increasing magnetic field, the canted moment increases while the compensation temperature decreases. So the moment increases at much higher rate at lower applied field. Above a certain magnetic field, when the compensation point does not go further low temperature, the canted moment contributes to opening up of the unsaturated magnetic hysteresis loop. A similar process takes place at the opposite quadrant as shown in the fig. 5.11. Thus, we observe two halves in the M *vs.* H hysteresis loop. It becomes more pronounced when M *vs.* H data is recorded near the compensation point. The significance of this observation is that, it confirms indirectly the antiferromagnetic coupling of rare-earth moments with the canted Mn^{+3} moments. The similar behavior was also observed in the $Nd_{1-x}Ca_xMnO_3$ [26].

5.3.3   Ferroelectricity

The most exciting and remarkable result is the observation of ferroelectricity in both $Nd_{1-x}Sc_xMnO_3$ and $Sm_{1-x}Sc_xMnO_3$ systems, which is the rationale behind the work. Figure 5.12 displays the pyrocurrent peak observed in $Sm_{0.9}Sc_{0.1}MnO_3$ around 65 K when the sample was poled from 120 K to 10 K with 100 V and -100 V in presence of magnetic field as well as in absence of magnetic field. The open (orange and blue) circles represent the pyrocurrent without magnetic field and solid (black and red) represents the pyrocurrent in presence of 4T field. For both the cases, we observe the pyrocurrent peak, in addition to the fact that in the presence of magnetic field, the peak intensity is markedly suppressed. The switching of the pyrocurrent peak is also observed when the sample was poled with reverse voltage. Figure 5.13 shows

polarization value when the pyrocurrent was integrated upon time as shown in the figure 5.12.
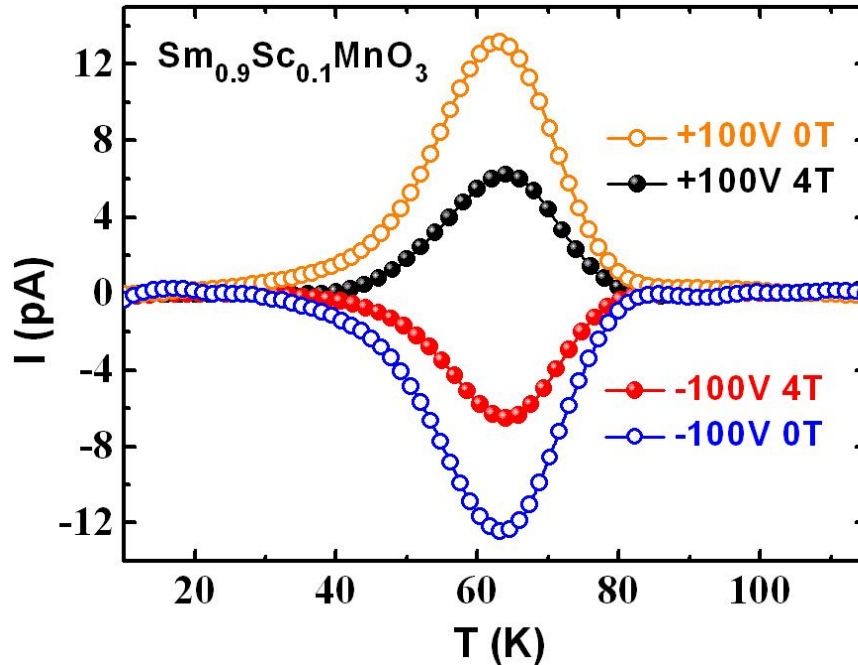

Figure 5.12 Pyrocurrent measured data of Sm$_{0.9}$Sc$_{0.1}$MnO$_3$. The open (orange and blue), solid (black and red) shows the pyrocurrent for (+100V, -100V) 0 T and 4 T respectively.

This suggests that the ferroelectric polarization sets in at 65 K. From the FC magnetization we see the magnetic ordering temperature is around 50 K, however, the pyrocurrent peak arises at 65 K. We observed a difference in temperature which may be due to different experimental setup (PPMS and Squid magnetometer). We have confirmed that our PPMS had a temperature lag of around 10 K which may cause the pyrocurrent to arise 10 K above the magnetic ordering temperature while the temperature dependence of magnetic measurement is relatively more accurate.
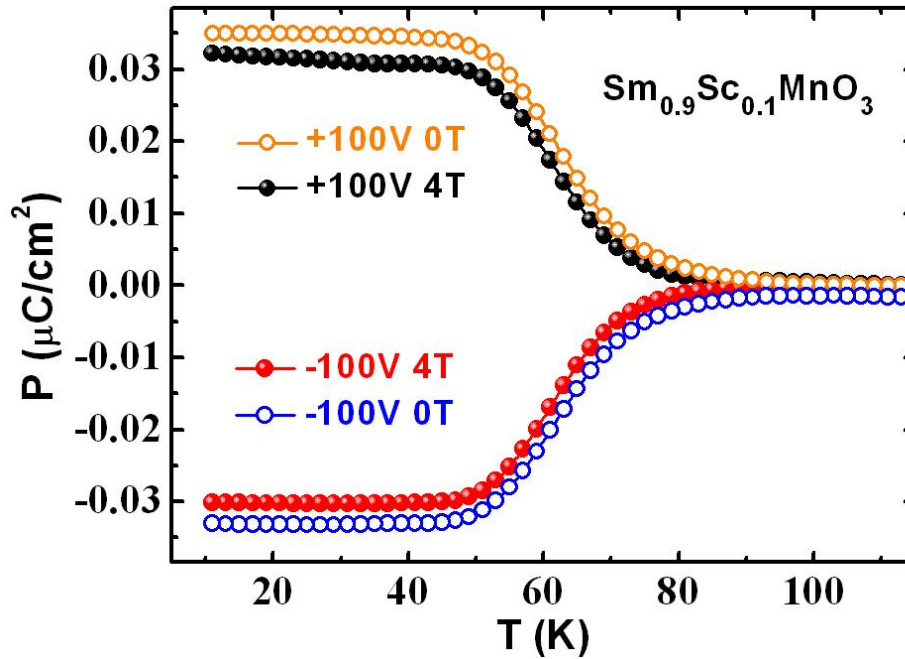
Figure 5.13 Reversal of integrated polarization (P) value in $Sm_{0.9}Sc_{0.1}MnO_3$ confirming bipolar nature.

The pyrocurrent peak can actually be assumed at the magnetic ordering temperature of Mn^{+3} ions. Hence the origin of ferroelectricity seems to occur at magnetic ordering. Furthermore, pyrocurrent measurement in $Nd_{0.8}Sc_{0.2}MnO_3$ sample also shows pyrocurrent peak at around 77 K [fig 5.14 inset] wherein the magnetic ordering is observed at around 60 K [fig 5.5]. The temperature difference is consistent with the $Sm_{0.9}Sc_{0.1}MnO_3$ sample. Fig. 5.14 shows the integrated polarization reversal where black open and red open points data shows the polarization for +80 V and -80 V poling voltage respectively. The maximum polarization (P) for 1.3 kV/cm electric field is around 0.025 $\mu C/cm^2$. It is expected based on our above presented result that the other $Nd_{1-x}Sc_xMnO_3$ (x = 0.1, 0.15, 0.25) and $Sm_{1-x}Sc_xMnO_3$ (x= 0.2, 0.3), which has not been measured yet, would also show the ferroelectric polarization. According to the Goldsmith factor, this result is expected (c.f. $TbMnO_3$) although the experimental lattice parameter values are contradictory. It is to be noted that the parent compounds do not show any ferroelectric polarization at the magnetic ordering temperature.
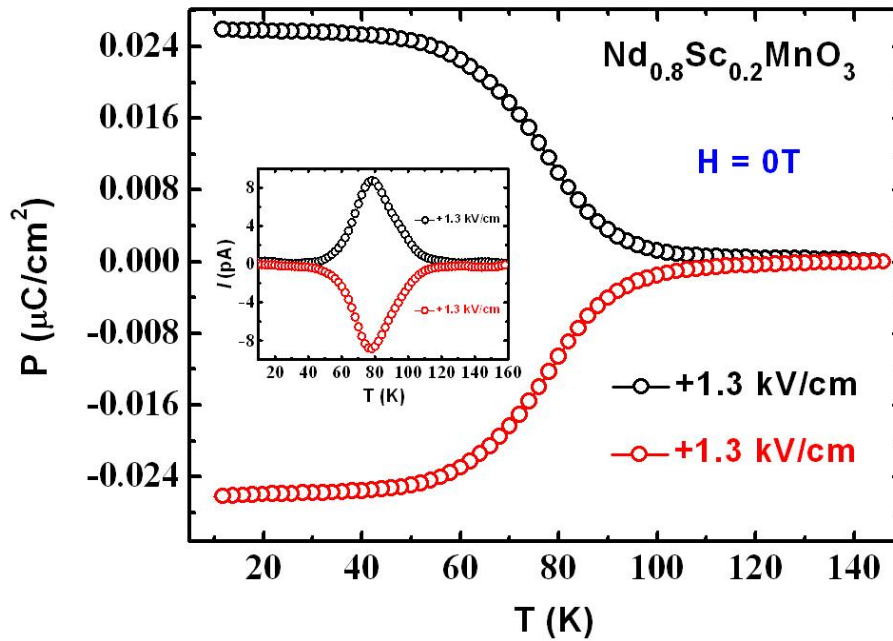
Figure 5.14 Integrated polarization for both directions in Nd$_{0.8}$Sc$_{0.2}$MnO$_3$. Inset shows the recorded pyrocurrent.

There could be one of the two plausible origins irrespective of lattice parameter value discussed in earlier. Firstly, this ferroelectricity could be due to lowering of 'A' site cation size on average which would give rise to frustration in the *ab* plane and hence non collinear spiral ordering leading to the polar state which is very similar to the classical TbMnO$_3$. However, we could not observe any significant anomaly in the dielectric measurement, instead we observe a small change of slope near the magnetic ordering temperature. The dielectric anomaly is supposed to be observed at the same magnetic ordering temperature, in case if the material is ferroelectric. But if the ferroelectricity occurs at a particular crystallographic direction then the dielectric anomaly might be suppressed as our samples are polycrystalline. Our pyroelectric measurement in the presence of 4 T magnetic field shows that magnetic field has an effect on the ferroelectricity. Actually, the direction of polarization can be flipped from

one direction to another (from c to a as observed in $TbMnO_3$) which is reflected in the value of pyroelectric current [2]. The detailed experimental observation of directional dependence of polarization is discussed for similar compound in single crystal ($TbMnO_3$, $Eu_{1-x}Y_xMnO_3$) elsewhere [2-4, 8].

On the other hand, the ferroelectricity could be understood by newly proposed 3d-4f interaction mechanism. This is very similar to the origin of ferroelectricity in the rare-earth ortho chromites ($RCrO_3$) [13]. $RCrO_3$ has G-type antiferromagnetic ordering of 3d transition element. A combined effect of 3d-4f exchange striction and external applied electric field explained the ferroelectricity there [13]. The external electric field creates a local non-centrosymmetric distortion (a local temporary polarization) of rare-earth ion which would be stabilized further due to canted magnetic moment of 3d transition element below magnetic ordering temperature. The net dipole moment of rare-earth and oxygen bond gives the ferroelectric polarization. Here, the role of rare-earth moment is very important. It is already reported that $Eu_{1-x}Y_xMnO_3$ exhibits ferroelectricity, which proves the ferroelectricity in $TbMnO_3$ analogous compounds do not involve the rare-earth magnetism.

To confirm the ferroelectricity further in our compounds, we have to perform similar experiments on $Eu_{1-x}Sc_xMnO_3$. If it becomes ferroelectricity (Eu^{+3} being non magnetic) then the mechanism responsible for ferroelectricity to the magnetic frustration. This will also show that the occurrence of ferroelectricity, due to spiral ordering, does not require the lattice parameter constrained which is exploited in the other similar compounds like $Nd_{1-x}Y_xMnO_3$ [7, 25]. Most interestingly, in our case, the ferroelectricity occurs at relatively higher temperature. So this provides a strategy to get the ferroelectricity from the magnetic origin at higher temperatures.

5.4   Conclusion

We have synthesized the Nd$_{1-x}$Sc$_x$MnO$_3$ (x = 0.1, 0.15, 0.2, 0.25), Sm$_{1-x}$Sc$_x$MnO$_3$ (x = 0.1, 0.2, 0.3) series of compound which shows ferroelectricity below the magnetic ordering temperature. We have proposed two different mechanisms for the occurrence of ferroelectricity. The details of underlying magnetic structure are not yet verified to investigate the real picture of spin structure and lattice structure. Interestingly the ferroelectricity occurs at much higher temperature than the classical TbMnO$_3$ multiferroic which gives us way to find new multiferroic manganites at higher temperature. Definitely, we need a single crystal study on our sample so that we could see the direction dependency of the ferroelectric polarization.

5.5   Bibliography

1.   E. Wollen and W. Kohler, *Phys. Rev.***100**, 545 (1955).

2.   T. Kimura, T. Goto, H. Shintani, K. Ishizaka, T. Arima, and Y. Tokura, *Nature* (London) **426**, 55 (2003).

3.   T. Kimura, S. Kawamoto, I. Yamada, M. Azuma, M. Takano, and Y. Tokura*, Phys. Rev*. **B67** , 180401 (R) (2003).

4.   S. Cheong and M. Mostovoy, *Nat. Mater*. **6,** 13 (2007).

5.   Daniel Khomskii, *Physics2*, **20** (2009).

6.   J.B. Goodenough, science, *New York,* 165-185 (1963); (b) J. Kanamori, *Phys. Chem. Solids*, **10**, 87 (1959).

7.   S. Landsgesell, K. Prokes, B. Ouladdiaf, B. Klemke, O. Prokhnenko, B. Hepp, K. Kiefer and D. N. *Argyriou, Phys. Rev*. B **86** , 054429 (2012).

8.   J. Hemberger, S. Lobina, H.-A. Krug von Nidda, N. Tristan, V. Yu. Ivanov, A. A. Mukhin, A. M. Balbashov, and A. Loidl, *Phys. Rev. B*. **70**, 024414 (2004).

9.   T. Kimura, S. Ishihara, H. Shintani, T. Arima, K. T. Takahashi, K. Ishizaka and Y. Tokura *Phys. Rev. B* **68**, 060403 (R) (2003).

10.   J. Hemberger, F. Schrettle, A. Pimenov, P. Lunkenheimer, V. Yu. Ivanov, A. A. Mukhin, A. M. Balbashov, and A. Loidl *Physical Rev.* B.**75**, 035118 (2007).

11.   Jong-Suck Jung, Ayato Iyama, Hiroyuki Nakamura, Masaichiro Mizumaki, Naomi Kawamura, Yusuke Wakabayashi and Tsuyoshi Kimura, *Phys. Rev. B* **82,** 212403, (2010).

12. S M Feng, Y S Chai, J L Zhu, N Manivannan, Y S Oh, L J Wang, Y S Yang, C Q Jin and Kee Hoon Kim, *New Journal of Physics* **12,** 073006, (2010).

13. B. Rajeswaran, D. I. Khomskii, A. K. Zvezdin, C. N. R. Rao and A. Sundaresan. *Phys. Rev. B* **86**, 214409, (2012)

14. Ruslan P. Liferovich and Roger H. Mitchell, *Journal of Solid State Chemistry* **177,** 2188, (2004).

15. L. Lin, L. Li, Z.B. Yan, Y. M . Tao, S. Dong · J.-M. Liu, *Appl Phys A* **12,** 7453, (2012).

16. O. Prokhnenko, R. Feyerherm, E. Dudzik, S. Landsgesell, N. Aliouane, L.C. Chapon, and D. N. Argyriou, *Phys Rev Lett.* 057206, (2007).

17. Goldschmidt, Victor M. *Die Naturwissenschaften* **21,** 477, (1926).

18. Schinzer, Carsten. "Distortion of Perovskites". Retrieved 17 May 2012.

19. R. D. Shannon, *Acta Cryst***A32**, 751, . (1976).

20. Y. Ren, T. T. M. Palstra, D. I. Khomskii, E. Pellegrin, *nature,*Vol **396** , 441, (1998).

21. E. W. Gorter and J. A. Schulkes, *Phys. Rev*. **90**, 487, (1953).

22. N. Menyuk, K. Dwight, and D. G. Wickham, *Phys. Rev. Lett*. **4**, 119, (1960).

23. L. Néel , *Ann. Phys. (Leipzig)* **3**, 137 (1948).

24. P. Mandal, A. Sundaresan, and C. N. R. Rao, *Phys. Rev. B* **82**, 100416R, (2010).

25. J. Hemberger, S. Lobina, H.-A. Krug von Nidda, N. Tristan, V. Yu. Ivanov, A. A. Mukhin, A. M. Balbashov, and A. Loidl, *Phys. Rev. B.* **70**, 024414 (2004).

26.   IO Troyanchuk ,VAKhomchenko, GMCho bot, AIKur bakov et al. *J. Phys. Condens. Matter* **15**, 8865, (2003).

27.   S. Landsgesell, K. Prokes, B. Ouladdiaf, B. Klemke, O. Prokhnenko, B. Hepp, K. Kiefer and D. N. Argyriou, *Phys. Rev. B* **86** , 054429, (2012).

28.   HB́ea, MGajek, M Bibes and A Barthélémy *J. Phys. Condens. Matter* 434221, (2008).

29.   Hur, N. et al. *Nature* **429**, 392, (2004).

30.   H. Bea, M. Bibes, S. Cherifi, F. Nolting, B. Warot-Fonrose, S. Fusil, G. Herranz, C. Deranlot, E. Jacquet, K. Bouzehouane, A. Barthelemy, *Appl. Phys. Lett*. **89**, 242114, (2006).

31.   Choithrani, R.;Rao, M.N.;Chaplot, S.L.;Gaur, N.K.;Singh, R.K. *New Journal of Physics*, **11**, 073041, (2009).

32.   de la Calle, C. Alonso, J.A. Martinez Lope, M.J. Retuerto, M. Garcia Hernandez, M. Fernandez Diaz, M.T. *European Journal of Inorganic Chemistry,* **5**, 781, (2010) .

33.   Choithrani, R.Rao, M.N. Chaplot, S.L. Gaur, N.K. Singh, R.K. Journal of Magnetism and Magnetic Materials, **323**(12), 1627, (2011).